

# A Description of the Correlated $k$ Distribution Method for Modeling Nongray Gaseous Absorption, Thermal Emission, and Multiple Scattering in Vertically Inhomogeneous Atmospheres

ANDREW A. LACIS

*NASA Goddard Space Flight Center, Institute for Space Studies, New York*

VALDAR OINAS

*Queensborough Community College of CUNY, New York  
STX, Incorporated, New York*

We describe a radiative transfer method for treating nongray gaseous absorption and thermal emission in vertically inhomogeneous multiple scattering atmospheres. We derive probability density distributions of absorption coefficient strength from line-by-line calculations to construct line-by-line and band model based  $k$  distributions. The monotonic ordering of absorption coefficient strengths in these  $k$  distributions implicitly preserves the monochromatic structure of the atmosphere at different pressure levels, thus simulating monochromatic spectral integration at a fraction of the line-by-line computing cost. The  $k$  distribution approach also permits accurate modeling of overlapping absorption by different atmospheric gases and accurate treatment of nongray absorption in multiple scattering media. To help verify the accuracy of the correlated  $k$  distribution method, we compare radiative cooling rates by atmospheric water vapor, CO<sub>2</sub>, and ozone against line-by-line calculations. The results show the correlated  $k$  distribution method is capable of achieving numerical accuracy to within 1% of cooling rates obtained with line-by-line calculations throughout the troposphere and most of the stratosphere.

## 1. INTRODUCTION

Accurate determination of atmospheric heating and cooling rates is essential for understanding the radiation balance of the Earth and the changes that occur in climate. Direct measurements are available only for the troposphere, where the radiative flux divergences are largest [e.g., *Smith et al.*, 1977; *Cox and Griffith*, 1979]. Also, the limited sampling in time and space of such in situ measurements precludes global monitoring. Further, in order to usefully interpret measurements of radiative flux divergences, simultaneous knowledge is required of the contributing absorber amounts and their vertical distributions.

Numerically computed radiative heating and cooling rates provide a viable alternative but are subject to additional uncertainties due to the numerical approximations required to make the radiative calculations tractable. The specific problem is the nongray nature of atmospheric absorption due to the large number ( $\sim 10^{5-6}$ ) of spectral lines of the principal absorbing gases (H<sub>2</sub>O, CO<sub>2</sub>, and O<sub>3</sub>) and the large effect that pressure broadening has on spectral line absorption coefficients and thus on the vertical homogeneity of the atmosphere.

Band models have been remarkably successful in their ability to describe gaseous absorption along homogeneous paths in terms of relatively simple statistical formulas based on the mean absorption line strength and half-width distributions [e.g., *Elsasser*, 1942; *Goody*, 1952; *Malkmus*, 1967]. Efforts to apply band model theory to vertically inhomogeneous atmospheres invariably attempt to replace the inho-

mogeneous path with an equivalent homogeneous path, a practice dictated by the lack of viable alternatives, but also one which has theoretical justification only in the weak and strong line limits [*Goody*, 1964].

In its simplest form, the effects of atmospheric pressure broadening are roughly accounted for by scaling the absorber amount with pressure. This type of single-parameter scaling has been widely used in past atmospheric work [e.g., *Howard et al.*, 1956; *Manabe and Moller*, 1961; *Yamamoto*, 1962] and continues to find application in parameterizations for radiative transfer modeling in three-dimensional general circulation models (3-D GCM), where computational speed is essential [cf. *Stephens*, 1984]. One-parameter scaling is often adequate for estimating atmospheric transmission in the troposphere over limited absorber and pressure ranges, but it can lead to large errors in the calculation of atmospheric heating and cooling rates, particularly in the stratosphere and upper troposphere, where errors in the transmission gradient can be substantially larger than errors in the transmission itself [e.g., *Wang*, 1976].

Higher accuracy can be achieved with two-parameter scaling methods such as the procedure originally described by *van de Hulst* [1945] and now more commonly referred to as the Curtis-Godson method [*Curtis*, 1952; *Godson*, 1953]. The Curtis-Godson method is frequently used in atmospheric radiative transfer calculations and is generally considered to produce reliable results. Atmospheric cooling rate computations by *Rodgers and Walshaw* [1966] for H<sub>2</sub>O, CO<sub>2</sub>, and O<sub>3</sub> have served as longtime standards of reference for the Curtis-Godson approximation. A number of modifications to help improve or generalize the two-parameter scaling methods have been suggested [e.g., *Armstrong*,

Copyright 1991 by the American Geophysical Union.

Paper number 90JD01945.  
0148-0227/91/90JD-01945\$05.00

1968; Yamamoto *et al.*, 1972; Lindquist and Simmons, 1972; Young, 1975].

Nevertheless, there are well-known examples of situations in which the Curtis-Godson scaling method fails to provide adequate accuracy. In particular, the inverse pressure-concentration distribution of atmospheric ozone makes it difficult for two-parameter scaling methods to accurately model the radiative cooling by ozone [Goldman and Kyle, 1968]. Also, scaling is inappropriate in situations where the effects of multiple scattering are important. In multiple scattering situations, individual photons traverse different atmospheric path lengths and thus require the application of scaling laws to a distribution of atmospheric paths. The root cause of this failure to provide reliable accuracy for atmospheric heating and cooling rates is the inability of scaling methods to adequately model the pressure-induced changes in the nongray atmospheric absorption.

Nongray gaseous absorption in vertically inhomogeneous atmospheres can be modeled with greater realism using line-by-line calculations; this provides a sounder theoretical basis for computing reliable atmospheric heating and cooling rates [e.g., Fels and Schwartzkopf, 1981]. Comprehensive line parameter tabulations [McClatchey *et al.*, 1973; Rothman, 1981] are available, but the computation cost of line-by-line calculations makes this approach feasible only for limited applications. Since the basic physics of gaseous absorption and pressure broadening are sufficiently well understood, line-by-line calculations can provide a reliable standard of comparison for developing and verifying the accuracy of approximate methods for computing atmospheric heating and cooling rates.

In the following, we describe a computationally efficient numerical procedure for computing heating and cooling rates in vertically inhomogeneous, multiple scattering atmospheres. The procedure involves the grouping by strength of absorption coefficients within a given frequency interval. This procedure results in a " $k$  distribution" of absorption coefficients that requires far fewer points (or subintervals) to represent the spectral absorption than is required for line-by-line computations. For computational convenience, the procedure utilizes the analytical properties of the Malkmus model to convert, in effect, the line-by-line calculated absorption spectra into ordered distributions of absorption coefficient strength, i.e.,  $k$  distributions. This is done by performing a least squares fit of the Malkmus band model parameters to the line-by-line computed absorption over homogeneous paths for prescribed pressures, temperatures, and absorber amounts.

The effects of vertical inhomogeneity (e.g., pressure broadening) are modeled through the implicit wavelength correlation of  $k$  distributions at different pressure levels, which is presumed to hold throughout the atmosphere. The physical basis for this premise is that, for a given spectral interval  $[\nu_1, \nu_2]$ ,  $k$  distributions at all altitudes are simply correlated in frequency space, i.e., the monotonic ordering by strength of absorption coefficients at different levels in the atmosphere retains the relative spectral alignment of absorption lines between different levels. Clearly, for an isolated absorption line, this spectral correlation is rigorously maintained through all levels of the atmosphere as long as the line center remains fixed in wavelength. The degree to which this spectral correlation can be maintained in a realistic atmosphere for gaseous spectra with overlapping lines of different

strength is not readily obvious and is the key topic addressed in this paper.

The principal advantages of the correlated  $k$  distribution approach are its numerical efficiency and its computational speed in modeling nongray absorption by gases in vertically inhomogeneous atmospheres and the ability to include multiple scattering rigorously at a fraction of the computational cost of line-by-line calculations. For a spectral interval of arbitrary width, only two band model parameters (least squares fitted at a given pressure and temperature) are needed to describe the essential aspects of nongray line-by-line spectral information. The  $k$  distribution approach also permits an accurate simulation of the overlapping absorption by different gases and of multiple scattering effects in the presence of nongray absorption. Moreover, the correlated  $k$  distribution method permits a "stacked-layer" approach for computing multilayered atmospheres (where computation time is linearly proportional to the number  $N$  of atmospheric layers). Other methods, on the other hand, often require transmission function matrix multiplication for different groupings of layers (for which the computation time is proportional to  $N^2$ ). Comparison of radiative cooling rates calculated using the Malkmus model based correlated  $k$  distribution method to those calculated using line-by-line techniques indicates a practical capability to achieve numerical accuracy to within  $\sim 1\%$  throughout the troposphere and most of the stratosphere. The only important occurrence that we find where empirical correction is needed to maintain the accuracy of radiative cooling rates computed with the correlated  $k$  distribution approach, is in the case of overlapping absorption between  $\text{CO}_2$  and  $\text{H}_2\text{O}$  within the 5- to 30-mbar region, where poor vertical correlation of  $k$  distributions is aggravated by rapidly changing relative absorber amounts.

We describe in section 2 our basic approach of using line-by-line calculations to obtain  $k$  distributions numerically, and to upgrade band model accuracy by least squares fitting of band model parameters to line-by-line results. In sections 3 and 4 we describe the Malkmus band model distribution functions and their application in modeling and correlating  $k$  distributions in a vertically inhomogeneous atmosphere. In section 5 we compare the radiative cooling rates of the principal atmospheric gases obtained line-by-line with those computed using the correlated  $k$  distribution method. In section 6 we discuss the utility of the  $k$  distribution approach in multiple scattering situations and illustrate the combined effect of multiple scattering and nongray absorption. The overall utility of the correlated  $k$  distribution method and its application to atmospheric radiative calculations is discussed in section 7; additional details of comparisons to the line-by-line calculations and of the treatment of overlapping absorption are given in Appendix B.

We have tested the correlated  $k$  distribution method in a number of one-dimensional (1-D) climate modeling applications [e.g., Wang *et al.*, 1976; Hansen *et al.*, 1978, 1981; Lacis *et al.*, 1981]. A parameterized version of the correlated  $k$  distribution is used to compute atmospheric heating and cooling rates in the Goddard Institute for Space Studies (GISS) 3-D climate model [Hansen *et al.*, 1983, 1984; Rind *et al.*, 1988] and to model radiative forcing of the global surface temperature due to gradual changes in trace gas concentrations in the study of transient climate response [Hansen *et*

*al.*, 1988]. In all of these applications the  $k$  distribution approach has proved itself both versatile and reliable.

## 2. ABSORPTION IN HOMOGENEOUS MEDIA

For radiative transfer purposes, "homogeneous" requires only that the monochromatic absorption coefficient  $k_\nu$  be constant along the light beam path, a requirement that is generally met for atmospheric paths at constant pressure and temperature. For constant  $k_\nu$ , the integral over the absorber density  $\rho$  along the atmospheric path simplifies to  $u = \int \rho(z) dz$ , and the spectrally integrated transmission function can be written in its conventional form

$$T(u) = \frac{1}{\nu_2 - \nu_1} \int_{\nu_1}^{\nu_2} \exp(-k_\nu u) d\nu \quad (1)$$

Two general approaches exist that utilize compilations of atmospheric line parameter data to compute transmission (or absorption) functions for homogenous paths. Monochromatic line-by-line calculations use the line parameters directly and are generally regarded to be a "precise" but computationally costly approach. Band model methods, which express the transmission analytically in terms of band model parameters that are based on the statistical distribution of absorption lines, offer computational economy and numerical convenience but at the cost of reduced precision.

As described below, line-by-line calculations serve two basic objectives: first, they provide the means for determining the dependence of transmission and/or absorption on absorber amount; second, by ranking the line-by-line calculated absorption coefficients by strength, they provide a numerical distribution of absorption coefficient strengths that we identify as the " $k$  distribution." The band models also possess intrinsic  $k$  distribution representations defined in terms of their band model parameters.

For our line-by-line calculations, we use the absorption line strengths, half widths, energy levels, and line positions from the 1982 Air Force Geophysics Laboratory (AFGL) atmospheric line compilation [Rothman, 1981]. To model the effect of pressure broadening on line shape, we use the Voigt profile throughout the atmosphere [e.g., Drayson, 1975; Pierluissi *et al.*, 1977]; line wings are truncated  $5 \text{ cm}^{-1}$  from the line center. The spectral resolution used is  $0.005 \text{ cm}^{-1}$  below 15 km, and  $0.0005$  above 15 km. We utilize several optimizations to reduce computing time but maintain computational accuracy to within several tenths of a percent compared to more time consuming calculations that use numerical overkill to overcome such problems as spectral resolution. For example, absorption lines that are too weak to contribute significant absorption over the range of absorber amounts of interest are eliminated, and we combine closely spaced overlapping lines. The full pressure and temperature dependence of absorption line shapes as well as line wing contributions from outside the immediate spectral interval are explicitly included in the calculations. A more detailed description of our procedure for computing line-by-line absorption is given by Oinas [1983].

### 2.1. Absorption Coefficient Frequency Distribution

Since  $k_\nu$  is a highly repetitive function of wavelength, computational efficiency can be improved by replacing the

integration over wavelength with a reordered grouping of spectral subintervals with similar absorption coefficient strength. The basic idea of grouping spectral intervals according to absorption coefficient strengths is not new [e.g., Ambartzumian, 1936; Lebedinsky, 1939]. More recently, the same principle has been applied to radiative problems in the terrestrial atmosphere [Altshuler and King, 1968; Kondratyev, 1969; Yamamoto *et al.*, 1970; Arking and Grossman, 1972; Lacis and Hansen, 1974; Chou and Arking, 1980; Wang and Shi, 1988].

The basic approach is illustrated in Figure 1 for a sample absorption coefficient spectrum computed for the  $1510\text{--}1520 \text{ cm}^{-1}$  section of the  $6.3\text{-}\mu\text{m}$  water vapor band. The spectrum in Figure 1a was calculated for a pressure of 10 mbar and temperature 240 K; the comparison spectrum in Figure 1c was calculated for 1 bar and 296 K. The spectra contain overlapping absorption from 141 lines within the  $1510\text{--}1520 \text{ cm}^{-1}$  spectral interval and include wing contributions from lines extending  $5 \text{ cm}^{-1}$  beyond the interval. The resulting absorption coefficient spectra are then used to determine the frequency distributions of absorption coefficient strengths, shown in Figures 1b and 1d, and to compute transmission as a function of absorber amount.

The absorption coefficient range is subdivided into a suitable number of subintervals, or bins ( $N \sim 10^{1-2}$  per decade of absorption coefficient strength) of specified width  $\Delta k_i$ ; this also serves to define the resolution in  $k$  space for tabulating the absorption coefficient frequency distribution. To resolve the absorption coefficient spectrum, particularly in cases of small pressure and large line strength, a large number of spectral subintervals ( $M \sim 10^{3-5}$  per wave number) may be required. Linear interpolation is used between computed points of the spectrum in order to bin wavelength subintervals that extend beyond local absorption coefficient bin boundaries. Thus the frequency distribution of absorption coefficient strengths is obtained directly from the absorption coefficient spectrum by binning and summing wavelength subintervals  $\Delta\nu_j$ , which have absorption coefficient strengths within a specified range between  $k_i$  and  $k_i + \Delta k_i$  (see Figure 1c).

$$f(k_i) = \frac{1}{\nu_2 - \nu_1} \sum_j^M \left| \frac{\Delta\nu_j}{\Delta k_i} \right| W(k_i, k_i + \Delta k_i) \quad (2)$$

where  $W(k_i, k_i + \Delta k_i)$  is a "window" function that is zero everywhere except in the interval between  $k_i$  and  $k_i + \Delta k_i$ , where it is equal to unity. The absolute value designation in (2) accommodates the change in sign associated with increasing and decreasing absorption coefficient strengths within spectral subintervals. The frequency distribution is normalized to unity over the given spectral interval  $[\nu_1, \nu_2]$ ; hence the cumulative frequency distribution increments,  $\Delta g_i = f(k_i) \Delta k_i$ , define the fraction of the interval  $[\nu_1, \nu_2]$  for which the absorption coefficient  $k_\nu$  is between  $k_i$  and  $k_i + \Delta k_i$ . A similar approach was used by Arking and Grossman [1972] to obtain absorption coefficient frequency distributions for portions of the  $\text{CO}_2$  band.

The characteristic spikes in Figures 1b and 1d, that occur throughout the absorption coefficient range, arise from local maxima and minima in the  $k_\nu$  spectrum where small changes of  $\Delta k_i$  are associated with large changes of wavelength subintervals  $\Delta\nu_j$ , causing the apparent discontinuities in  $f(k)$ . These spikes can be readily associated with the tops of

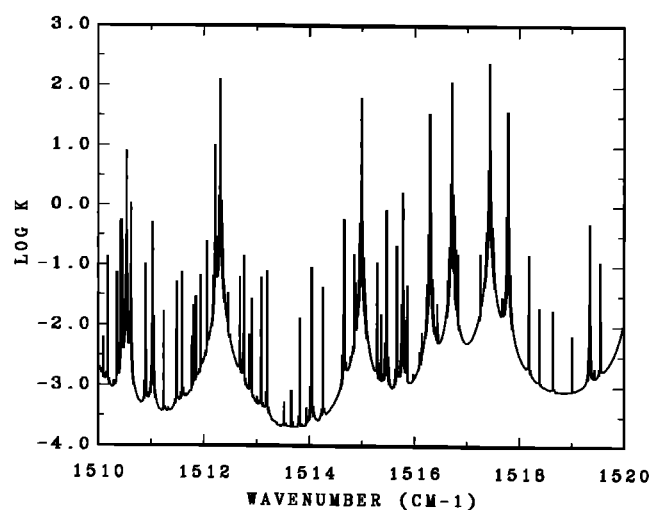


Fig. 1a

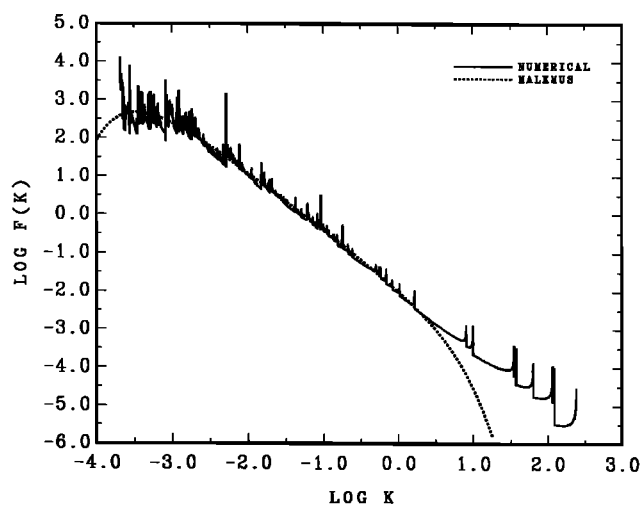


Fig. 1b

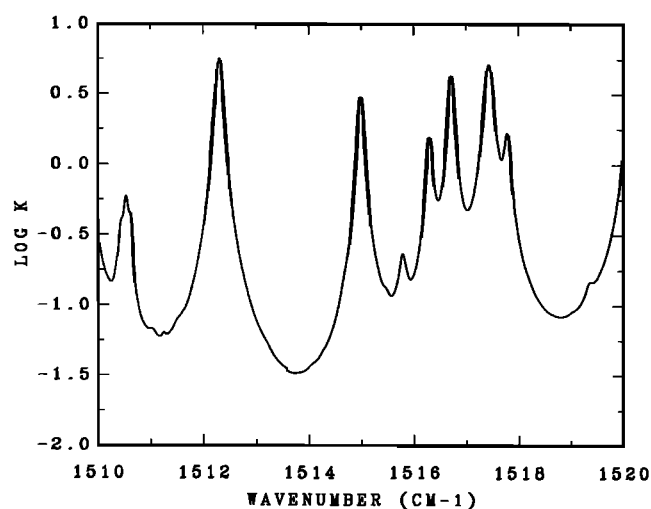


Fig. 1c

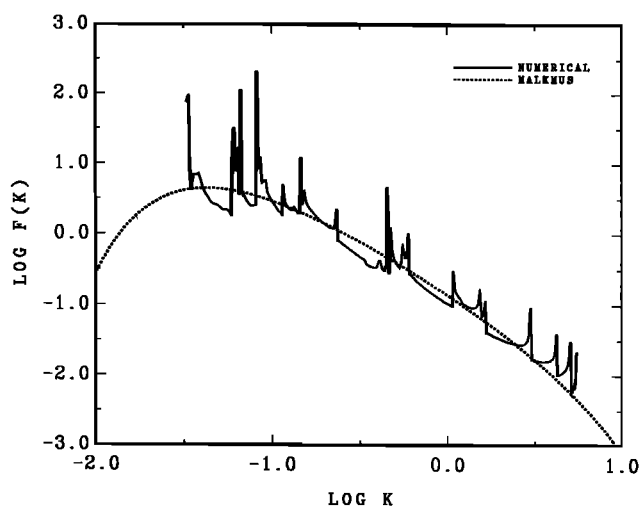


Fig. 1d

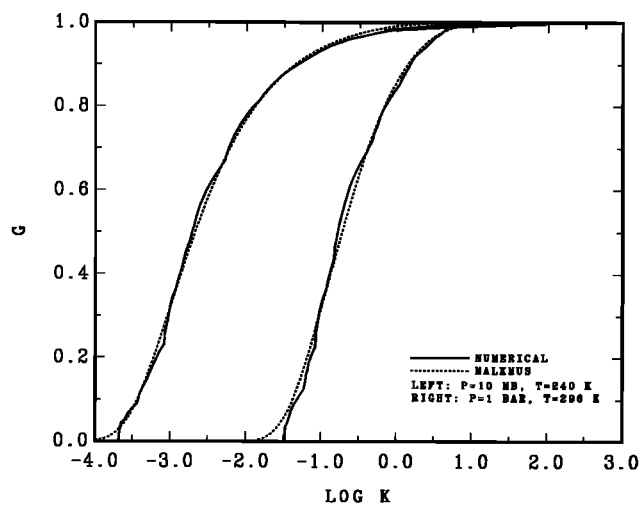


Fig. 1e

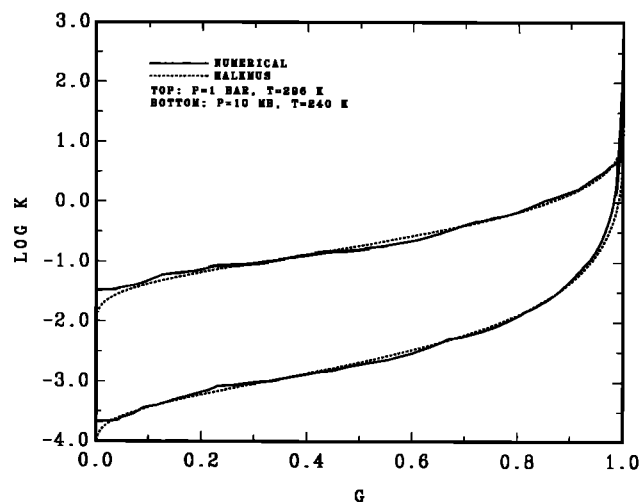


Fig. 1f

Fig. 1. Absorption coefficient spectrum for the 1510–1520  $\text{cm}^{-1}$  portion of the 6.3- $\mu\text{m}$  water vapor band. (a) Line-by-line absorption coefficients for a pressure of 10 mbar and temperature 240 K and (c) for a pressure of 1 bar and 296 K. The spectra utilize the AFGL 1982 atmospheric line compilation [Rothman, 1981] and include 141 lines with absorption contributions from outside of the interval within a 5  $\text{cm}^{-1}$  Lorentz wing cutoff limit. (b and d) Absorption coefficient frequency distributions corresponding to absorption spectra in Figures 1a and 1c, respectively. (e) Cumulative frequency distributions of the absorption coefficient spectra in Figures 1a and 1c. (f) The  $k$  distributions of the absorption coefficient spectra Figures 1a and 1c. Malkmus band model equivalents, obtained to provide best fit to line-by-line transmission, are shown by dashed lines.

the stronger absorption lines in Figures 1a and 1c. The amplitude of the spikes is resolution dependent, i.e., they depend on the size of the  $\Delta k_i$  intervals. The frequency distribution in Figure 1b exhibits a characteristic  $k^{-3/2}$  slope, a common feature at low pressures. Note that this portion of the frequency distribution, though ostensibly significant in appearance, contributes very little to the total absorption (except over extremely long path lengths). The characteristic slope arises from Lorentz wing absorption, which in the low-pressure regime, dominates the “empty” portion of the spectral interval as the line cores become increasingly narrow and constitute but a tiny fraction of the total spectral interval.

The predominance of Lorentz wing absorption in low-pressure  $k$  distributions does not mean that Lorentz wings will account for most of the absorption. Rather, this emphasizes the point that, in a particular case, only a small portion of the total  $k$  distribution (the region where the product of  $k$  and absorber amount is near unity) is actively contributing. Only for extremely large absorber paths do these small-value absorption coefficients come into play.

For subsequent numerical applications, it is more convenient to express the absorption coefficient strength distribution in terms of a cumulative frequency distribution, i.e.,

$$g(k_n) = \sum_{i=1}^n f(k_i) \Delta k_i \quad (3)$$

and its inverse,

$$k_n(g) = g^{-1}(k_n) \quad (4)$$

The profiles of the cumulative frequency distribution (shown in Figure 1e) and its inverse (Figure 1f) are free of the discontinuities present in the frequency distribution and are thus more amenable to numerical handling.

The inverse of the cumulative frequency distribution,  $k(g)$ , is what we define as the “ $k$  distribution.” Transformation of the absorption coefficient spectrum into the  $k(g)$   $k$  distribution produces a pseudo-absorption line profile that has the same nongray transmission properties (within the spectral interval  $\Delta\nu$ ) as the original absorption coefficient spectrum. This follows because the  $k$  distribution profile is simply the result of the line spectrum absorption coefficients being regrouped and ranked according to absorption coefficient strength. The  $g$  coordinate is roughly analogous to a normalized wavelength coordinate, and integration over  $g$  is equivalent to integration over frequency. (For the equivalence to hold, there is, of course, the implicit assumption that the incident flux is spectrally uniform across the interval  $[\nu_1, \nu_2]$ ). The cumulative frequency distribution  $g(k)$  serves as the abscissa of the  $k$  distribution; it represents (ordered) fractional segments of the spectral interval  $[\nu_1, \nu_2]$ . As required by the normalization of  $f(k)$ ,  $g(k)$  is defined over the range  $[0, 1]$ , and thus represents a normalized wavelength coordinate.

The dashed comparison curves in Figures 1b, 1e, and 1f (also in Figure 2) are Malkmus band model equivalents for the frequency distribution, the cumulative frequency distribution, and the inverse cumulative frequency distribution, respectively. Defined in terms of (Malkmus) band model parameters, they represent an indirect fit to the line-by-line distribution functions. As described more fully in the follow-

ing sections, band model parameters are least squares fitted to the line-by-line transmission calculations. That the resulting band model distribution functions closely match the line-by-line frequency distributions is indicative of the degree to which the band model statistical parameters describe the line spectrum. The regions of closest  $k$  distribution fit reflect the range of absorber amount over which the band model transmission was least squares fitted to reproduce the line-by-line results.

Comparison of the high- and low-pressure  $k$  distributions in Figures 1e and 1f shows that the  $k$  distribution profiles respond to pressure broadening in a manner similar to that of individual spectral lines. At low pressure, the line shapes are no longer Lorentzian, and the range of absorption coefficient strength (as evident in the line spectra and the resulting frequency distributions) spans nearly 6 orders of magnitude. There is a narrow core of very strong absorption, with the bulk of the interval characterized by orders of magnitude weaker line wing absorption. At high pressure, the contrast between the strongest and weakest absorption becomes much reduced, as is the case for individual spectral lines. For fixed line strengths within the interval  $[\nu_1, \nu_2]$ , the  $k$  distribution profile changes shape with pressure, but the area under the  $k$  distribution curves is invariant. Utilization of these pseudo-absorption line characteristics of the  $k$  distributions to model absorption along inhomogeneous paths is described in section 4.

Figure 2 shows the same transformation of the absorption coefficient spectrum into its  $k$  distribution, or equivalent pseudo-absorption line form, for the 660–670  $\text{cm}^{-1}$  section of the 15- $\mu\text{m}$   $\text{CO}_2$  band. As in Figure 1, we compare a low-pressure case of 10 mbar and temperature 240 K and a high-pressure case of 1 bar and 296 K. In this example, the spectral lines exhibit bimodal bunching and thus are less randomly distributed than lines in the  $\text{H}_2\text{O}$  spectrum discussed above. There are 1856 lines within the 660–670  $\text{cm}^{-1}$  interval; again, line wing contributions from within 5  $\text{cm}^{-1}$  external to the interval are included. As in Figure 1b for water vapor, the frequency distribution in Figure 2b exhibits the characteristic  $k^{-3/2}$  Lorentz wing slope. Though the number of lines and line distributions are very different for the water vapor and  $\text{CO}_2$  spectra, the corresponding frequency and  $k$  distributions show characteristic similarity, indicating the predominant importance of common factors, i.e., randomly overlapping Lorentz or Voigt line profiles with common response to pressure changes.

Having transformed the absorption coefficient spectrum into a frequency distribution, we now can develop alternative expressions for computing the transmission functions:

$$T(u) = \sum_i^N f(k_i) e^{-k_i u \Delta k_i} \quad (5)$$

and

$$T(u) = \sum_i^N e^{-k_i u \Delta g_i} \quad (6)$$

where  $k_i(g)$  is the inverse cumulative frequency distribution, or  $k$  distribution, given by (4), and  $\Delta g_i = f(k_i) \Delta k_i$ . Generalized in the limit of small intervals, the transmission function in (5) becomes a transmission integral over the density distribution of absorption coefficient strengths:

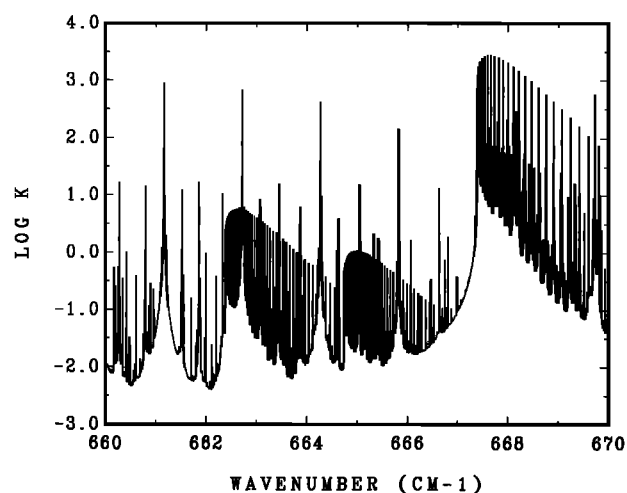


Fig. 2a

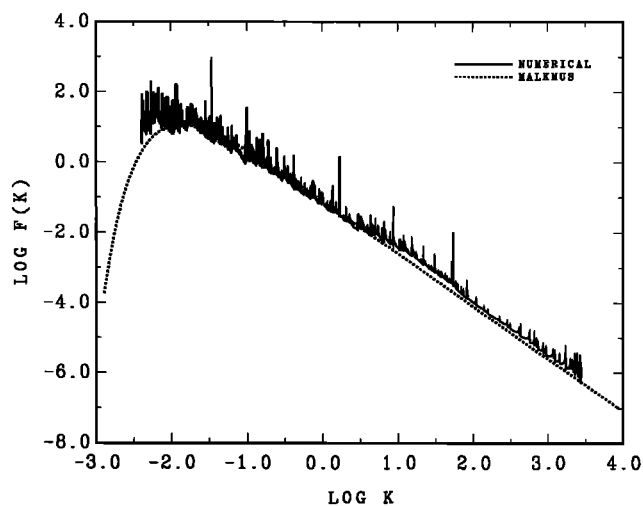


Fig. 2b

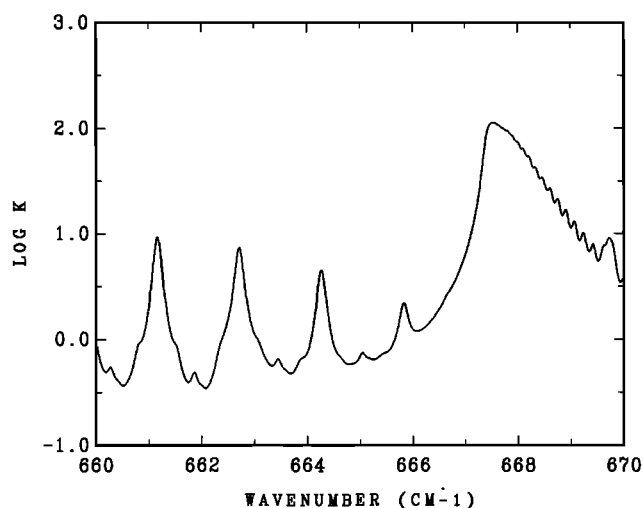


Fig. 2c

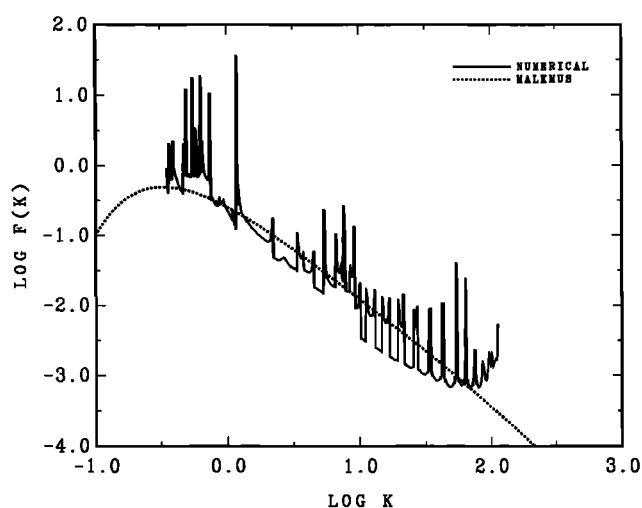


Fig. 2d

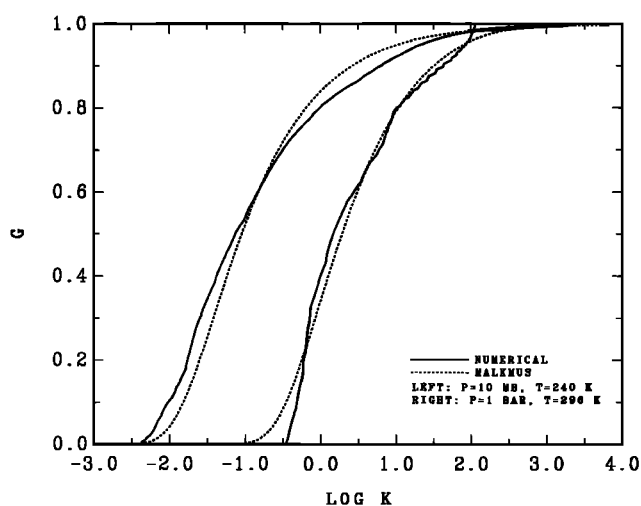


Fig. 2e

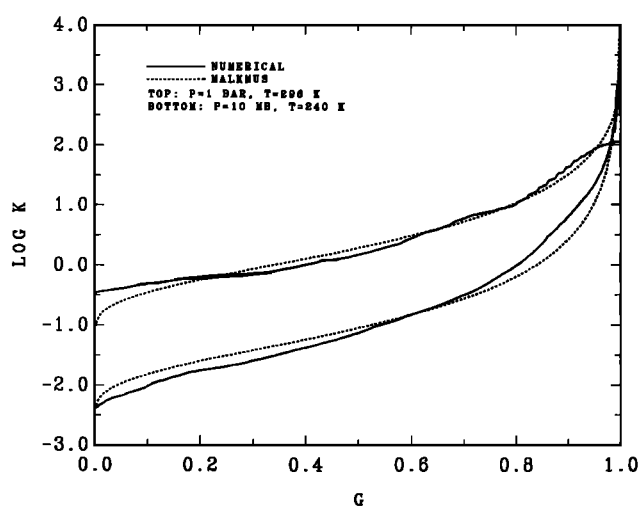


Fig. 2f

Fig. 2. Absorption coefficient spectrum for the 660–670  $\text{cm}^{-1}$  portion of the 15- $\mu\text{m}$   $\text{CO}_2$  band. (a) Line-by-line absorption coefficients for a pressure of 10 mbar and temperature of 240 K and (c) for 1 bar and 296 K. (b and d) Corresponding frequency distributions; (e) cumulative frequency distributions, and (f)  $k$  distributions as in Figure 1. Malkmus band model equivalents, obtained to provide best fit to line-by-line transmission, are shown by dashed lines.

$$T(u) = \int_0^\infty f(k) e^{-ku} dk \quad (7)$$

Likewise, the transmission integral over the inverse cumulative density distribution yields

$$T(u) = \int_0^1 e^{-k(g)u} dg \quad (8)$$

So far, no approximations have been introduced. For a homogeneous path, transmission can be computed using line-by-line spectral integration as in (1), by integrating over the frequency distribution as in (7), or by integrating over the  $k$  distribution as in (8). In all three cases the multiplicative property of monochromatic transmission holds, i.e.,  $T(u_1 + u_2; g) = T(u_1; g) \times T(u_2; g)$ . While all three approaches produce the same transmission results for a given absorber range, performing the integration over the  $k$  distribution is clearly simpler for numerical evaluation. Of course, for one-time applications, there is no real advantage to using  $k$  distributions, since line-by-line calculations are required to obtain the  $k$  distribution in the first place.

The transmission formula in (7) has the standard form of a Laplace transform. This is of special significance, as it permits the probability density distribution of the absorption coefficient strengths to be formally identified as the inverse Laplace transform of the transmission function, i.e.,  $f(k) = L^{-1}[T(u)]$ . In the following sections, this relationship is used to derive analytic expressions for the probability density distributions and  $k$  distributions directly from band model transmission functions.

## 2.2. Band Model Transmission

Band models provide convenient analytic expressions for computing the transmission function over homogeneous paths and over a wide range of absorber amounts. The only question is the accuracy with which they reproduce line-by-line transmission results. The Malkmus [1967] band model transmission function is a two-parameter formula:

$$T(u) = \exp \{ -\pi B/2[(1 + 4Su/\pi B)^{1/2} - 1] \} \quad (9)$$

where  $B$  is the effective line half width and  $S$  is the effective line strength. The parameters  $B$  and  $S$  are related, in turn, to three statistical line spectrum parameters ( $s$ ,  $b$ , and  $d$ ) by the relations  $B = b/d$  and  $S = s/d$ , where  $b$  is the mean absorption line half width,  $s$  is the mean absorption line strength, and  $d$  is the mean line spacing. These three statistical parameters can be obtained directly from line data such as the AFGL atmospheric line compilation [Rothman, 1981]. For the band model to correctly reproduce transmission in the optically thin limit,  $T(u) = e^{-Su}$ , it is required that the mean line strength be

$$s = \frac{1}{N} \sum_i s_i \quad (10)$$

Likewise, agreement in the optically thick limit,  $T(u) = \exp [-(\pi BSu)^{1/2}]$ , requires that the mean line half width be

$$b = \frac{4}{\pi s} \left[ \frac{1}{N} \sum_i (s_i b_i)^{1/2} \right]^2 \quad (11)$$

The mean line spacing is given by

$$d = \Delta\nu/N \quad (12)$$

where  $N$  is the number of absorption lines within the spectral interval  $\Delta\nu$ . The pressure and temperature dependence in line-by-line calculations is included explicitly within the  $s_i$  and  $b_i$  parameter definitions through the line intensity partition functions, Boltzmann factor, and Voigt line shape [McClatchey *et al.*, 1973], i.e.,

$$s_i = s_{i0} \frac{V_0 R_0}{VR} \exp \left[ \frac{hc}{k} E'' \left[ \frac{1}{T_0} - \frac{1}{T} \right] \right] \quad (13)$$

and

$$b_i = b_{i0} \frac{P}{P_0} \left[ \frac{T_0}{T} \right]^n \quad (14)$$

where  $s_{i0}$  and  $b_{i0}$  are the tabulated values of line intensity and line half width at reference pressure  $P_0$  and reference temperature  $T_0$ , respectively, and where  $h$  is Planck's constant,  $c$  is the speed of light,  $k$  is Boltzmann's constant, and  $E''$  is the energy of the lower state of the transition. The coefficient of temperature dependence  $n$  is normally approximated as  $n = 0.5$ , unless other information is available. The temperature dependence of the vibrational partition function  $V/V_0$  is close to unity, and that of the rotational partition function  $R/R_0$  is  $(T/T_0)^j$ , with  $j$  equal to 1.0 or 1.5, depending on the type of molecule, both tabulated by McClatchey *et al.* [1973].

The above expressions provide a convenient recipe for converting atmospheric line tabulations into transmissions without having to resort to line-by-line computations; however, the accuracy of these band model transmissions is unacceptably low. Typical errors in the troposphere are 10–20%, becoming worse with altitude. Basically, whenever line shapes and/or line distributions deviate significantly from the “randomly distributed, overlapping Lorentz lines with exponentially tailed  $s^{-1}$  line-strength distribution” premise of the Malkmus band model parameter definition, large errors in transmission and absorption can be expected.

This deficiency can be compensated for by least squares fitting the band model parameters to line-by-line calculations. This transfers the accuracy of line-by-line calculations to band model transmissions, so that the inherent capability of band models to describe gaseous absorption over a wide range of absorber amounts (for homogeneous paths) is more fully utilized. The fitting of the Malkmus band model parameters to the line-by-line calculated transmission is a nonlinear least squares problem and requires some care, as no standard fitting procedure is guaranteed to work in all cases. However, in practice, whenever the statistical parameters provide a reasonably accurate estimate for the transmission, little iteration is required to obtain the best fit band model parameters. Typical examples of the least squares parameter fits to line-by-line data are shown in Figure 3.

We compute line-by-line transmission (solid circles in Figure 3) as a function of absorber amount by starting with a small initial value and doubling the absorber until the desired absorber range is covered. The dashed lines show the band model transmission obtained with the statistical band model parameters given by (10)–(12); the solid lines depict the improvement gained by using the least squares fitted band

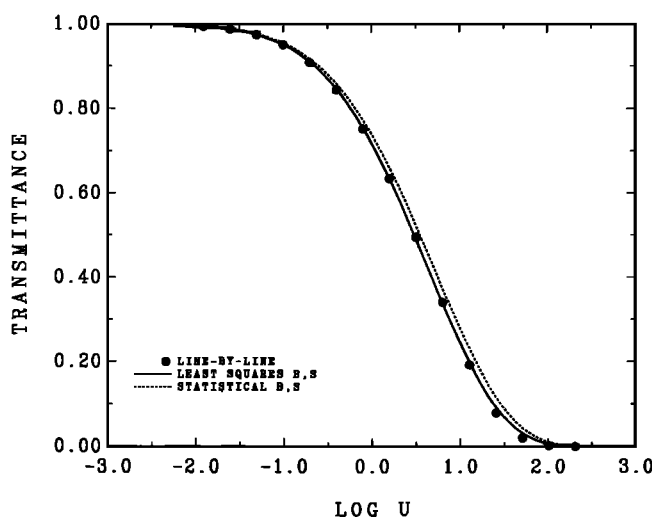


Fig. 3a

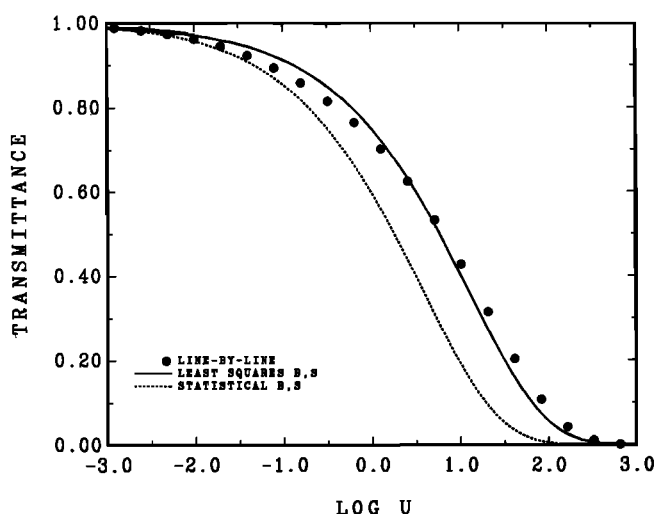


Fig. 3b

Fig. 3. Least squares fit of Malkmus band model parameters to line-by-line transmission. Solid circles depict line-by-line results. Least squares fit results are shown by solid lines, while transmissions obtained from statistical Malkmus parameters are shown by dashed lines. (a) Results for the 1510–1520  $\text{cm}^{-1}$  portion of the 6.3- $\mu\text{m}$  water vapor band at 1-bar pressure and 296 K. (b) Results for the 660–670  $\text{cm}^{-1}$  portion of the 15- $\mu\text{m}$   $\text{CO}_2$  band at 10-mbar pressure and 240 K.

model parameters. The results in Figure 3a are for the 1510–1520  $\text{cm}^{-1}$  section of the 6.3- $\mu\text{m}$  water vapor band at 1-bar pressure; the dashed line fit to the line-by-line results somewhat overestimates the transmission, but otherwise indicates that within this spectral interval, the statistical band model parameters fairly closely describe the line spectrum.

Figure 3b shows the transmission fit for the 660–670  $\text{cm}^{-1}$  section of the 15- $\mu\text{m}$   $\text{CO}_2$  band at a pressure of 10 mbar (shown in Figure 2b), which presents a more difficult case to fit with the Malkmus model. Here, the statistical band model parameters provide a very poor initial fit to the line-by-line transmission because the statistical criteria assumed for the Malkmus model are not satisfied, i.e., the selected  $\text{CO}_2$  spectrum is characterized by nonoverlapping Voigt lines

with a bimodal line strength distribution. Nevertheless, as shown by the solid line, the least squares fitted band model parameters greatly improve the accuracy, but over a limited range of absorber amount.

Of the two band model parameters, the effective line strength parameter  $S$  is usually better represented by statistical averages of the line data compared to the effective half width parameter  $B$ . Having already computed the line-by-line transmission as a function of absorber amount, we can invert the transmission directly at each absorber amount point to obtain the corresponding Malkmus model optical depths, i.e.,

$$\tau_i = \frac{\pi B_i}{2} [(1 - 4Su_i/\pi B_i)^{1/2} - 1] \quad (15)$$

Assuming  $S$  is given by  $S = s/d$ , we obtain a series of estimates for the  $B$  parameter:

$$B_i = \frac{\tau_i^2}{\pi} (Su_i - \tau_i)^{-1} \quad (16)$$

Generally, the  $B_i$  vary with absorber amount  $u_i$  unless the model parameters happen to precisely fit the line-by-line transmission. In averaging the  $B_i$ , greater weight is given to those values where  $Su_i/B_i$  is large, since this ratio determines the degree to which the lines are saturated. Further, since the band model cannot fit the entire range of absorber amount with uniform precision, the weight assignment is used to force the region of optimum fit to coincide with the range of interest. Typically, an absorber range covering a factor of 32 in absorber amount is adequate for most atmospheric applications.

Contour plots depicting the percent error in fitting the line-by-line transmission over the selected absorber range help to illustrate the nature of the least squares fitting problem. Figure 4a shows the fitting error for the 1510–1520  $\text{cm}^{-1}$  section of the 6.3- $\mu\text{m}$  water vapor band at 1-bar pressure for different combinations of the Malkmus model  $B$  and  $S$  parameters. The triangle identifies the initial starting point of the least squares fit at  $B = b/d$  and  $S = s/d$ , based on the statistical band model parameters given by (10)–(12). Because this initial guess may occasionally be too far removed for a two-parameter iteration to converge (as is the case for the  $\text{CO}_2$  example in Figure 4b), we sample a broad mesh of  $S$  values in the neighborhood of the statistical average value with one-parameter iterations on  $B$ . Of these, the best fit point, indicated by the square, is selected as the starting point for further iteration, for which we use a two-parameter Newton-Raphson procedure. The circle denotes the optimum iterated  $B$  and  $S$  parameters for the Malkmus model, which give the minimum fitting error to the line-by-line transmission over the specified absorber range. For the 6.3- $\mu\text{m}$  water vapor example, the mean fractional error for absorption over nearly the full absorber range in Figure 3a is less than 1%.

In Figure 4b the percent error contours refer to different combinations of band model parameters used in fitting the 660–670  $\text{cm}^{-1}$  section of the 15- $\mu\text{m}$   $\text{CO}_2$  band at 10-mbar pressure and 240 K. In this example, for the absorber range of interest, the principal absorption lines are already saturated; thus the least squares fit is effectively a one-parameter fit to the product of  $BS$ . Here, the initial estimate (triangle)



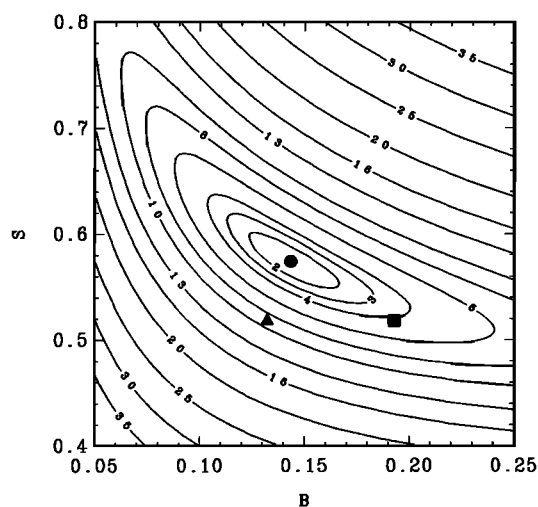


Fig. 4a

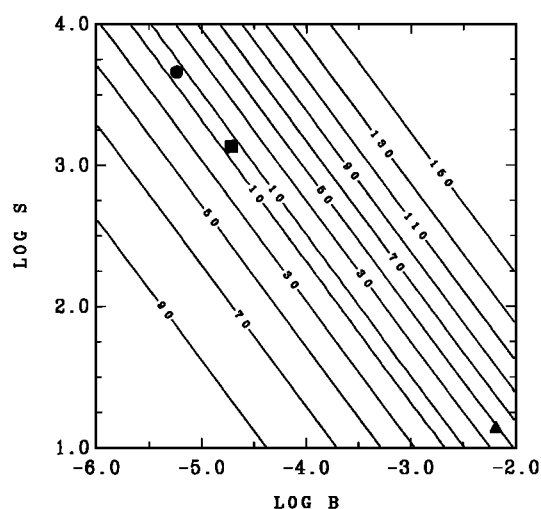


Fig. 4b

Fig. 4. Percent error in fitting Malkmus parameters to line-by-line transmission. Contours in  $BS$  plane depict root-mean-square error in absorbance fit to line-by-line results in Figure 3. (a) Results of water vapor transmission and (b) for  $\text{CO}_2$ . Triangles depict statistical  $B$ ,  $S$  values, while squares represent the best  $B$ ,  $S$  pair in which  $B$  is derived by least squares for a discrete set of  $S$  values. The solid circles depict the best fits by least squares iteration of both  $B$  and  $S$ .

based on the statistical parameter values results in a poor fit (see Figure 3b). Coarse mesh sampling with iterations on  $B$  locates the trough in the  $BS$  plane, where the error contours are set by the product of  $B$  and  $S$ , and obtains a better fit (square). Further two-parameter iteration locates the minimum error point (circle) within the trough. In this case, the least squares fitted parameters are very different from the initial statistical parameters, but the fitting error has been greatly reduced with a mean fractional error in absorption of  $\sim 6\%$  within the selected absorber range of 1–32 cm (STP).

The above demonstrates the ability of the Malkmus model to reproduce line-by-line transmissions over homogeneous paths with good accuracy. Typically, within the troposphere and over much of the stratosphere, band model transmissions can be least squares fitted to within  $\sim 1\%$  of line-by-line

results for the principle atmospheric gases for absorber ranges spanning a factor of 30 or more in absorber amount. Several exceptions that are difficult for the Malkmus model to represent accurately, i.e., isolated single lines and Doppler line shapes, are discussed in section 3.5.

The closest transmission fits are obtained at the larger (tropospheric) pressures, where it is more likely that the band model criteria of overlapping Lorentz lines with  $s^{-1}$  line strength distribution are more fully satisfied. The accuracy of the fitted transmission is not particularly sensitive to the width of the spectral interval for widths ranging from 1 to  $100 \text{ cm}^{-1}$  as long as sharp band edges, which produce a bimodal strength distribution, are not included in the spectral interval, and as long as line wing contributions from strong lines external to the selected spectral interval are included. The accuracy and/or the absorber range over which an adequate fit can be obtained decrease with pressure as the absorption characteristics of the spectrum tend toward those of Doppler line shape.

Other band models (e.g., the Goody and Elsasser models) could have been used with equal success to obtain accurate least squares fits to line-by-line transmission. The practical reason for using the Malkmus model is because of its analytical properties that facilitate manipulation of  $k$  distributions as discussed below.

### 3. MALKMUS BAND MODEL DISTRIBUTION FUNCTIONS

For applications that require only the transmission over homogeneous paths in the absence of scattering, band model transmission results (with least squares fitted parameters) provide good accuracy. However, when modeling multiple scattering, or the vertical inhomogeneity of the atmosphere, accurate knowledge of the mean transmission alone is insufficient; full knowledge of the nongray information describing the distribution of absorption coefficient strengths is essential because the nonlinear dependence of multiple scattering interactions on absorption coefficient strength is very difficult to simulate accurately by using only spectral-mean absorption coefficients.

This nongray information is available in the numerical frequency distributions (e.g., Figure 1b) that were computed directly from the line spectrum. Unfortunately, these numerical  $k$  distributions are computationally unwieldy due to the large number of points required to represent the absorption coefficient frequency distribution. The band model  $k$  distributions offer simplicity, but two key questions must be addressed: (1) to what extent is nongray information describing the distribution of absorption coefficient strengths contained within the band model formulation; and (2) can this information be extracted in a form that is useful for application to practical radiative transfer problems.

#### 3.1. Density Distribution of Absorption Coefficient Strengths

The formal definition of the transmission function as the Laplace transform of the absorption coefficient probability density distribution in (7) implies that the full information content of the nongray distribution of absorption coefficient strengths is contained within the band model transmission function. Thus, to the extent that the band model transmission function (e.g., the Malkmus model given by (9)) accu-

ately describes the line-by-line transmission over the full range of absorber amount, the inverse Laplace transform of the band model transmission function should reproduce the absorption coefficient probability density distribution. Of the commonly used band models, *Domoto* [1974] showed that the Malkmus model possesses an inverse Laplace transform that is mathematically well suited for further manipulation. Sometimes also referred to as the inverse transmission, the Malkmus model probability density distribution of absorption coefficient strengths (the inverse Laplace transform of (9)) is

$$f(k) = \frac{1}{2} k^{-3/2} (BS)^{1/2} \exp \left[ \frac{\pi B}{4} \left( 2 - \frac{S}{k} - \frac{k}{S} \right) \right] \quad (17)$$

where  $f(k)$  is a normalized distribution function, i.e.,

$$\int_0^\infty f(k) dk = 1 \quad (18)$$

with a peak value at

$$k_{\max} = \frac{3S}{\pi B} [(\pi B/3)^2 + 1]^{1/2} - 1 \quad (19)$$

The mean value of absorption coefficient strength is equal to the effective line strength parameter  $S$ ,

$$\bar{k} = \frac{\int_0^\infty kf(k) dk}{\int_0^\infty f(k) dk} = S \quad (20)$$

The overall shape of the density distribution is characterized by a  $k^{-3/2}$  power law dependence with exponential cutoffs at both small and large values of  $k$ .

Some of the characteristic features of the probability density distribution  $f(k)$  are shown in Figure 5a as  $B$ , the effective half width parameter, is varied from typical stratospheric values ( $B \sim 10^{-3}$ ) to values characteristic of the ground surface ( $B \sim 0.1$ ), and to much larger values; the effective line strength parameter in these comparisons is fixed at  $S = 1$ . The characteristic  $k^{-3/2}$  power law slope, which results from the Lorentz line-shape assumption used in the Malkmus model derivation, emerges as  $B$  becomes small. With decreasing pressure, line core regions occupy an increasingly smaller fraction of the spectral interval  $[\nu_1, \nu_2]$ , and a greater fraction of the interval becomes characterized by Lorentz wing absorption, i.e.,  $k \propto S/\nu^2$ .

Transforming this spectral dependence to a frequency distribution, as in (2), yields  $f(k) \propto k^{-3/2}$ . *Arking and Grossman* [1972] observed a similar slope in their numerical frequency distributions for the  $15\text{-}\mu\text{m}$   $\text{CO}_2$  band, though they did not explicitly identify the slope as being due to Lorentz profile wing absorption.

The shape of the  $f(k)$  profile is invariant in  $S/k$ . Hence, changing  $S$  relative to a reference value  $S_0$  causes the probability density profile to be shifted horizontally along the  $k$  axis by the ratio  $S/S_0$ , and vertically by the factor  $S_0/S$  to maintain normalization of  $f(k)$ .

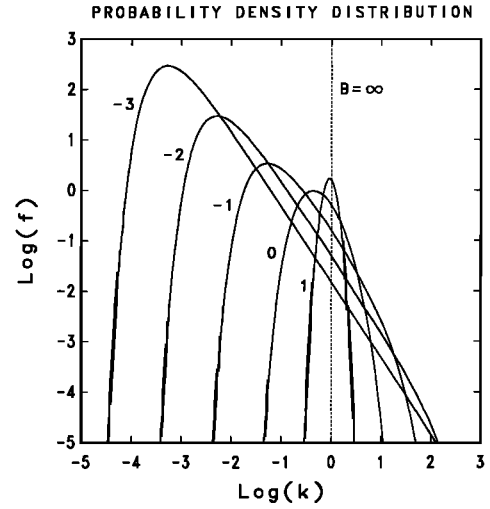


Fig. 5a

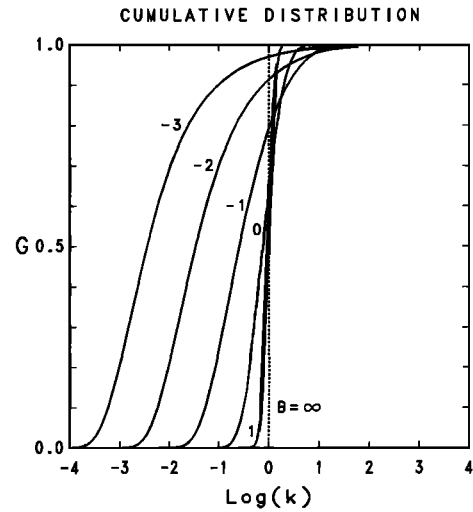


Fig. 5b

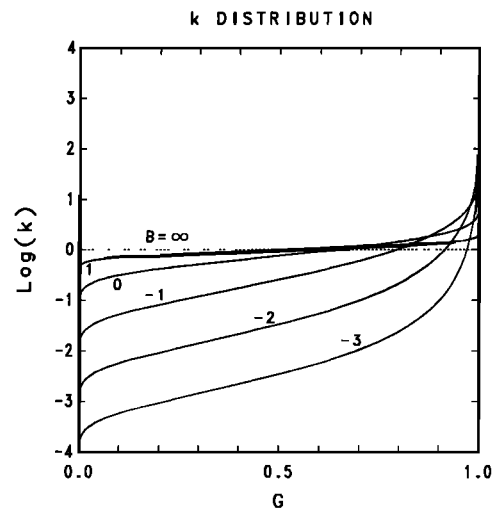


Fig. 5c

Fig. 5. (a) Malkmus model probability density distributions for fixed effective line strength,  $S = 1$ . The effective line half width parameter is varied from  $B = 10$  to  $B = 10^{-3}$ , with each curve identified by its  $\log B$  value. (b) Malkmus cumulative probability distributions corresponding to  $B$  and  $S$  parameters in Figure 5a. (c) Malkmus  $k$  distributions for  $B$  and  $S$  parameters plotted in Figure 5a.

### 3.2. The Cumulative Density Distribution

The Malkmus model density distribution  $f(k)$  can be integrated in closed form to yield the cumulative density distribution of absorption coefficient strengths

$$g(k) = \int_0^k f(k') dk'$$

This is given by

$$g(k) = 1/2[1 - \operatorname{erf}(a/\sqrt{k} - b\sqrt{k})] + 1/2[1 - \operatorname{erf}(a/\sqrt{k} + b\sqrt{k})]e^{\pi B} \quad (21)$$

where  $a = \frac{1}{2}(\pi BS)^{1/2}$ ,  $b = \frac{1}{2}(\pi B/S)^{1/2}$ , and where  $\operatorname{erf}(z)$  is the error function

$$\operatorname{erf}(z) = 2/\sqrt{\pi} \int_0^z e^{-t^2} dt$$

The cumulative density distribution displays the distribution of absorption coefficient strengths in monotonic order and represents the accumulated fraction of the spectral interval  $[\nu_1, \nu_2]$  for which absorption coefficient strengths are less than  $k$ . These  $g(k)$  profiles, shown in Figure 5b, are for the same set of Malkmus model parameters that define the  $f(k)$  distributions in Figure 5a. The cumulative probability distributions are an intermediate step in transforming the absorption spectra into monotonically ordered  $k$  distributions.

### 3.3. The $k$ Distribution

Taking the inverse of the cumulative density distribution in (21) yields the Malkmus model  $k$  distribution:

$$k(g) = g^{-1}(k) \quad (22)$$

Though not expressible in analytic form,  $k(g)$  can be obtained numerically, requiring 5–10 iterations to achieve 6-digit precision. The inflection point at  $k = k_{\max}$  given by (19) provides a convenient starting point for a Newton-Raphson type iteration. The resulting  $k$  distributions are shown in Figure 5c. The pseudo-absorption line characteristics are evident in the  $k$  distribution profiles and show the simulated pressure broadening changes that are effected through the  $B$  parameter.

The Malkmus model equivalents for the absorption coefficient frequency distribution, the cumulative frequency distribution, and the  $k$  distribution are shown by the dashed lines in Figures 1 and 2 for band model transmissions that have been least squares fitted to line-by-line calculations for the 1510–1520  $\text{cm}^{-1}$  section of the 6.3- $\mu\text{m}$  water vapor band and the 660–670  $\text{cm}^{-1}$  section of the 15- $\mu\text{m}$   $\text{CO}_2$  band, respectively. The close agreement between line-by-line and band model results for water vapor tends to verify the basic soundness of the  $k$  distribution approach. Even in the low-pressure case of the 660–670  $\text{cm}^{-1}$  section of the 15- $\mu\text{m}$   $\text{CO}_2$  band, adequate accuracy is obtained.

The nongray nature of the Malkmus transmission and its similarity to standard absorption line behavior is illustrated in Figure 6, where the differential of the cumulative transmission,  $T(g) = e^{-k(g)u}$ , is plotted. The results shown are for a spectral-mean optical depth of unity (i.e.,  $S = 1$ ;  $u = 1$ ) as

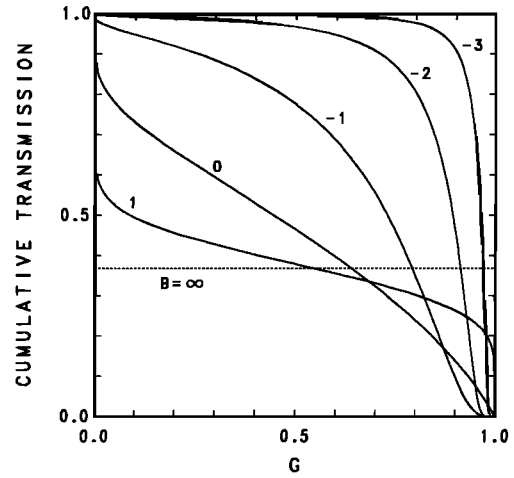


Fig. 6. Cumulative transmission for fixed mean line strength of  $S = 1$ . The effective line half width parameter is varied from  $B = 10$  to  $B = 10^{-3}$  with the absorber amount taken as unity. The dotted line depicts the limit for infinite pressure broadening ( $B \rightarrow \infty$ ). The total transmission  $T(u)$  is given by the area under each curve.

the effective half width parameter  $B$  is varied from  $10^{-3}$  to 10. The dotted line represents the limiting case of infinite pressure broadening, where the nongray absorption dependence is obliterated as  $k(g) \rightarrow S$ . (Here the differential cumulative transmission,  $T(g) = T(u)$ , is equal to the integrated transmission, or area under the curve in Figure 6). The increase in total transmission (with concentration of absorption in a narrow fraction of the cumulative density interval) as  $B$  decreases is characteristic of the change in nongray absorption that takes place with height in the atmosphere. Below we seek to “digitize,” or histogram, the cumulative transmission to facilitate accurate numerical representation of the changing nongray distribution with height.

### 3.4. The Cumulative Transmission Function

The cumulative transmission function defines the accumulated fractional transmission that is associated with absorption coefficients of strengths less than  $k$  within the spectral interval  $[\nu_1, \nu_2]$ . It allows  $k$  distributions to be digitized in histogram form without loss of transmission accuracy.

$$h(k) = \int_0^k f(k') e^{-k'u} dk' \quad (23)$$

For the Malkmus probability density distribution  $f(k)$  in (17), the cumulative transmission function exists in closed form:

$$h(k) = 1/2[1 - \operatorname{erf}(a/\sqrt{k} - c\sqrt{k})]T(u) + 1/2[1 - \operatorname{erf}(a/\sqrt{k} + c\sqrt{k})]T^{-1}(u)e^{\pi B} \quad (24)$$

where  $a = \frac{1}{2}(\pi BS)^{1/2}$ ,  $c = \frac{1}{2}(\pi B/S + 4u)^{1/2}$ , and  $T(u)$  is the Malkmus transmission given in (9).

The cumulative transmission function permits easy subdivision of the cumulative density coordinate range into arbitrary subintervals,  $\Delta g_i$ , while conserving transmission accuracy. The boundaries of these subintervals are set in  $k$  space using the inverse relationship in (22). The example in Figure 7 shows the digitized form of the  $k$  distribution for subinter-

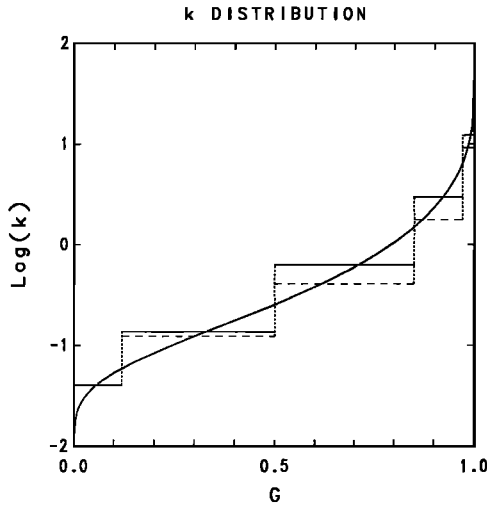


Fig. 7. Digitized  $k$  distribution. The solid curved line is the Malkmus  $k$  distribution for  $B = 0.1$  and  $S = 1$ . The solid histogram is the digitized  $k$  distribution in the limit of zero absorber amount as given by (28). The dashed histogram is the absorber weighted ( $u = 1$ ) digitization of the  $k$  distribution given by (26).

vals of  $\Delta g_i$  that have been set to provide approximately uniform (though coarse) resolution over the absorption coefficient range.

The mean absorption coefficients over the specified subintervals of  $\Delta g_i$  are defined as transmission-weighted averages:

$$e^{-\bar{k}_i u} = \frac{\int_{k_i}^{k_j} f(k) e^{-ku} dk}{\int_{k_i}^{k_j} f(k) dk} \quad (25)$$

or

$$\bar{k}_i = \frac{1}{u} \ln (\Delta g_i / \Delta h_i) \quad (26)$$

where  $\Delta g_i$  and  $\Delta h_i$  designate the cumulative density and cumulative transmission subintervals bounded by  $k_i$  and  $k_j$  in (25).

Since the mean absorption coefficients defined in (26) are weighted averages for a specified absorber amount, the resulting histogram of absorption coefficients is necessarily absorber dependent. Because of this, the transmission computed by

$$T(u) = \sum_i^N e^{-\bar{k}_i u} \Delta g_i \quad (27)$$

remains equal to the Malkmus transmission  $T(u)$  given by (9), regardless of the number of subintervals that are used in the summation over the cumulative transmission contributions from the individual subintervals  $\Delta g_i$ . The above relations permit arbitrary digitization of the Malkmus transmission. This practically eliminates the need for exponential sum fitting of  $k$  distributions such as those described by Lacis and Hansen [1974] and Wiscombe and Evans [1977].

As defined above, the histogrammed  $k$  distribution "con-

serves" the band model transmission; the number and width of the subintervals can be selected to optimize computing time and the treatment of nongray absorption effects. The absorption coefficient dependence on absorber amount is automatically set within each  $k$  distribution interval and may be thought of as a form of multiparameter scaling. Obviously, with a larger number of subintervals in the summation, nongray effects are treated more accurately and the pathlength dependence of the absorption coefficients is reduced, but there is an increase in computing time.

For comparison, in the limit as  $u \rightarrow 0$ , the mean absorption coefficients within the  $\Delta g_i$  subintervals are given by

$$\bar{k}_i^0 = S \frac{\text{erf}(a/\sqrt{k} - b\sqrt{k})|_{k_i}^{k_j} - e^{\pi B} \text{erf}(a/\sqrt{k} + b\sqrt{k})|_{k_i}^{k_j}}{\text{erf}(a/\sqrt{k} - b\sqrt{k})|_{k_i}^{k_j} + e^{\pi B} \text{erf}(a/\sqrt{k} + b\sqrt{k})|_{k_i}^{k_j}} \quad (28)$$

where  $\bar{k}_i^0$  designates pathlength independent absorption coefficients within the  $i$ th interval bounded by absorption coefficient values  $k_i$  and  $k_j$ , respectively. In (28) the mean absorption coefficients are obtained by differencing the respective error functions evaluated for  $k_i$  and  $k_j$ ; all of the other parameters have their previous meanings.

In Figure 7 the histogrammed  $k$  distributions for the pathlength dependent (dashed line) and the pathlength independent (solid lines) cases, defined by (26) and (28), respectively, are compared for a coarse subdivision of the cumulative density coordinate  $g$ , representative of the resolution used in GCM applications. The illustrative example, computed for an absorber amount of  $u = 10$ , with  $B = 10^{-2}$  and  $S = 1$ , yields a transmission of  $T(u) = 0.58$  and shows substantial pathlength dependence of the histogrammed absorption coefficients, particularly for the stronger absorption coefficient values. Note that the absorber unweighted coefficients (solid line), that are valid in the limit as  $u \rightarrow 0$ , would overestimate the absorption for the case of coarse resolution illustrated in Figure 7, while the transmission computed with the pathlength dependent absorption coefficients (dashed line) given by (26) is precisely equal to  $T(u)$ .

For computational efficiency, the cumulative density range is divided into subintervals that are unequal in width. The unequal spacing of intervals in  $\Delta g$  is selected to provide approximately equal ratios in absorption coefficient strength; this provides a more uniform distribution of absorption coefficient strengths when modeling nongray absorption. Though transmission is conserved over a homogeneous path (with no scattering) for any number of  $k$  intervals, nongray effects become evident in the case of multiple scattering and for vertical inhomogeneity. Then for a given number of  $k$  intervals, optimum accuracy is obtained when the cumulative density intervals are more closely spaced near  $g = 0$ , and the strong absorption end near  $g = 1$ .

### 3.5. Band Model Limitations

Despite its versatility over a wide range of atmospheric conditions, there are several notable examples where the Malkmus model accuracy is deficient. First, the  $k$  distributions for single Lorentz or Doppler lines are poorly represented by the Malkmus model. The practical consequence of this is minimal, requiring only that the spectral intervals be

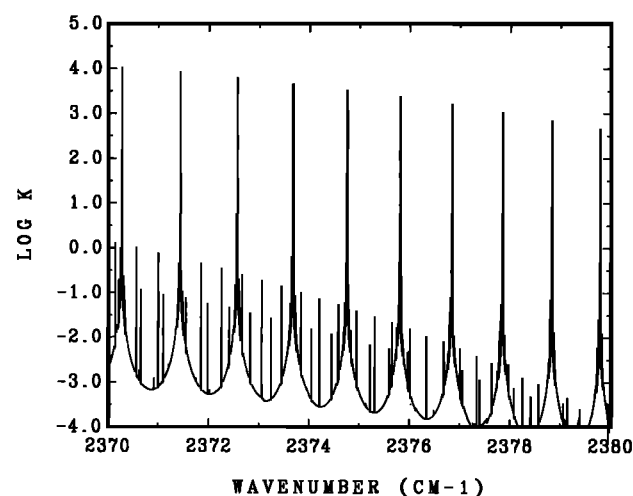


Fig. 8a

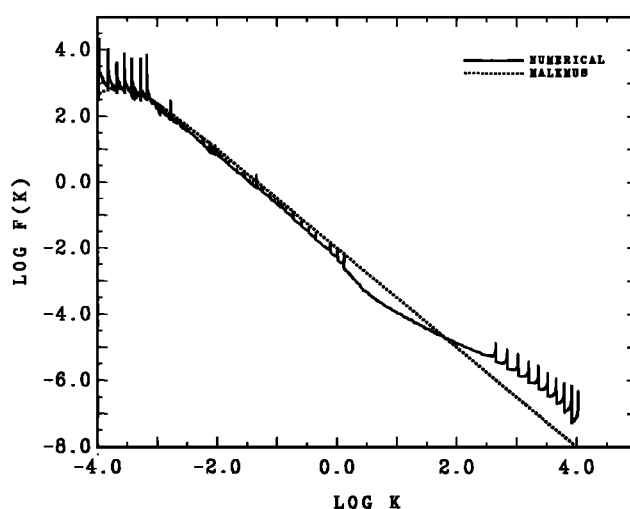


Fig. 8b

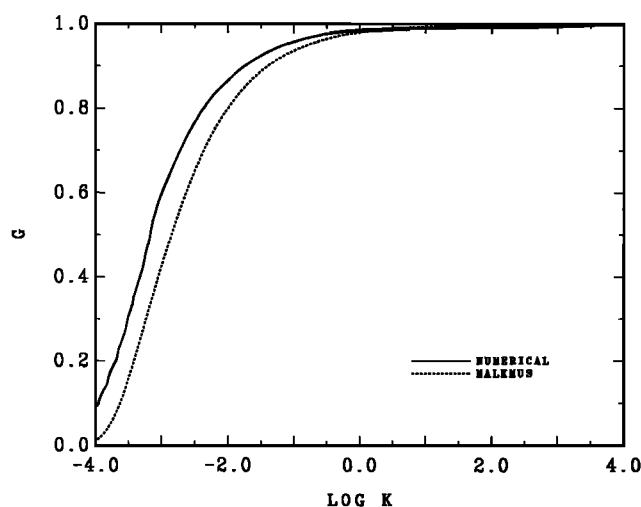


Fig. 8c

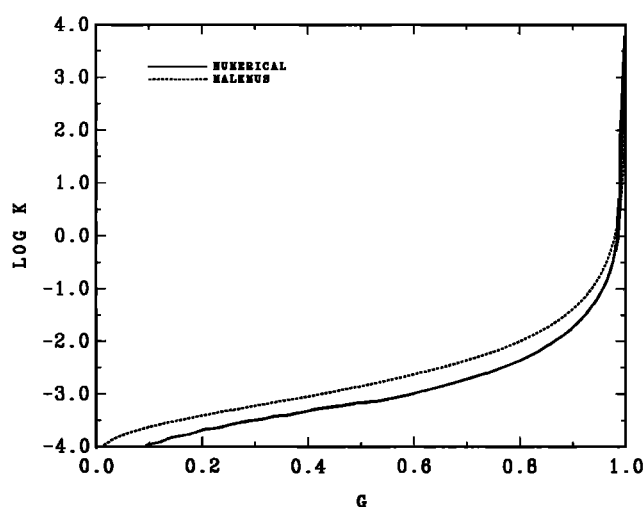


Fig. 8d

Fig. 8. Absorption coefficient spectrum for the 2370–2380  $\text{cm}^{-1}$  portion of the 4.7- $\mu\text{m}$   $\text{CO}_2$  band. (a) Doppler limit line-by-line absorption coefficients for a pressure of 0.1 mbar and temperature of 220 K. (b) Absorption coefficient frequency distribution. (c) Cumulative frequency distributions and corresponding (d)  $k$  distribution. The dotted lines are the Malkmus band model equivalents.

broad enough to contain several dozen lines. For typical spectral resolution for narrow-band applications of 5–50  $\text{cm}^{-1}$ , this poses no problem. Moreover, while the shape of the Malkmus model  $k$  distribution is very different from that of an isolated Lorentz line, the situation is not all that bleak because we can least squares fit the band model parameters to closely match the isolated line transmission over some desired absorber range. This way, transmission (or absorption) accuracy of order 1–2% can still be achieved for absorber amounts that range over a factor of 30.

In the atmosphere, a difficult case arises when the pressure becomes so low that the line profiles have the Doppler shape and when the strong lines present become appreciably saturated. In this case, the pseudoline  $k(g)$   $k$  distribution of the sample spectrum has a slope that is too steep for the Malkmus model  $k(g)$  to provide an adequate fit, i.e., the Malkmus model  $k$  distribution is too gray to fit the Doppler line shape. This difficulty can be illustrated further by

considering the slope of the  $k$  distribution function  $f(k)$  in the limit of large  $k$ . For the Malkmus model this limiting slope is

$$\frac{d \ln f(k)}{d \ln k} = -\frac{3}{2} - \frac{\pi B}{4S} k \quad (29)$$

For a Doppler line the minimum slope is

$$\frac{d \ln f(k)}{d \ln k} = -1 \quad (30)$$

The best that can be accomplished in attempting a fit to line-by-line absorption in the case of a Doppler line spectrum is to have the two transmission curves intersect at some desired point. This is illustrated in Figure 8 for a selected section of the  $\text{CO}_2$  spectrum in the center of the very strong 4.3- $\mu\text{m}$  band. A least squares fit of the Malkmus band model parameters was made to line-by-line transmissions calcu-

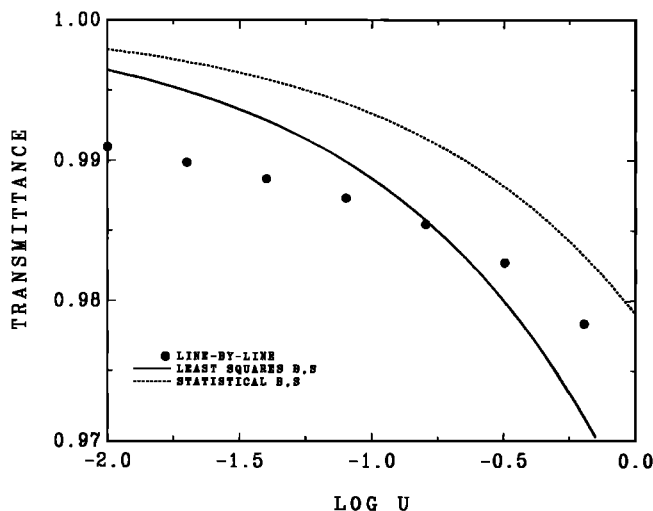


Fig. 9. Least squares fit of Malkmus band model parameters to line-by-line transmission for spectrum defined in Figure 8. Symbols used are defined as in Figure 3.

lated for absorber amounts ranging from 0.02 to 0.64 cm (STP) characteristic of a 2-km-thick atmospheric layer at the 0.1-mbar level. The spectral range covered (Figure 8a) is  $2370\text{--}2380\text{ cm}^{-1}$ ; the temperature is 220 K. The incompatibility of the slopes of the frequency distributions within the absorber range of the desired fit is clearly evident in Figure 8b. This difference is further illustrated in Figures 8c and 8d for the corresponding cumulative frequency and  $k$  distributions, respectively.

Figure 9 shows the resulting poor fit of the Malkmus model transmission (solid line) to line-by-line computations (solid circles). This again illustrates the point that least squares fitting can produce agreement between the line-by-line and band model transmissions for a specified absorber amount, even in the Doppler regime. But, aside from the crossover point, large errors in the absorber dependence of transmission (and absorption) persist because of the incompatibility of slopes of the Malkmus model and Doppler regime  $k$  distributions. For completeness, the dashed line in Figure 9 shows the even more dismal fit to the line-by-line transmission using statistical band model parameters.

#### 4. ABSORPTION IN VERTICALLY INHOMOGENEOUS MEDIA

In previous sections we described the basic approach for converting line-by-line transmissions over homogeneous paths into band model  $k$  distributions which can reproduce the line-by-line results without significant loss of accuracy. We now extend these techniques to model nongray gaseous absorption in a realistic atmosphere where pressure broadening and the atmospheric temperature gradient produce a vertically inhomogeneous absorber path. First, we present the rationale for modeling the effects of atmospheric pressure broadening by means of vertically correlated  $k$  distributions. Then we compare these correlated  $k$  distribution results to line-by-line radiative heating and cooling rates for the principal atmospheric gases.

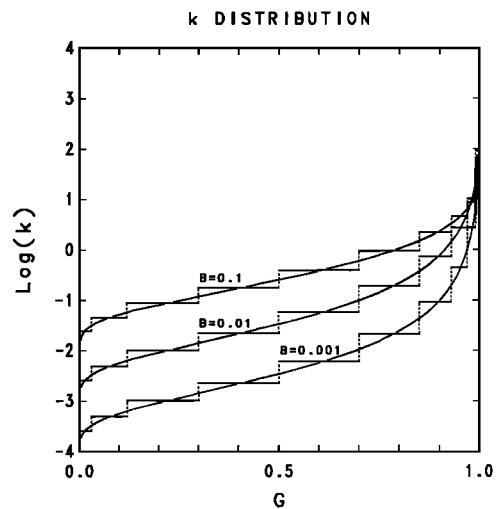


Fig. 10. Vertically correlated  $k$  distributions. The vertical correlation of Malkmus model  $k$  distributions at selected pressure levels of the atmosphere is established by maintaining the same histogramming intervals at all levels of the atmosphere. The three  $k$  distributions and corresponding histograms are for fixed  $S$  ( $S = 1$ ), with  $B$  values of 0.001, 0.01, and 0.1, respectively.

##### 4.1. Vertical Correlation of $k$ Distributions

The rationale of applying  $k$  distributions derived for homogeneous absorber paths to model pressure broadening and nongray gaseous absorption in vertically inhomogeneous atmospheres makes use of the pseudo-absorption line characteristics of  $k$  distributions. The basic premise is that, for a given spectral interval  $[\nu_1, \nu_2]$ ,  $k$  distributions at all altitudes are simply correlated in frequency space. This correlation of absorption coefficients at different heights in the atmosphere is apparent in the case of a single absorption line, where it is easy to verify the one-to-one correspondence that exists between the monotonically ordered rank of absorption coefficient strengths and the wavelength scale relative to the line center. This correspondence, as long as the line center remains fixed, is rigorously maintained at all levels of the atmosphere with the strongest absorption always occurring at the line-center frequency at all pressure levels. Similarly, the weakest absorption at all altitudes occurs at frequencies corresponding to the extreme line wings. For single lines, and in the case of a regular Elsasser band model, the cumulative probability density scale  $g$  of absorption coefficient strengths maps uniquely into the wavelength scale at each level of the atmosphere, thus assuring complete vertical correlation at all values of  $g$ .

The Malkmus band model  $k$  distribution profiles, computed for different atmospheric pressures, exhibit characteristics that resemble the pressure-broadening behavior of individual absorption lines. For example, the strongest absorption in the spectral interval  $[\nu_1, \nu_2]$ , which originates from the line-center region of the strongest line in the interval, will occur at the same frequency (and at the same value of the cumulative density  $g$  at all altitudes. We assume that a similar correspondence will hold with sufficient accuracy for intermediate values of absorption coefficient strength down to the weakest absorption in the interval. Thus absorption coefficients of a given relative strength may originate from different noncontiguous wavelength regions within the spectral interval  $[\nu_1, \nu_2]$ ; but the same set of

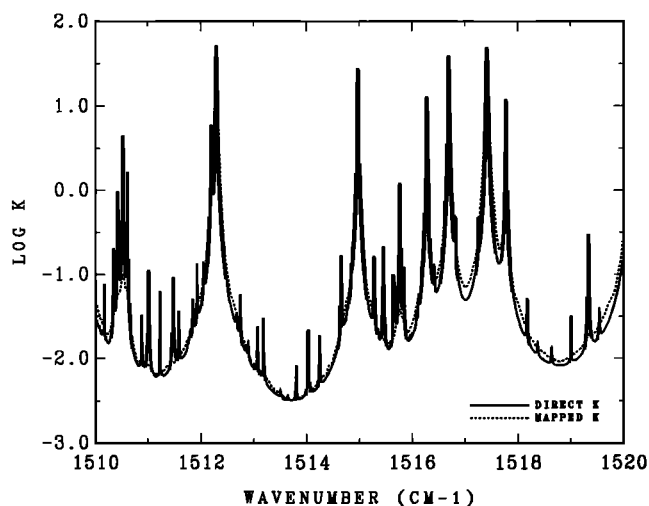


Fig. 11a

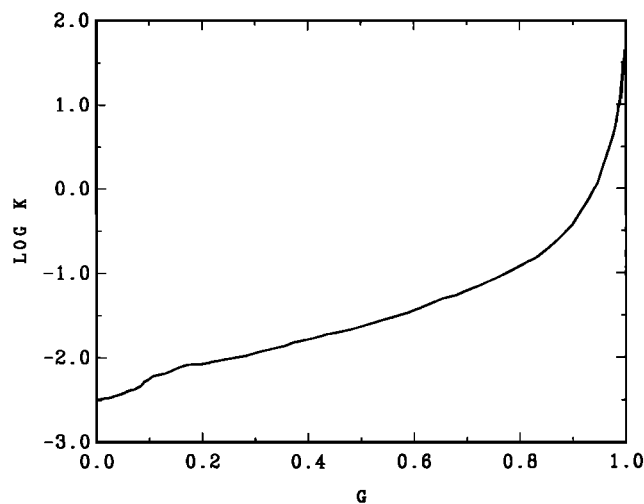


Fig. 11b

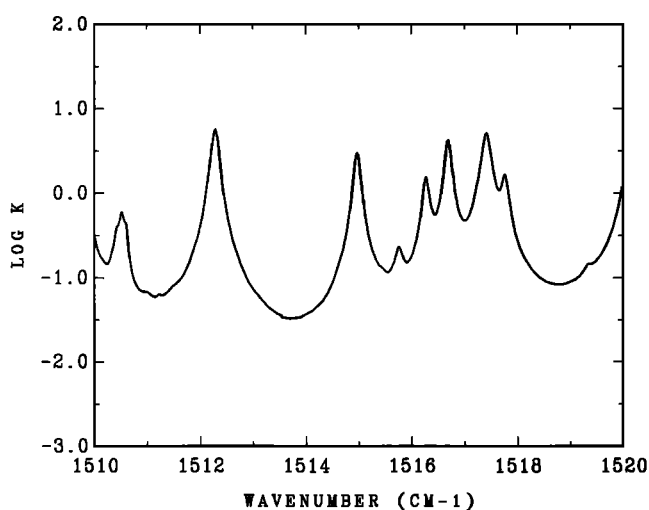


Fig. 11c

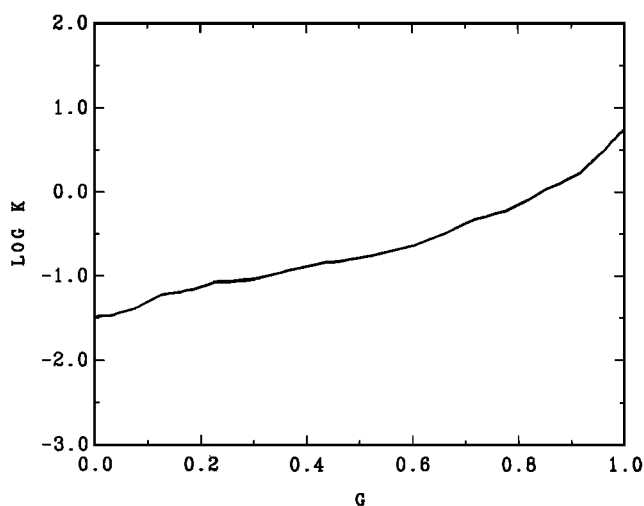


Fig. 11d

Fig. 11. Spectral correlation for transmission across a pressure inhomogeneity of 0.1 to 1.0 bars. (a) Results for the 1510–1520  $\text{cm}^{-1}$  portion of the 6.3- $\mu\text{m}$  water vapor band at 0.1-bar pressure and (c) 1.0 bar, respectively. (b and d) Numerical  $k$  distributions of respective absorption spectra in Figures 11a and 11c. The dashed line in Figure 11a is the result of mapping the absorption spectrum in Figure 11c via the  $k$  distributions in Figures 11d and 11b.

noncontiguous wavelengths will comprise absorption coefficients of the same relative strength in corresponding  $\Delta g$  subintervals from  $k$  distributions at different atmospheric heights. To maintain this vertical correlation of band model  $k$  distributions at different atmospheric pressure levels requires fixed subdivisions of  $\Delta g$ , i.e., for a given spectral interval  $[\nu_1, \nu_2]$ , the same set of  $\Delta g$  subintervals is to be used for all atmospheric layers as shown in Figure 10.

While there is reason to believe that the assumed vertical correlation is robust for the strongest and weakest absorption coefficients in the spectral interval  $[\nu_1, \nu_2]$ , it is also easy to see that strict correlation is not likely to be maintained over the entire range of absorption coefficient strengths. For example, randomly overlapping absorption lines of different strengths and large-scale shifts in line strength distribution within hot band regions can produce spectrally uncorrelated changes in  $k$  distribution. The precise degree of correlation between  $k$  distributions at different pressures and tempera-

tures and how this correlation affects transmission accuracy for arbitrary spectral intervals are difficult to describe a priori. Below, we illustrate the nature of this problem by considering two extreme examples.

In Figure 11 we examine the spectral correlation for transmission through two contiguous atmospheric slabs separated by a large pressure difference of 0.1–1.0 bars. (This is a far more extreme case than normally encountered in the atmosphere.) Absorption coefficient spectra for water vapor in the 1510–1520  $\text{cm}^{-1}$  wavelength interval are shown in Figures 11a and 11c for pressures of 0.1 and 1.0 bars, respectively. Figures 11b and 11d show the  $k$  distributions corresponding to these spectra. The dotted line in Figure 11a is obtained by mapping the absorption coefficient spectrum in Figure 11c to 11a via their respective  $k$  distributions in Figures 11d and 11b. This is done by taking the spectral subintervals in Figure 11c that have the same given value of  $k$ ; these subintervals constitute a particular value of  $g$  in the

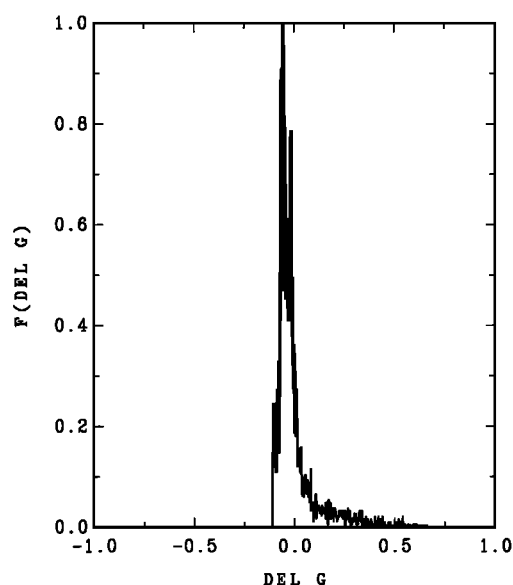


Fig. 12a

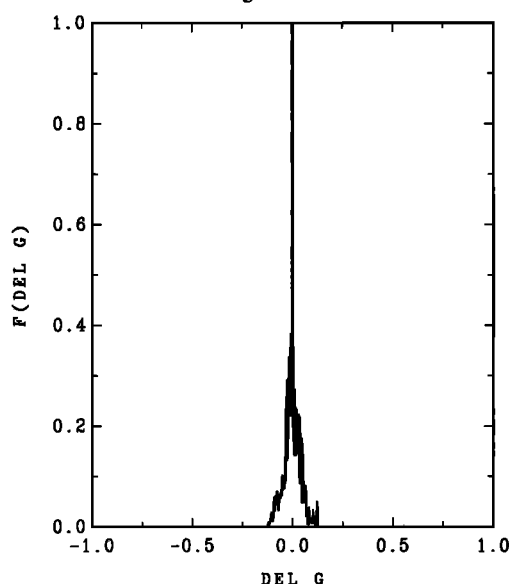


Fig. 12b

Fig. 12. Frequency distribution of correlation errors due to pressure and temperature inhomogeneities for water vapor in the 1510–1520  $\text{cm}^{-1}$  wavelength interval. (a) Distribution of correlation errors for pressure difference inhomogeneity between two slabs at 0.1- and 1.0-bar pressures at a temperature of 296 K, and (b) temperature difference inhomogeneity of 250 to 296 K at 1.0-bar pressure. The abscissa depicts the fractional error between  $g(k)$  values at identical frequency points in the top and bottom layer spectra. The ordinate is proportional to the number of frequency points with correlation errors equal to  $\Delta g$ .

high pressure  $k$  distribution in Figure 11d. The same  $g$  value in the low-pressure  $k$  distribution is then used to map the above spectral subintervals. Though substantial differences are apparent at specific wavelengths, it can be seen that there is error compensation at nearby wavelengths.

Figure 12a shows the (unnormalized) distribution of correlation errors for the case of pressure difference inhomogeneity. The abscissa depicts the error, defined as the difference in the values of  $g(k)$  at the same frequency point in the spectra of the two layers, while the ordinate is proportional

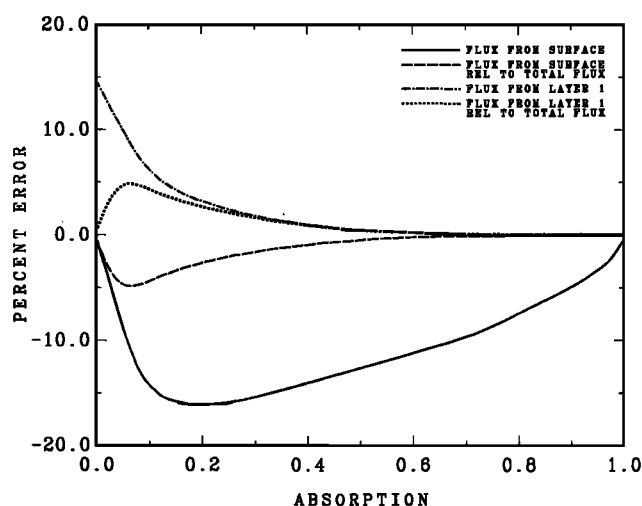


Fig. 13a

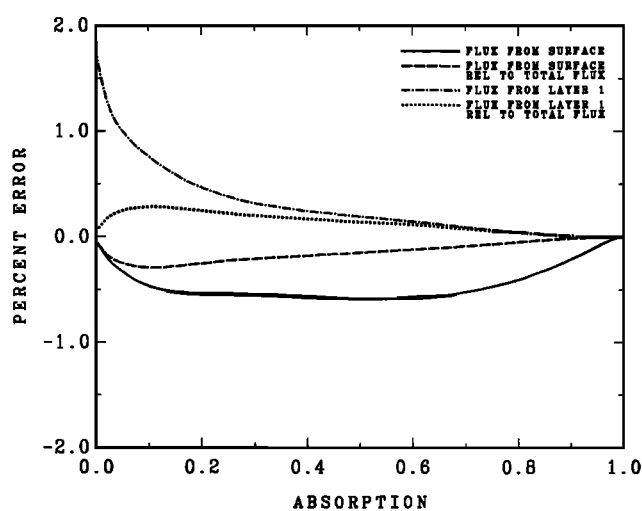


Fig. 13b

Fig. 13. Emission and absorption errors caused by errors in spectral correlation. (a) Results for the pressure difference inhomogeneity in the water vapor spectra shown in Figure 11. (b) Results for temperature difference inhomogeneity for the water vapor spectra shown in Figure 14. The solid lines depict the percent errors in absorption (within the top slab) of the flux emitted by the surface, while the broken lines represent the errors in absorption weighted by the contribution of the surface to the total absorbed flux. The dashed and dotted lines depict analogous quantities for the flux emitted by the bottom slab. The errors are plotted as a function of the layer absorptance, which is kept equal and varied simultaneously in the two layers.

to the number of frequency points where the correlation error has the abscissa error value. The largest errors tend to occur in situations where the peaks of the low-pressure spectrum are higher than the corresponding peaks of the  $k$  mapped spectrum, except in the case of the highest peak. Despite the extreme pressure difference between the two test layers, the frequency correlation remains quite good.

To examine the effect of the degree of spectral correlation on the radiative fluxes, upward fluxes are calculated for a wide range of absorber amounts using both line-by-line and correlated  $k$  distribution calculations for water vapor in the 1510–1520  $\text{cm}^{-1}$  wavelength interval. The rather extreme



configuration used to illustrate the effect consists of two contiguous low- and high-pressure layers overlying a surface that produces a spectrally flat emission. To isolate the correlation effect and to minimize extraneous factors, both layers and the emitting surface are taken to be isothermal; thus both methods will give the same net outgoing flux at each layer boundary independent of absorption coefficient differences. However, there will be compensating errors in the correlated  $k$  distribution fluxes (relative to the line-by-line fluxes) from the individual layers that combine to yield the net flux. These errors in the top layer fluxes are plotted in Figure 13a as a function of absorption within that layer.

The solid line in Figure 13a in the percent error in the absorption by the top slab of the flux originating from the surface. The dashed line is the corresponding relative error, i.e., the error in the absorption of the flux originating from the surface relative to the absorbed flux originating from both the surface and the bottom layer. Similarly, the broken line is the percent error in the absorption by the top slab of the flux originating from the bottom layer, while the dotted line is the relative error, i.e., the error in the absorption of the flux from the bottom layer relative to the total absorbed flux. For the isothermal case selected, the relative errors in absorbed fluxes must sum to zero. Note that although the percent error in the absorbed surface flux is quite large, the relative error quickly approaches zero with increasing absorber amount due to the increasing optical depth of the intervening bottom layer. Similarly, for very small absorber amounts, the large percentage error in the absorption of the flux from the bottom layer is negated by the dominance of the surface.

Considering the large difference in pressure between the layers, the errors are gratifyingly small. Differences in transmission across the two slabs between line-by-line and  $k$  distribution calculations are very small (less than 1%) for a wide range of absorber amounts and are thus less diagnostic of correlation differences.

In Figure 14 we examine the spectral correlation for water vapor in the 1510–1520  $\text{cm}^{-1}$  wavelength interval at a fixed pressure of 1.0 bar, but with a temperature inhomogeneity of 46 K (again, a more severe case than would be normally encountered in the atmosphere). The differences between these spectra are due primarily to changes in line strength dependence on temperature and to a lesser extent to the  $(T_0/T)^n$  pressure broadening caused by the temperature differential. As in Figure 13a, the dotted line in Figure 14a is obtained by mapping spectral subintervals at corresponding  $g$  values from the 296 K spectrum in Figure 14c via their respective  $k$  distributions to the 250 K spectrum in Figure 14a. Again, substantial differences occur at some wavelengths with compensating differences at nearby wavelengths.

A plot of the unnormalized distribution of correlation errors for the temperature difference inhomogeneity is shown in Figure 12b. The correlation distribution is defined in the same way as for the pressure difference case. The sharper distribution of correlation errors in Figure 12b is indicative of the closer correspondence between the reference spectrum (solid line) and the mapped spectrum (dashed line) in Figure 14a and shows the temperature difference inhomogeneity to be less extreme than the pressure difference inhomogeneity. Figure 13b shows the error contribution to the net flux absorbed in the top layer of the two-slab

atmosphere analogous to those shown in Figure 13a. Again, because of the stronger spectral correlation in Figure 14, the flux errors are significantly smaller than those for the pressure inhomogeneity in Figure 13a (note the change in scale).

In modeling the real atmosphere, the pressure and temperature differences that are encountered between radiatively interacting layers are typically much smaller than those used in the illustrations above. In these more realistic cases, the mapping of spectral subintervals at corresponding values of  $g$ , as in Figures 13 and 14, would produce differences so small as to be masked by the width of a line. The radiative exchanges that take place between a given atmospheric layer and more distant layers, including the ground and the boundary with space, generally take place within the relatively transparent regions of the spectrum where the correlated  $k$  distribution results would be accurate due to the relative insensitivity to spectral detail in the optically thin regime. In the case of moderate to strong absorption, most of the atmospheric thermal radiation is emitted and re-absorbed between neighboring layers of the atmosphere (involving only small pressure and temperature differences between interacting layers) with typically only a small fraction escaping directly to space. We can therefore expect the correlated  $k$  distribution method to yield accurate heating and cooling rates despite the large vertical inhomogeneity of the atmosphere. This contention, nevertheless, is substantiated best by making detailed comparisons of radiative cooling rates obtained with the  $k$  distribution approach with those obtained from line-by-line calculations for realistic absorber, temperature, and pressure profiles in a vertically inhomogeneous multilayered atmosphere. These comparisons are made in section 5.

In passing, it may be worth noting that the so-called cooling-to-space approximation, whereby the net radiative balance due to interactions between atmospheric layers is set to zero, can yield fairly accurate cooling rates in some circumstances but fail badly in other cases [e.g., *Fels and Schwartzkopf*, 1975]. We performed several test calculations using this method with the column transmissions above each layer computed using  $k$  distributions. While the cooling-to-space approximation yields substantial savings in computing time, in nearly all cases the errors were much larger compared to the correlated  $k$  distribution approach.

#### 4.2. Overlapping Absorption

Overlapping absorption is a common problem in radiative transfer modeling of the atmosphere. The common assumption that is generally made to account for overlapping absorption is that the absorption line positions of one gas relative to the other are randomly distributed. In this case, transmission by the combined gases is the scalar product of the two individual transmissions, i.e.,  $T(u_a, u_b) = T(u_a) \times T(u_b)$ . However, this formulation loses validity in a multilayered atmosphere because there is strong correlation of the overlapping spectra between neighboring atmospheric layers; hence the successive multiplications of the transmission product between different atmospheric layers destroys the nongray information in the overlapping spectra.

To evaluate the nongray product of the individual transmissions in terms of the  $k$  distribution formulation, the combined transmission for overlapping gases is given by the double sum

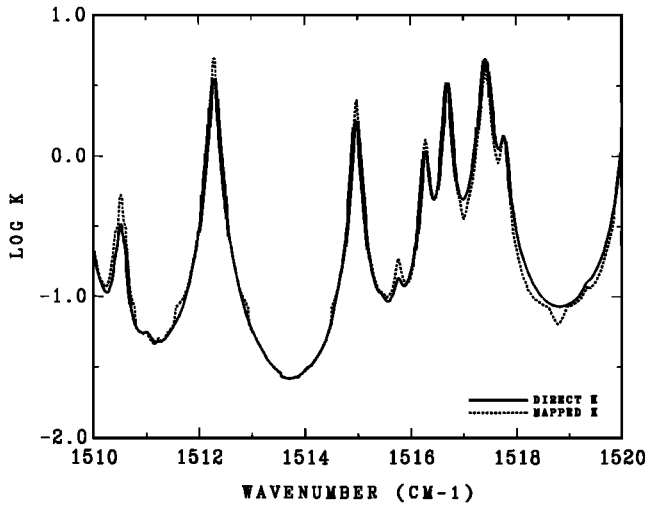


Fig. 14a

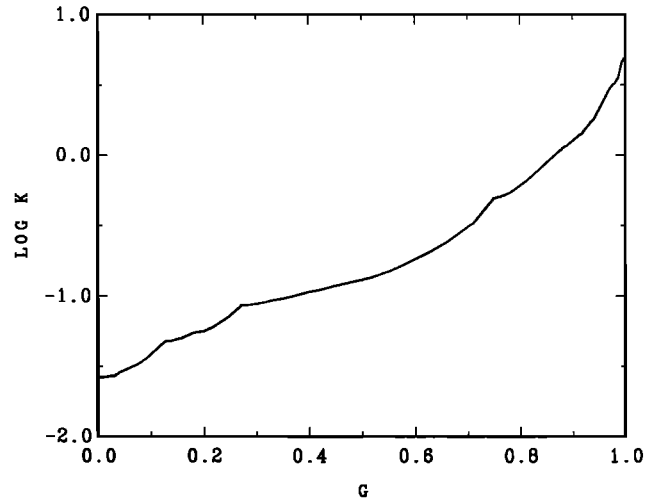


Fig. 14b

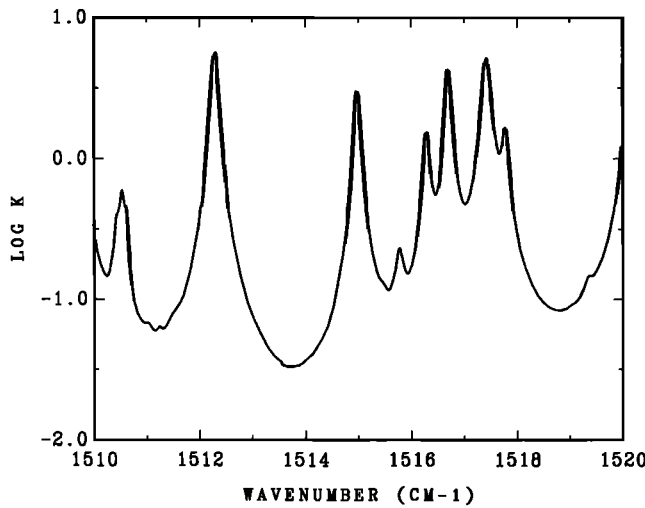


Fig. 14c

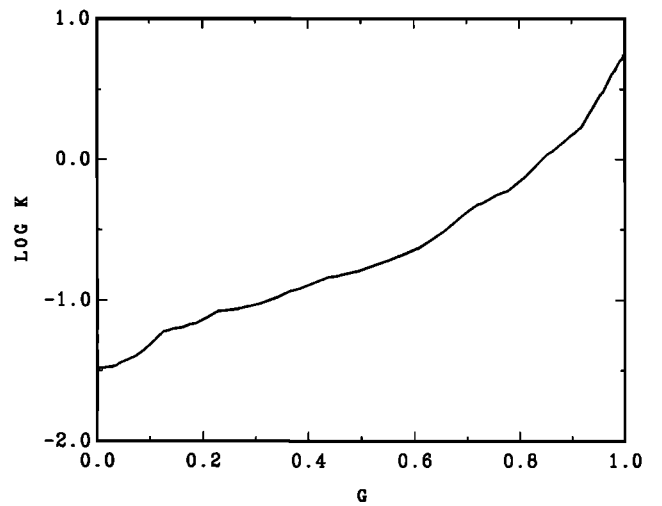


Fig. 14d

Fig. 14. Spectral correlation for transmission across temperature difference inhomogeneity between two slabs at temperatures of 250 and 296 K. (a) Absorption spectrum at 1-bar pressure and 250 K and (c) 296 K. The dashed line in Figure 14a is the mapped spectrum from Figure 14c via the respective  $k$  distributions in Figures 14d and 14b, as in Figure 11.

$$T(u_a, u_b) = \sum_i^N \sum_j^N e^{-(k_i u_a + k_j u_b)} \Delta g_i \Delta g_j \quad (31)$$

where  $u_a$  and  $u_b$  are the absorber amounts of the two overlapping gases. Again, in order to retain the nongray information within the  $k$  distributions, computations are to be made over the full vertical extent of the atmosphere for each individual (i.e., pseudomonochromatic)  $k$  distribution component before being summed over  $N$  to obtain the transmitted fluxes. Since the double sum increases the computing time by a factor of  $N$  for each overlapping gas, it is expensive in computer time. Instead of calculating the entire vertical atmosphere with multiple scattering computations  $N^2$  times, we can minimize this added burden by first computing the  $N^2$  transmission terms according to (31), ranking them in monotonic order, and then reblocking these

$N^2$  transmissions back into the original number of  $N$   $k$  distribution intervals. Computations then proceed with the original number of  $N$   $k$  distribution intervals. Generally, the time consumed in sorting and reblocking the  $N^2$   $k$  intervals is small compared to performing  $N$  multiple scattering computations, hence saving in computing time. This rather clumsy approach for treating overlapping absorption has been in use in most of our 1-D and 3-D climate modeling applications.

Overlapping absorption by several different gases can also be evaluated more directly in terms of the band model parameters by combining the  $B$  and  $S$  parameters for each gas in a manner that is consistent with the band model assumption of uncorrelated randomly overlapping absorption lines. Consider, for example, two overlapping gases that are characterized by band model parameters  $B_a$ ,  $S_a$ , and absorber amount  $u_a$ , and  $B_b$ ,  $S_b$ , and  $u_b$ , respectively. The

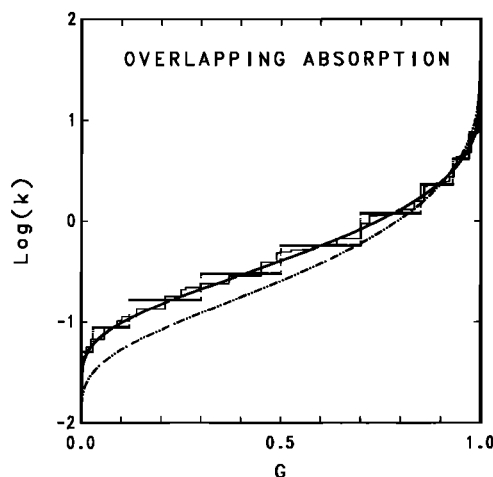


Fig. 15. Combining  $k$  distributions for the case of uncorrelated overlapping absorption. The broken line is the individual Malkmus  $k$  distribution, given by (22), for each of the two overlapping gases. The smooth solid curve is the overlapping  $k$  distribution obtained analytically using (32) and (33). The high-resolution histogram is the result of cross multiplying the  $k$  distributions of the two overlapping gases according to (31). The coarser histogram is the result of numerically reblocking to the original resolution. Transmissions computed with the histogrammed  $k$  distributions and the solid line  $k$  distribution are practically identical.

statistical parameter definitions in (10)–(12) imply that the  $B$  and  $S$  parameters for the two overlapping gases combine as follows:

$$S = S_a(u_a/u) + S_b(u_b/u) \quad (32)$$

$$(BS)^{1/2} = (B_a S_a u_a/u)^{1/2} + (B_b S_b u_b/u)^{1/2} \quad (33)$$

where  $u$  is the combined absorber amount,  $u = u_a + u_b$ . A similar procedure can be used to evaluate overlapping absorption for any number of gases.

The half-width relationship expressed in (33) implies a fit to the strong line limit for both gases. Thus, if the absorption by the overlapping gases is comparable with similar degree of saturation, their half width parameters can be combined as in (33). However, in the extreme situation where one of the gases is strongly absorbing and the other contributes only very weak absorption in the weak line limit, the square root dependence in (33) can greatly exaggerate this overlapping contribution and overestimate the value of the combined  $B$  parameter by an order of magnitude. This situation is found to occur in the Doppler regime of the  $15\text{-}\mu\text{m}$   $\text{CO}_2$  band, where the very weak  $\text{O}_3$  bands contribute the overlapping absorption. The remedy, which gives good results in these cases, is to add the effective Malkmus optical depths of the two gases calculated with (15), then use (16) to determine  $B$ . The  $S$  parameters, which add linearly, are not adversely affected by the absorber mismatch.

The equivalence between the redefinition of band model parameters according to (32) and (33), and the nongray product approach of cross multiplying the absorber-weighted  $k$  distributions of the overlapping gases according to (31) is demonstrated in Figure 15. In the example shown, the two gases are taken to have equal  $B$  and  $S$  parameters and equal absorber amounts. In terms of the statistical parameters,  $s$  and  $b$  remain unchanged, but the mean line spacing parameter  $d$  is reduced by half. Thus both  $B$  and  $S$

increase by a factor of 2, and the resulting band model transmission is equal to the product of the two individual transmissions.

The formalism for computing nongray transmission for overlapping absorption may appear well defined in cases where the overlapping spectra are uncorrelated. Nevertheless, it really requires line-by-line verification for each individual case to be sure that the overlapping absorption is indeed uncorrelated. An important example of overlapping absorption in the terrestrial atmosphere is the 7- to  $8\text{-}\mu\text{m}$  region, where the trace gases  $\text{CH}_4$  and  $\text{N}_2\text{O}$  overlap. Line-by-line radiative cooling rates for  $\text{CH}_4$  and  $\text{N}_2\text{O}$  are compared with correlated  $k$  distribution results in section 5.4, both for the individual gases and for the combined overlapping absorption case.

## 5. RADIATIVE COOLING RATES

Radiative cooling rates require modeling of both the magnitude and gradient of gaseous absorption and thermal emission over a wide range of pressures and absorber amounts. This poses a more rigorous test for the correlated  $k$  distribution than is provided by net flux comparisons at the top and bottom of the atmosphere. In this section, we compare radiative heating and cooling rates computed with the correlated  $k$  distribution method against line-by-line calculations for the principal atmospheric absorbing gases. The very different vertical distributions of atmospheric water vapor,  $\text{CO}_2$ , and ozone provide additional complexity to test the correlated  $k$  distribution method.

The numerical procedure for computing the radiative cooling rates is described in Appendix A, with additional details including tables of the line-by-line computed fluxes and radiative cooling rates given in Appendix B. Basically, we use the standard McClatchey mid-latitude summer pressure-temperature profile to define the atmosphere structure with 1-km resolution from the ground to 30 km, and 2-km resolution above 30 km. Our calculations assume local thermodynamic equilibrium throughout the atmosphere. While this results in diminished accuracy for the cooling rates above  $\sim 70$  km, where non-LTE effects become important [e.g., Kuhn and London, 1969], it does not degrade the line-by-line versus correlated  $k$  distribution comparisons.

To resolve the sharply peaked  $k$  distributions in the stratosphere, we used 36 intervals for the  $k$  distribution. (For most atmospheric applications, 10  $k$  intervals are generally sufficient.) The spectral width of the  $k$  distributions was taken to be  $10\text{ cm}^{-1}$ , although test examples using  $50\text{ cm}^{-1}$  resolution gave essentially identical results. The temperature gradient was specified to be linear (in Planck emission) within individual atmospheric layers to eliminate bias errors due to temperature gradient digitization. The computed radiances were integrated over emission angle using a five-point Gaussian quadrature to reduce flux errors from angle integration to a negligible proportion (see Figure A3). The resulting upwelling and downwelling fluxes were then differenced to obtain the radiative cooling rates.

In the following, we present radiative cooling rates for  $\text{H}_2\text{O}$ ,  $\text{CO}_2$ ,  $\text{O}_3$ , including an example of overlapping absorption illustrated for the case of  $\text{CH}_4$  and  $\text{N}_2\text{O}$ . The results are computed line-by-line and compared with the Malkmus model based correlated  $k$  distribution approach. We emphasize again that the correlated  $k$  distribution results presented

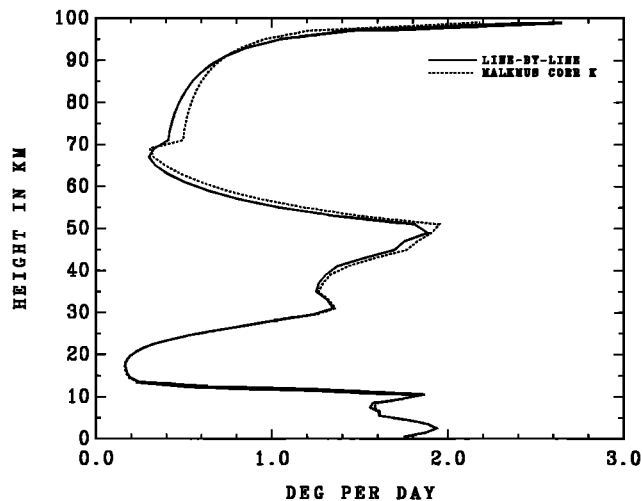


Fig. 16. Radiative cooling rate by atmospheric water vapor. The solid line is the line-by-line cooling rate computed for the McClatchey mid-latitude summer water vapor and temperature profiles using the AFGL 1982 line compilation. The correlated  $k$  distribution results are shown by the dashed line. Computational details are described in the text.

here are “unparameterized” in the sense that no ad hoc corrections have been made to improve the numerical fits. The band model parameters were least squares fitted to line-by-line results at each level of the atmosphere, and the resulting set of band model parameters was used to compute the vertically correlated  $k$  distributions and the resulting radiative cooling rates. We note that for each atmospheric level and spectral interval, only two band model parameters are needed to represent the equivalent nongray properties of the full line-by-line spectrum.

There is, nevertheless, a systematic overestimate of stratospheric cooling (typically by about 5% above the 30-km level) in all of the correlated  $k$  distribution comparisons presented below. This overestimate is attributable to the basic difficulty of the Malkmus band model in fitting Doppler regime line-by-line transmissions, and not to the lack of correlation between stratospheric  $k$  distributions. We have checked this using numerical  $k$  distributions, and Goody *et al.* [1989] have demonstrated the general capability of the correlated  $k$  distribution method (using numerical  $k$  distributions) to reproduce line-by-line flux divergences to better than 1% accuracy even for the very pathological case of  $\text{CO}_2$  in the 5000–5050  $\text{cm}^{-1}$  spectral interval.

Our purpose in this study is to demonstrate the overall utility of the Malkmus model, including its limitations, for atmospheric cooling rate computations. As the following comparisons indicate, the Malkmus model based correlated  $k$  distribution results are in excellent agreement with line-by-line calculations in the tropospheric Lorentz line regime, but produce a systematic overestimate in the middle and upper stratosphere. To bring the stratospheric results in better agreement with the line-by-line calculations, simple parameterizations, such as scaling the stratospheric absorber amount are possible. This procedure to improve the accuracy of  $\text{CO}_2$  stratospheric cooling was adopted in the stratospheric version of the GISS GCM [Rind *et al.*, 1988].

### 5.1. Water Vapor

Water vapor is the principal absorbing gas in the atmosphere, with absorption lines spanning the entire spectrum. It has a characteristic vertical distribution where most of atmospheric water vapor is concentrated in the lower troposphere near the ground, diminishing to a small but not negligible concentration within the stratosphere. As shown in Table B1, the rotational band (0–700  $\text{cm}^{-1}$ ) accounts for most of the line cooling by water vapor. The 6.3- $\mu\text{m}$  band contributes  $\sim 30\%$  of the cooling in the 50-km region and  $\sim 15\%$  near the ground; its contribution is near zero in the upper troposphere and lower stratosphere, with a small heating tendency ( $\sim 0.1^\circ\text{C/d}$ ) in the region above 60 km. The cooling by weak lines in the window region (700–1200  $\text{cm}^{-1}$ ) is important only in the lower troposphere, accounting for 35% of the cooling near the ground surface. In these comparisons, the contribution due to the water vapor continuum is not included.

Figure 16 shows the overall radiative cooling rate by water vapor lines for the McClatchey *et al.* [1972] mid-latitude summer temperature and water vapor profiles. Water vapor continuum opacity is an important contributor to tropospheric cooling rates, but since the continuum opacity is simply additive to the line opacity at each wavelength, we have not included it in our comparisons. As discussed in the ICRCCM comparisons [Luther and Fouquart, 1984], there is considerable uncertainty as to the proper treatment for water vapor line wing and continuum absorption. A comprehensive discussion and self-consistent treatment of water vapor line shape, line wing cutoff, and continuum absorption is presented by Clough *et al.* [1989]. All of these improvements in line-by-line calculation techniques can be readily incorporated into the correlated  $k$  distribution approach simply by least squares fitting the band model parameters to the improved line-by-line calculations. The solid line shows the line-by-line cooling rate results, and the dashed line depicts the correlated  $k$  distribution results. Although water vapor is considered to be primarily a tropospheric gas, the stratospheric cooling by water vapor in the 20- to 60-km altitude range is also significant. Cooling by water vapor exceeds cooling by  $\text{CO}_2$  in the 20- to 30-km altitude range, and contributes 10–20% of the cooling in the 50-km altitude region.

As noted above, the comparison shows close agreement throughout the troposphere and in the stratosphere to about 30 km. The accuracy of the correlated  $k$  distribution cooling rates falls off above 30 km, where the assumption of “randomly distributed overlapping Lorentz lines” of the Malkmus model formulation becomes less representative of the physical conditions.

### 5.2. Carbon Dioxide

$\text{CO}_2$  is the principal radiative cooling gas in the stratosphere, where it plays a key role in determining the temperature structure. Atmospheric  $\text{CO}_2$  is very close to being uniformly mixed and, from an absorber distribution point of view, represents a simpler modeling task of the vertical correlation of  $k$  distributions. Nearly all of the radiative cooling by  $\text{CO}_2$  is contributed by the 15- $\mu\text{m}$  band (see Table B2). Only near the ground do the weak 10- $\mu\text{m}$  and the 4.3- $\mu\text{m}$  bands contribute as much as 10% of the cooling. Computations for  $\text{CO}_2$  are the same as for water vapor, and

the accuracy of fit to the line-by-line cooling rate is also similar to that obtained for water vapor, with excellent agreement throughout the troposphere and a systematic overestimate of the radiative cooling in the stratosphere for altitudes above 30 km. The solid line in Figure 17 shows the line-by-line computations for the radiative cooling by  $\text{CO}_2$ . The dashed line gives the correlated  $k$  distribution cooling rate.

$\text{CO}_2$  is of particular interest because of its continued gradual increase in atmospheric concentration due to anthropogenic activity and its role as the leading factor in the rise of global surface temperatures over the past century. Since both the expected signature of stratospheric cooling and global surface warming due to  $\text{CO}_2$  change are induced by radiative flux changes, it is important that the radiative cooling by  $\text{CO}_2$  be accurately computed.

The cooling rate comparisons in Figure 18 help to illustrate how the least squares fitting of band model parameters to line-by-line transmission provides significant improvement in the accuracy of cooling rate computations. The comparison shown is for the frequency range of  $590\text{--}600\text{ cm}^{-1}$  in the  $15\text{-}\mu\text{m}$   $\text{CO}_2$  band. Line-by-line results are shown by the solid line. The dashed line gives the cooling rate calculated using least squares fitted Malkmus parameters, while the dotted line depicts cooling rates calculated using the statistically defined Malkmus model parameters. Use of the statistical parameters greatly overestimates the stratospheric cooling below  $\sim 50$  km and results in poor agreement in the troposphere. Only in the upper stratosphere, above 50 km, are the statistical parameter cooling rates close to the line-by-line results. While compensating errors might yield closer agreement for the total band cooling, the above comparison is indicative of the uncertainties associated with using statistical band model parameters.

A further practical consideration of the correlated  $k$  distribution method is its applicability to climate modeling. In particular, the narrow-band  $k$  distribution approach is suitable for 1-D radiative convective model applications and has been used in a number of such studies [e.g., Wang *et al.*, 1976; Hansen *et al.*, 1981; Lacis *et al.*, 1981]. In these

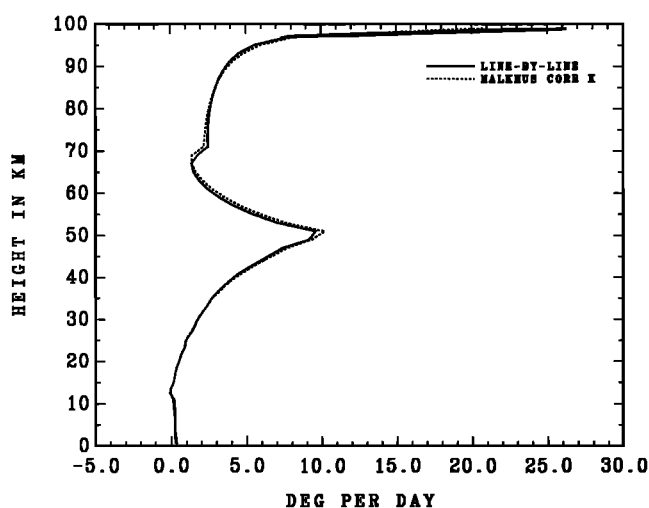


Fig. 17. Radiative cooling rate by  $\text{CO}_2$ . The solid line refers to line-by-line calculations for a 300-ppmv concentration for the McClatchey mid-latitude summer temperature profile. The dashed curve gives the correlated  $k$  distribution cooling rate.

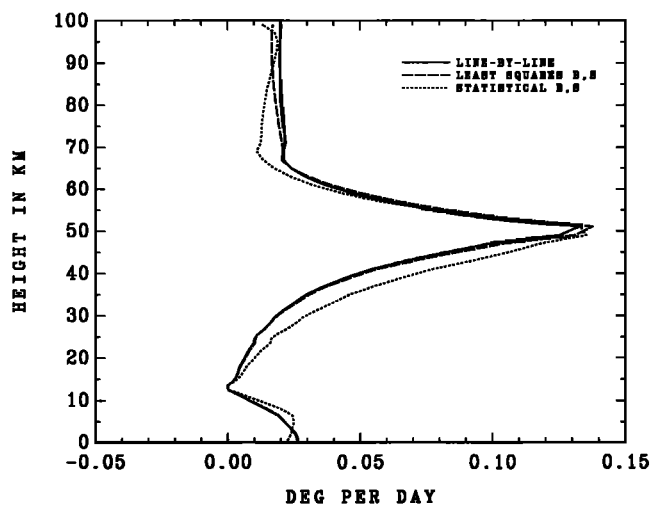


Fig. 18. Comparison of statistical and least squares fitted band model parameters in computing radiative cooling by  $\text{CO}_2$  in the frequency interval  $590\text{--}600\text{ cm}^{-1}$ . The solid line depicts line-by-line results; the dashed and dotted lines depict computations using least squares fitted and statistical band model parameters, respectively.

applications, the band width resolution used for  $\text{CO}_2$  was, on average,  $\sim 50\text{ cm}^{-1}$  from  $450$  to  $1100\text{ cm}^{-1}$ , with typically 10  $k$  intervals of nonuniform width used for the  $k$  distribution in each narrow-band interval. For 3-D GCM applications, computing speed becomes paramount. Accordingly, some additional parameterization of the  $k$  distribution approach is required. For this purpose, we used 10  $k$  intervals for the entire  $15\text{-}\mu\text{m}$   $\text{CO}_2$  band. (In the GISS GCM, four  $k$  intervals are used for the  $9.6\text{-}\mu\text{m}$  ozone band, and 11  $k$  intervals for  $\text{H}_2\text{O}$ .) While  $k$  distributions can be obtained for spectral intervals of arbitrary width, for very broad (or spectrally noncontiguous intervals), accuracy can be maintained by taking into account the spectral variation of the incident and emitted fluxes. The coefficients for the 10  $k$  intervals are thus obtained by convolving the Planck function and the narrow-band  $k$  distributions across the  $15\text{-}\mu\text{m}$   $\text{CO}_2$  band. This results in a large table of Planck-weighted, spectrally merged  $k$  distribution coefficients which can be interpolated in pressure, temperature, and absorber amount. Figure 19 shows a comparison of the radiative cooling rate for  $\text{CO}_2$  between line-by-line calculations, the correlated  $k$  distribution method, and a spectrally merged correlated  $k$  distribution parameterization that is used to compute radiative cooling rates in the GISS 3-D GCM [Hansen *et al.*, 1983].

The results for  $\text{CO}_2$  show generally good accuracy throughout the troposphere. Both underestimates and overestimates of the radiative cooling rate occur in the stratosphere where the Malkmus model applicability begins to break down. It is more likely, however, that the major part of the error in stratospheric cooling is attributable to the inadequacy of the  $k$  interval and/or vertical resolution that was used in setting up the original parameterization, since the GCM radiation was initially developed for tropospheric applications. A more detailed description of the parameterized correlated  $k$  distribution treatment in the GISS GCM will be presented in a separate paper.

### 5.3. Ozone

Ozone radiative cooling provides another important test example for the correlated  $k$  distribution method. The non-

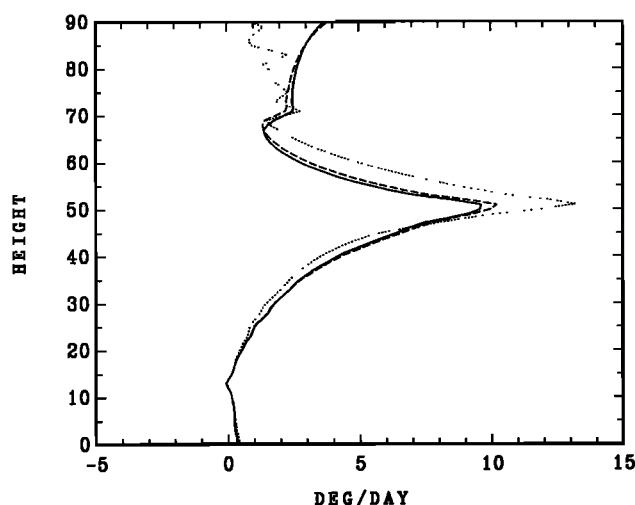


Fig. 19. Radiative cooling rate for  $\text{CO}_2$ . Results shown are for 300 ppmv for the McClatchey mid-latitude temperature profile. The solid line depicts line-by-line results; the dashed line gives the correlated  $k$  distribution results; the dotted line shows the spectrally merged correlated  $k$  distribution results computed with the GISS 3-D GCM radiation code.

uniform distribution of ozone has been historically a difficult case to handle for other radiative transfer methods, such as the Curtis-Godson approximation [e.g. *Walshaw and Rodgers*, 1963; *Goldman and Kyle*, 1968]. In earlier calculations [*Lacis et al.*, 1979], we obtained close agreement between line-by-line and correlated  $k$  distribution cooling rate calculations for the  $9.6\text{-}\mu\text{m}$   $\text{O}_3$  band. Here, we also include contributions from the  $14\text{-}\mu\text{m}$  band as well as from the  $\text{O}_3$  rotational band from 0 to  $160\text{ cm}^{-1}$ , and from the weak  $2100\text{ cm}^{-1}$  band. The relative importance of these contributions may be compared in Table B3. The  $14\text{-}\mu\text{m}$  band contributes about 25% of the outgoing flux and about 33% of the downward flux at the ground due to ozone, and accounts for about 20% of the ozone cooling rate between 20 and 40 km. These relative comparisons, however, apply for the case of pure ozone; in the real atmosphere, the  $14\text{-}\mu\text{m}$  band contribution is greatly suppressed by the strong overlapping absorption due to  $\text{CO}_2$ . The contributions from the rotational band and the  $2100\text{ cm}^{-1}$  band are negligible.

Figure 20 shows the line-by-line (solid line) and correlated  $k$  distribution results (dashed line) for the  $\text{O}_3$  cooling rate. Again, the correlated  $k$  distribution results are in excellent agreement with the line-by-line calculations below 30 km, with a small systematic overestimate of the stratospheric cooling above the 30-km level. Through much of the atmosphere, the absorption of upwelling radiation by ozone dominates self-emission, producing heating in the upper troposphere and lower stratosphere between 5 and 29 km, as well as in the upper stratosphere above the 62-km level.

Our radiative cooling rate profiles for ozone appear to agree well below  $\sim 30$  km with those obtained by *Kratz and Cess* [1988]. Differences evident at higher altitudes can be attributed to the different vertical resolution employed. In particular, placement of the atmospheric top at 50 km by *Kratz and Cess* overestimates ozone cooling in the top layer of the atmosphere and does not allow for the gradual decrease in cooling with height. In their comparison to

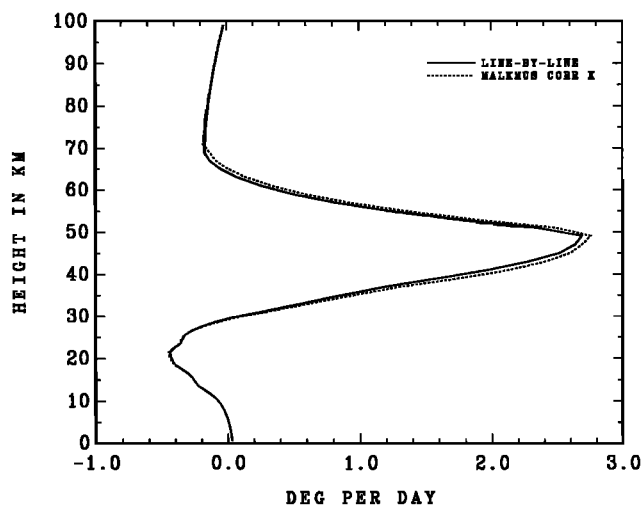


Fig. 20. Radiative cooling rate by ozone. The solid line depicts line-by-line results for the McClatchey mid-latitude summer ozone and temperature distributions. The dashed line gives the correlated  $k$  distribution results.

line-by-line cooling, *Kratz and Cess* note that total band absorptance for the narrow-band model results is in precise agreement with line-by-line results over homogeneous paths, and conclude that the  $\sim 10\%$  underestimates of the cooling by their narrow-band model results is attributable to the classical mismatch between Curtis-Godson scaling and the characteristic ozone distribution with large amounts of ozone at small pressures and small amounts at high pressure. It is this limitation of the Curtis-Godson scaling approximation that makes the correlated  $k$  distribution method a more general and flexible approach for modeling the vertical inhomogeneity of the atmosphere.

#### 5.4. Methane and Nitrous Oxide

The cooling rate comparisons for methane and nitrous oxide address two separate aspects of the correlated  $k$  distribution concept. The first aspect is simply a direct comparison of the atmospheric cooling rate profile to line-by-line results, as in the case for water vapor,  $\text{CO}_2$ , and ozone. Figures 21a and 21b show the individual cooling rates for  $\text{CH}_4$  and  $\text{N}_2\text{O}$ , respectively, with the solid lines depicting line-by-line results, and the dashed lines giving the cooling rates computed with the correlated  $k$  distribution method. The spectral range covered is  $1100\text{--}1350\text{ cm}^{-1}$  for both gases. Significant cooling is also contributed by the  $4.7\text{-}$  and  $15\text{-}\mu\text{m}$  bands of  $\text{N}_2\text{O}$ , but these two bands do not directly overlap  $\text{CH}_4$  and thus are not included in our comparison. The quality of fit to the line-by-line cooling results is similar to those obtained previously for water vapor,  $\text{CO}_2$ , and ozone. Unlike water vapor and  $\text{CO}_2$ , methane and  $\text{N}_2\text{O}$  exhibit stratospheric warming above the 60-km level because the absorption of upwelling radiation dominates self-emission due to the stronger temperature dependence of Planck radiation in the  $7\text{-}$  to  $8\text{-}\mu\text{m}$  region. Likewise,  $\text{CH}_4$  and  $\text{N}_2\text{O}$  produce heating in the upper troposphere and lower stratosphere between 6 and 23 km. The methane and  $\text{N}_2\text{O}$  results are computed for 1.6 and 0.35 ppmv concentrations, respectively.

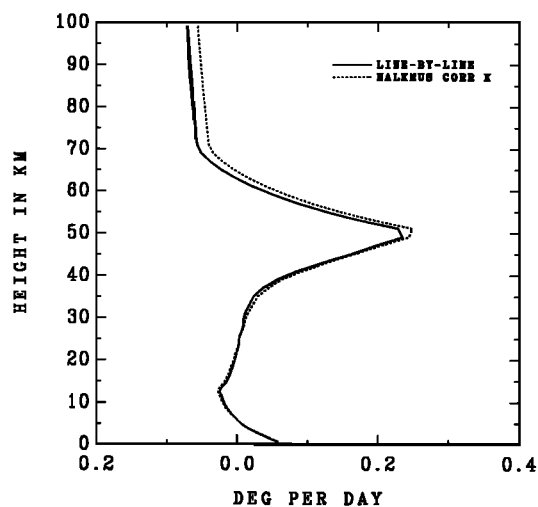


Fig. 21a

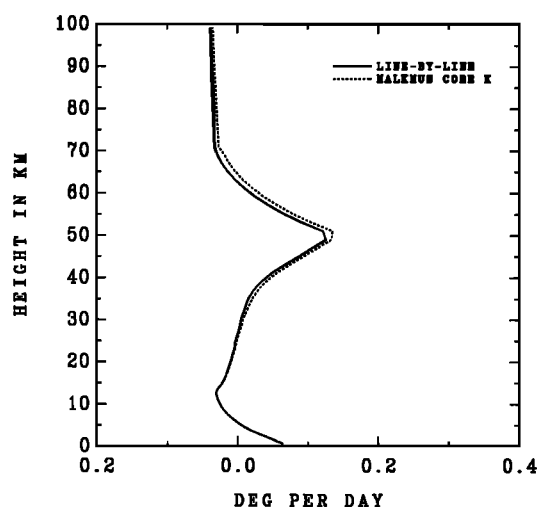


Fig. 21b

Fig. 21. (a) Radiative cooling rates by  $\text{CH}_4$  for 1.6-ppmv concentration and (b)  $\text{N}_2\text{O}$  for 0.35 ppmv. The solid line depicts line-by-line calculations; the dashed line refers to correlated  $k$  distribution results. The  $\text{N}_2\text{O}$  cooling rate includes contributions only from the 7- to 8- $\mu\text{m}$  region.

The second aspect of this comparison is directed toward the question of overlapping absorption.  $\text{CH}_4$  and  $\text{N}_2\text{O}$  overlap strongly in the 7- to 8- $\mu\text{m}$  region and provide an excellent example to test the accuracy of the correlated  $k$  distribution treatment for overlapping gases described in section 3.3. For this purpose, we use the line-by-line computations to model the overlapping absorption explicitly and compare the results against those obtained using the correlated  $k$  distribution gaseous overlap treatment. The combined cooling rate profile computed with explicit line-by-line overlapping absorption is shown by the solid line in Figure 22, and the correlated  $k$  distribution results are given by the dashed line. As expected, the results show a linear superposition of the downward fluxes and cooling rates throughout the stratosphere, where the overlap is essentially optically thin. In the 20- to 30-km range, the combined cooling rate for  $\text{CH}_4$  and  $\text{N}_2\text{O}$  is paradoxically greater than the sum of the individual cooling rates (see Table B4). This counterintuitive result

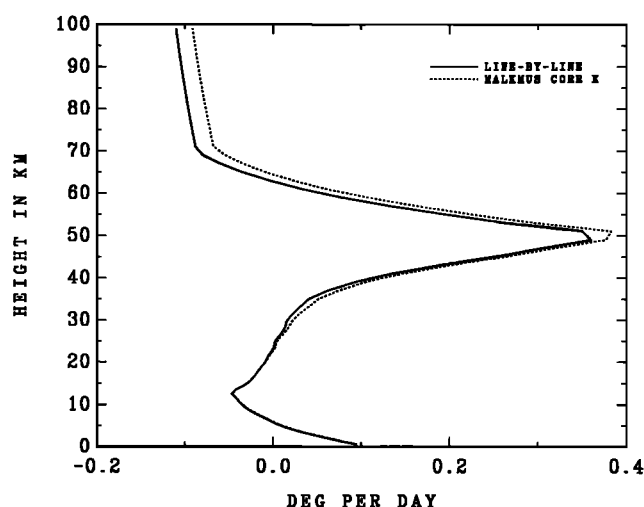


Fig. 22. Radiative cooling rate due to overlapping absorption by  $\text{CH}_4$  and  $\text{N}_2\text{O}$ . Explicit line-by-line overlap calculations are shown by the solid line. Correlated  $k$  distribution treatment of overlapping absorption is given by the dashed line.

arises from the proportionately greater reduction in the upwelling flux in the overlapping case compared to the reduction in the downwelling and self-emission components. As a result, the reduced warming due to decreased absorption of the upwelling radiation produces an increase in cooling.

We used the recipe provided by (32) and (33) to compute the overlapping  $k$  distributions of  $\text{CH}_4$  and  $\text{N}_2\text{O}$ . The band model coefficients were least squares fitted separately for each gas at each atmospheric level. The close agreement for both individual and overlapping cooling rates corroborates the correlated  $k$  distribution treatment of overlapping absorption by two different gases, at least in the case of  $\text{CH}_4$  and  $\text{N}_2\text{O}$ . Likewise, the assumption that the  $\text{CH}_4$  and  $\text{N}_2\text{O}$  spectra are uncorrelated is upheld. The nature of the stratospheric cooling rate overestimate above the 30-km level is basically unaffected by the overlap treatment.

## 6. MULTIPLE SCATTERING

It is well known that multiple scattering, even in the case of homogeneous media, requires explicit accounting for nongray absorption. Current practice, more often than not, still attempts to represent nongray absorption in terms of some scaled equivalent gray absorber amount. Multiple scattering by clouds, aerosols, and gas molecules causes the incoming photons to undergo different numbers of scattering events and to travel different path lengths before emerging as diffusively reflected or transmitted radiation. Only a fraction  $e^{-\tau/\mu}$  of the incident beam emerges unscattered, traveling in the original direction  $\mu$  for which scaling approximations are applicable.

Many different computational schemes are available for modeling the effects of multiple scattering [cf. Hansen and Travis, 1974]. We use the doubling and adding method [Lacis and Hansen, 1974] to compute the effects of multiple scattering. The basic input parameters for the doubling method are the total optical thickness  $\tau$ , the single scattering albedo  $\omega$ , and the phase function which controls the angular dependence of scattering. To illustrate the multiple scattering

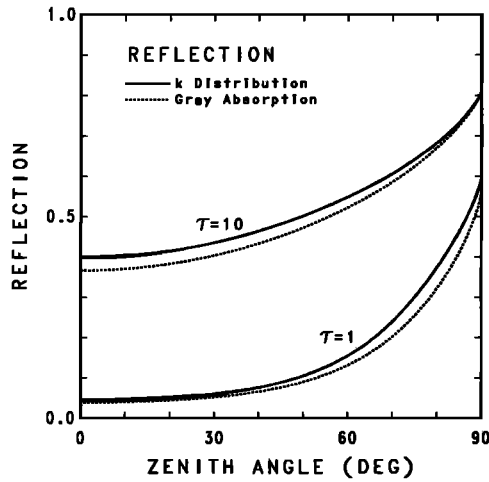


Fig. 23a

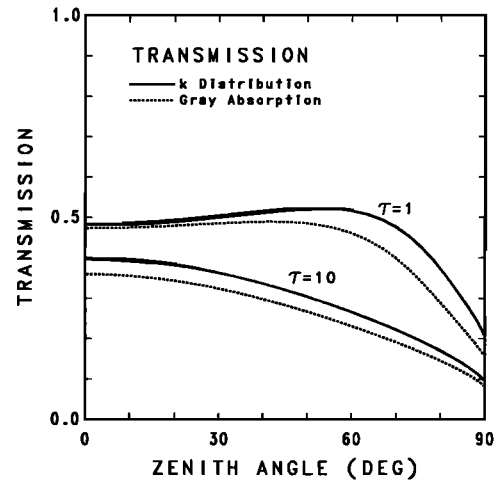


Fig. 23b

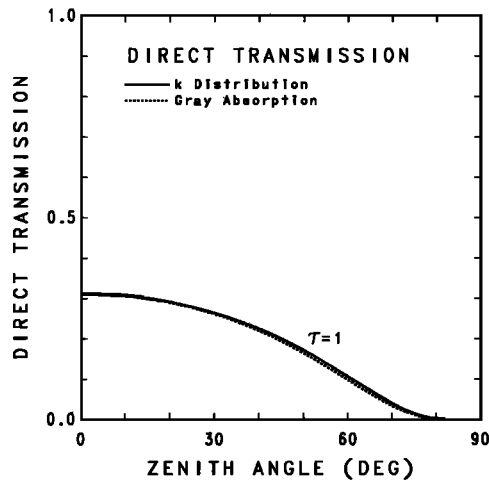


Fig. 23c

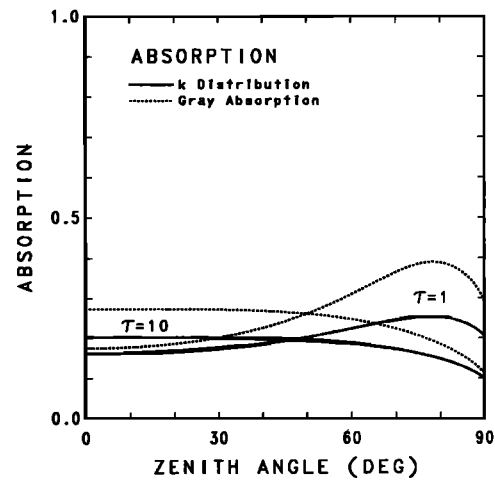


Fig. 23d

Fig. 23. Effect of nongray gaseous absorption on multiple scattering calculations. (a) Reflection, (b) diffuse transmission, (c) direct transmission, and (d) absorption are computed for nongray (solid line) and gray (dotted line) cases for cloud scattering optical thicknesses of  $\tau = 1$  and 10 using the doubling and adding method. The nongray gaseous absorption is included by using the  $k$  distribution for Malkmus band model parameters  $B = 0.01$  and  $S = 1$  with unit absorber amount. For the grey case, the mean absorption is set to be identical to the nongray absorption for zenith angle  $0^\circ$ .

effect, we use a Mie scattering phase function computed for visible wavelengths and a cloud particle effective radius of  $10 \mu\text{m}$ , corresponding to typical strongly forward scattering fair-weather water clouds with asymmetry parameter  $\sim 0.85$ .

Multiple scattering methods generally require monochromatic or spectrally uniform absorption specification. Accordingly, the multiple scattering calculations are performed for each subinterval of the  $k$  distribution, and the results are summed over the cumulative probability subintervals  $\Delta g_i$ . The spectrally integrated reflection and transmission are thus obtained in the form

$$R = \sum_i^N R(\tau_i, \omega_i) \Delta g_i \quad (34) \quad \text{and}$$

and

$$T = \sum_i^N T(\tau_i, \omega_i) \Delta g_i \quad (35)$$

respectively, where  $N$  is the number of  $k$  distribution subintervals, and  $R(\tau_i, \omega_i)$  and  $T(\tau_i, \omega_i)$  represent hemispherically integrated quantities to yield the plane albedo and transmission, respectively. The input parameters to include the nongray absorption for doubling and adding are specified by

$$\tau_i = \tau_{c,x} + k_i u \quad (36)$$

$$\omega_i = \frac{\tau_{c,s}}{\tau_{c,x} + k_i u} \quad (37)$$



where  $k_i$  is the mean absorption coefficient in the  $i$ th  $k$  distribution subinterval,  $u$  is the absorber amount, and  $\tau_{c,x}$  and  $\tau_{c,s}$  are the cloud extinction and scattering optical depths, respectively.

The cloud reflection and transmission are computed for two illustrative examples with  $\tau_{c,s} = 1$  and  $\tau_{c,s} = 10$ , using a single homogeneous layer to represent the cloud and overlapping gaseous-type absorber. The overlapping nongray absorber is assumed to have a mean absorption depth of unity (as in Figure 6) and to be characterized by Malkmus band model parameters  $B = 0.01$  and  $S = 1$ , representative of midtropospheric gas absorption. In making our comparisons, we use the recipe provided by (26) to define both gray and nongray absorption coefficients required as input for the gaseous absorber in (36). This way, both the gray and nongray cases will yield identical absorption over a homogeneous nonscattering path. To have set the mean absorption coefficient for the gray case based on the mean absorption depth  $Su$  (valid only in the optically thin limit) would have been unnecessarily crude.

The solid lines in Figures 23a and 23b depict the reflected and (diffusely) transmitted radiation as a function of the solar zenith angle computed with the  $k$  distribution method using 10 subintervals of  $\Delta g_i$  to resolve the nongray absorption. The dotted lines show the corresponding results obtained with a single  $k$  distribution interval (representing the gray absorption case). The results show decreases in both reflected and transmitted radiation in the case of the gray approximation. The differences are roughly 10% for the examples shown; they exhibit a solar zenith angle dependence of the error that reflects the amount of multiple scattering encountered by the emerging beam, i.e., for the smaller optical depth the error is largest for large zenith angles, while for the larger optical depth the error is largest near normal incidence.

Figure 23c shows that even for direct transmission there is a difference between the gray approximation and the nongray  $k$  distribution treatment. This error arises because the gray approximation, by virtue of its definition, always overestimates absorption in the weakly absorbing line wings and underestimates absorption in the strongly absorbing line centers. These two errors just balance each other at the point where the mean absorption coefficient is defined, i.e., for the absorber path corresponding to  $\mu = 1$  in the present example. Because of the exponential dependence of absorption on absorber path length, the cancellation of this error cannot be maintained as the absorber path length changes. As a result, the gray approximation will overestimate absorption at the longer absorber paths unless some form of absorber scaling is introduced to compensate. The direct transmission curves shown in Figure 23c are for the  $\tau_{c,s} = 1$  case, as direct transmission for  $\tau_{c,s} = 10$  is negligible.

The total absorption within the cloud layer attributable to the absorbing gas is shown in Figure 23d. Here, the largest disagreement between gray and nongray treatment of gaseous absorption again occurs in situations where multiple scattering effects are greatest, i.e., at large zenith angles for small cloud optical thickness and at small zenith angles for optically thick clouds. The results show that the gray approximation can overestimate gaseous absorption in clouds by as much as 50%. Thus there is need to model the nongray gaseous absorption explicitly, even in the case of a homogeneous medium.

We have not attempted, as part of this study, to combine

the line-by-line and multiple scattering calculations into a single comprehensive calculation that would incorporate cloud scattering into the vertically inhomogeneous atmosphere. A practical reason for not doing so is the disproportionate amount of computer time required for even a small spectral interval. A second reason is that the results obtained for a plausible example of, say, a single layered stratus cloud imbedded in an absorbing atmosphere would really be no different from the results already obtained in the previous section and those described in Figure 23. It should be remembered that in the correlated  $k$  distribution approach, each individual  $k$  interval is computed in isolation from all others through the entire atmospheric column. Thus each  $k$  interval is treated as if it were in fact monochromatic. As a result, the absorption contributions that occur over a distribution of photon paths within the cloud layer can be accurately modeled by any appropriate multiple scattering algorithm to compute the fraction of the incident light beam that is absorbed within the cloud. Similarly, precise fractions (as determined by the multiple scattering algorithm) of the incident beam will be reflected and diffusely transmitted by the cloud.

The problem of validating the correlated  $k$  distribution treatment of multiple scattering in a vertically inhomogeneous atmosphere is very much the same as validating the correlated  $k$  distribution treatment of gaseous absorption in a nonscattering atmosphere. If, for example, the  $k$  distributions were to be perfectly correlated with height, they would have the same monochromatic properties as the line-by-line spectrum, so that computations for multiple scattering would be identical in these two cases. The principal effect of the multiple path length distribution arising from multiple scattering is to require narrower  $k$  interval resolution to maintain a given precision. This is because, in the case of multiple scattering, the absorber scaling provided by the cumulative transmission digitization (section 3.4) is defined for a fixed path length; hence a higher  $k$  interval resolution is needed to compensate for the path length distribution caused by multiple scattering. As in the nonscattering atmosphere case, the required resolution can be determined by varying the  $k$  interval width until radiative quantities of interest, like the outgoing flux, no longer respond to a change in resolution.

Thus, for the single layered stratus cloud imbedded in an absorbing atmosphere, the correlated  $k$  distribution treatment should give the same accuracy fit to line-by-line data in the nonscattering case. The more pathological case of multiple scattering between a high cirrus cloud overlying a low stratus cloud in an absorbing atmosphere may provide a more difficult test for the correlated  $k$  distribution, and therefore should be investigated with explicit line-by-line calculations.

## 7. DISCUSSION

The Malkmus model, utilizing only two parameters, can successfully characterize and represent the considerable complexity of the line-by-line spectrum over a wide range of pressures, temperatures, and absorber amounts. Real difficulty in reproducing the line-by-line spectrum occurs only in the upper stratosphere, where line shapes deviate significantly from Lorentzian.

The following question raised by Fels in reviewing this manuscript probes at the heart of the Malkmus model based

correlated  $k$  distribution approach. "If the (Malkmus) treatment of Doppler effects is so poor (Figure 9), why are the results at 1 mb for CO<sub>2</sub> and O<sub>3</sub> (Figures 17 and 20) so good?"

The answer is, in part, that the Malkmus model correlated  $k$  distribution, with the least squares fitted band model parameters, reproduces to first order the essential features of line-by-line calculations. These are (1) in the stratosphere, wing absorption is so small that essentially 99% of each spectral interval is absorption free; and (2) the transmission (absorption) in the remaining 1% of the interval is least squares fitted to match line-by-line results for a specified range of absorber amount that is characteristic of the stratospheric layering used. The gradient of the  $k$  distribution that is so poorly represented by the Malkmus model in the Doppler regime (and the resulting poor fit of absorption versus absorber amount) is apparently of secondary importance, though it clearly is the source of the stratospheric cooling rate error. The Malkmus representation of the Doppler regime is too "gray," in that absorption coefficients of the  $k$  distribution are too strong in weakly absorbing regions and too weak in strongly absorbing regions. This leads to overestimated absorption over longer absorber paths (as when integrating over emission angle), a characteristic of the gray approximation that produces excess cooling.

A quantitative evaluation of the contributing components of radiative heating/cooling in a nongray medium is complicated by the fact that the radiative fluxes cannot be treated as scalar quantities, i.e., the effective temperature of the upwelling and downwelling components may be quite different within individual  $k$  distribution subintervals. Thus, while the self-emission (cooling) term of a given layer may be obtained accurately (as long as the absorption coefficients reproduce the layer mean absorption), an accurate  $k$  distribution is needed to calculate the heating contributions within each  $k$  interval arising from the absorption of upwelling and downwelling flux components with widely different emission temperatures.

Earlier studies, e.g., Kiehl and Ramanathan [1983] for CO<sub>2</sub> and Cess *et al.* [1986] for CH<sub>4</sub>, have shown that the accuracy of narrow-band model results depends on the width of the spectral intervals used to model the spectrum, and that significant errors result if the Goody or Malkmus models are applied to spectral intervals larger than 10 cm<sup>-1</sup>. Cess *et al.* [1986] point out that the band model accuracy diminishes significantly as the width of the spectral intervals becomes less than 5 cm<sup>-1</sup> because the line statistics become more variable with fewer lines in the selected spectral interval. Cess *et al.* further demonstrate this sensitivity to changing line statistics by using a fixed width spectral interval (5 cm<sup>-1</sup>) and shifting the starting location of the interval by small increments.

These errors in band model transmission encountered by Kiehl and Ramanathan [1983] and Cess *et al.* [1986] arise primarily from the variability of line statistics across the spectrum and the fact that these distributional variations of line strengths and positions are not fully represented by the basic band model parameter definition. By least squares fitting the band model parameters directly to the line-by-line calculated transmissions for a prescribed range of absorber amounts and pressure-temperature combinations of interest, we effectively eliminate this source of error even for large variations in the width of the spectral interval.

The least squares fitting of Malkmus model parameters to

line-by-line transmission effectively transfers the accuracy of the line-by-line calculations to the band model parameters and permits the full utilization of the Malkmus model properties for obtaining  $k$  distribution representations of the line spectra and to correlate these  $k$  distributions vertically to simulate line-by-line modeling of the pressure-temperature inhomogeneity of the atmosphere. Also important is the cumulative transmission capability of the Malkmus model, which allows arbitrary digitization of the  $k$  distribution without loss of transmission accuracy for homogeneous absorber paths. The automatic scaling in absorber amount that this provides within each  $k$  interval permits flexible trade-offs between computing time and numerical precision when modeling the inhomogeneous atmosphere.

Cess *et al.* [1986] describe a regression fit to line-by-line calculations to improve the accuracy of band model fit to the CH<sub>4</sub> transmission. This is equivalent to using a one-parameter fit for the band model  $S$  coefficient. However, in most cases of least squares fitting to line-by-line transmissions, it is the Malkmus  $B$  coefficients that requires the larger adjustment to achieve an optimum fit.

The practical limitations in the least squares fitting of Malkmus band model parameters to line-by-line results stem from the basic inability of the Malkmus model to fit the single Lorentz line and Doppler regime  $k$  distributions. Nevertheless, even for these cases, it is possible to obtain least squares fits to line-by-line transmission (or absorption) over a selected absorber range to within 1–2% accuracy, with somewhat larger errors in the corresponding cooling rates. Thus there is considerable flexibility in selecting the width of spectral intervals, since spectral intervals containing even a single line can be accommodated, though with somewhat reduced accuracy. Likewise, there is no hard upper limit for the width of spectral intervals, but it becomes necessary to account for the spectral dependence of the incident (and/or emitted) radiation.

The results obtained above show that the correlated  $k$  distribution method produces accurate radiative cooling rates throughout most of the atmosphere, and that the correlated  $k$  distribution approach is capable of modeling gaseous absorption in a vertically inhomogeneous atmosphere at a small fraction of the computing cost required for line-by-line calculations. The correlated  $k$  distribution results presented here are in a form most directly applicable to 1-D radiative-convective climate model computations; for 3-D applications, additional parameterization is needed.

In our comparisons with line-by-line cooling rates, the band model parameters were least squares fitted to line-by-line transmissions at each level of the atmosphere. Hence the problem of interpolating band model parameters in pressure or temperature was avoided. In more typical applications, the  $B$  and  $S$  parameters would form a tabulated grid spanning the range of pressures and temperatures expected in the radiative modeling of the atmosphere. Our 1-D model interpolation utilizes three points in temperature (to span 200–300°C) and three to four points per decade of the pressure range for each contributing gas with spectral intervals ranging from 20 to 100 cm<sup>-1</sup> in width. The interpolation is quadratic in temperature and linear in log pressure. Except in the region of the Lorentz/Doppler transition near ~10 mbar, interpolation errors in the  $B$  and  $S$  parameters are generally negligible.

The correlated  $k$  distribution method has proven itself

adaptable and useful for studying radiative transfer problems in climate-related applications. Since the full effects of pressure broadening and temperature dependence are automatically and explicitly included in the  $k$  distributions via line-by-line calculations, separate effort is not required to account for hot bands or Lorentz/Doppler line shape changes.

#### APPENDIX A: RADIATIVE COOLING RATE COMPUTATION

We use the McClatchey *et al.* [1972] standard atmosphere mid-latitude summer profile as the reference temperature profile, which gives temperatures at 1-km intervals with larger intervals for heights above 25 km. For better vertical resolution, we linearly interpolate the temperature at 1-km intervals above the 25-km level. This temperature profile has been used as a reference profile for radiative transfer comparisons by the ICRCCM radiative transfer comparisons group [Luther and Fouquart, 1984].

##### Thermal Emission From an Isolated Layer

To compute the thermal emission from an isolated atmosphere layer, some type of intralayer temperature gradient must be specified. Rather than use a large number of isothermal sublayers, we take the intralayer temperature gradient to be linear in Planck radiation. This approach has a number of practical advantages at little cost to modeling accuracy. As illustrated in Figure A1, a pencil beam of thermal radiation is emitted by a thin element of an isolated atmospheric layer in the direction  $\theta$  relative to the vertical. This differential emission is given by

$$dE(\mu) = B_\nu(\tau') e^{-\tau'/\mu} d\tau'/\mu \quad (\text{A1})$$

where the emission angle is defined by  $\mu = \cos(\theta)$  and where  $B_\nu(\tau')$  is the Planck radiation within the spectral interval  $[\nu_1, \nu_2]$ ; the local temperature within the layer is implicitly prescribed by its assumed linear dependence on the Planck radiation, i.e., at the point  $\tau'$  on the relative scale set by the optical depth  $\tau$ ,

$$B_\nu(\tau') = B_\nu(T_t) + \tau'/\tau [B_\nu(T_b) - B_\nu(T_t)] \quad (\text{A2})$$

where  $B_\nu(T_t)$  is the Planck function evaluated at the layer top edge temperature  $T_t$ , with  $B_\nu(T_b)$  similarly defined at the bottom edge of the layer.

For this temperature dependence of the intralayer temperature gradient, the integrated thermal emission from the entire layer can be obtained in closed form. Thus the intensity of the thermal radiation emitted in the direction  $\mu$  by the isolated atmospheric layer in Figure A1 is

$$E(\mu) = B_\nu(T_t) - B_\nu(T_b) + \{B_\nu(T_b) + \mu/\tau [B_\nu(T_b) - B_\nu(T_t)]\} (1 - e^{-\tau/\mu}) \quad (\text{A3})$$

for the upward directed radiation, and

$$E^*(\mu) = B_\nu(T_b) - B_\nu(T_t) + \{B_\nu(T_t) - \mu/\tau [B_\nu(T_b) - B_\nu(T_t)]\} (1 - e^{-\tau/\mu}) \quad (\text{A4})$$

for the downward directed radiation.

For small optical thickness, the apparent singularity in the

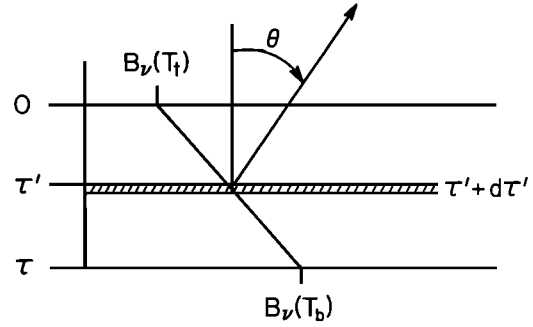


Fig. A1. Thermal emission from an isolated atmospheric layer with temperature gradient linear in Planck function.

thermal emission is removed by using a few terms of series expansion forms of (A3) and (A4), i.e.,

$$E(\mu) = \sum_{n=1}^{\infty} (-1)^{n+1} \frac{(B_t + nB_b)}{(n+1)!} (\tau/\mu)^n \quad (\text{A5})$$

and

$$E^*(\mu) = \sum_{n=1}^{\infty} (-1)^{n+1} \frac{(B_b + nB_t)}{(n+1)!} (\tau/\mu)^n \quad (\text{A6})$$

respectively. In the above,  $B_t$  and  $B_b$  represent the Planck radiation within the spectral interval  $[\nu_1, \nu_2]$  evaluated at the top and bottom layer temperatures, respectively.

Choosing the layer temperature gradient to be linear in Planck radiation simplifies the numerical procedure for integrating over the vertical extent of the atmosphere and requires fewer layers to achieve the same overall numerical precision for the calculation of radiative fluxes and cooling rates, as can be verified by using a large number of atmospheric layers. This approximation does have a physically undesirable property in that the temperature gradient becomes a function of wavelength; however, this is not a significant source of error if the temperature difference between the top and bottom edges of the individual atmospheric layers is kept small, say,  $\Delta T < 5$  K. This error is largest in the limit of small optical thicknesses when the emitted radiation “sees” the full interior structure of the layer; the error disappears completely in the limit of large optical thickness when the emitted radiation originates from the outer edges of the layer. Also, this error is negligible at long wavelengths but becomes increasingly important toward shorter wavelengths due to the stronger temperature dependence of the Planck function.

The dependence of this (maximum) error on the layer top-to-bottom temperature differential is illustrated in Figure A2 for three different reference temperatures, and displayed as the percent difference in emitted flux between the linear-in-Planck and the linear-in-temperature gradients. For wavelengths longer than  $6 \mu\text{m}$ , the maximum error is less than 0.1% for layer edge temperature differences of 5 K. Thus the inconsistency attributable to the slight wavelength dependence of the intralayer temperature gradient is far smaller

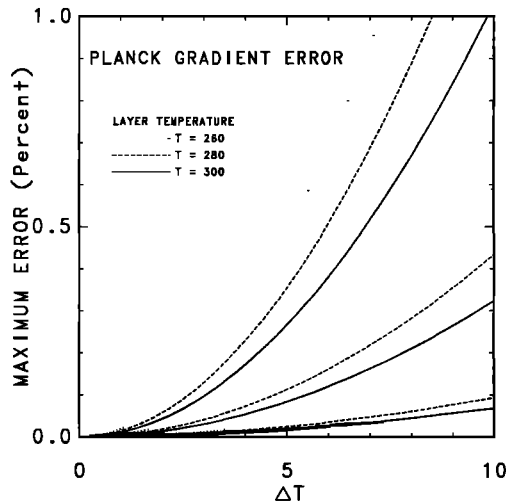


Fig. A2. Spectral dependence of maximum error in thermal emission for intralayer temperature gradients linear in Planck emission and linear in height. The dotted, dashed, and solid lines refer to layer bottom temperatures of 260, 280, and 300 K, respectively, for wavelengths (top to bottom) of 2500, 1500, and 800  $\text{cm}^{-1}$ .

than errors due, for example, to use of isothermal sublayers to approximate the intralayer temperature gradient.

#### Integration Over Emission Angle

The above formulas give the directional intensity of thermal emission from an isolated layer for specified values of  $\mu$ . Computation of atmospheric cooling rates requires knowledge of the upward and downward directed radiative fluxes. Hence we need to integrate the thermal intensities over the emission angle range, i.e.,

$$E = \int_0^1 E(\mu) \mu d\mu \quad (\text{A7})$$

A closed form integral over the emission angle is available in terms of exponential integral functions. Exponential integrals, however, are not always practical for modeling thermal cooling in multilayered atmospheres, since they require an  $N^2$  dependent computing effort, where  $N$  is the number of layers. Moreover, exponential integrals are not applicable in cases where multiple scattering effects need to be included.

A more flexible approach is to compute integrals over emission angle numerically such as by using a Gaussian quadrature to evaluate integrals of the type described by (A7), i.e.,

$$E = \sum_{i=1}^N E(\mu_i) \mu_i w_i \quad (\text{A8})$$

where the intensity is evaluated for the specified directions of  $\mu_i$  and weighted by corresponding Gaussian weights  $w_i$ . Normally, three quadrature points are all that is required to obtain fluxes to accuracies better than 1%. In the calculations presented here, we have used five Gaussian quadrature points to virtually eliminate this source of error. Figure A3 shows the percent error in angle-integrated transmission and absorption as a function of optical depth for different

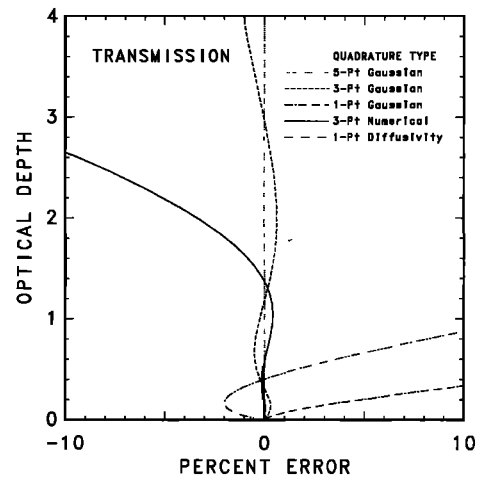


Fig. A3a

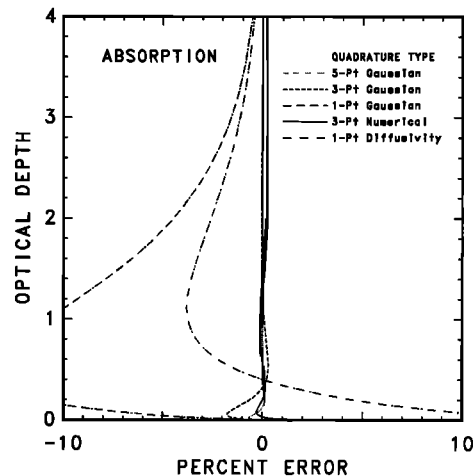


Fig. A3b

Fig. A3. Comparison of (a) transmission error and (b) absorption error as a function of optical thickness for emission angle integration. The dotted, dashed, and dot-dash lines depict integration by Gaussian quadrature. The errors for diffusivity factor are shown by the broken line, and by the solid line for the three-point numerical quadrature used in the GISS GCM.

numbers of Gaussian quadrature points. Also shown by the broken line is the error produced by the commonly used diffusivity factor approximation of  $\mu = 1/1.66$ .

The solid line in Figure A3 shows the error for the three-point numerical quadrature that is used in the GISS 3-D GCM to integrate the thermal intensities over emission angle. The emission angles are evaluated at  $\mu_i = 1, 0.5$ , and  $0.1$ ; the corresponding weight factors are:  $\mu_i w_i = 0.3825, 0.5742$ , and  $0.0433$ , respectively. The advantage of the above numerical quadrature is that it requires only a few extra multiplications to implement, while providing nearly the same accuracy as the three-point Gauss quadrature (requiring three exponentials to evaluate).

#### Thermal Emission From Stacked Layer Atmosphere

We represent the vertical inhomogeneity of the atmosphere by a stack of homogeneous layers. Each layer is

treated as being homogeneous with respect to absorption coefficient pressure and temperature dependence, but with an intralayer temperature gradient. This procedure permits accurate modeling of the transfer of thermal radiation within the atmosphere with a minimum number of layers.

We avoid the classical integral formulation [e.g., *Liou*, 1980] for computing the upward and downward directed longwave fluxes. Instead, we use the closed form expressions for the thermal emission which are valid for isolated atmospheric layers; we then use a layer "stacking" procedure to compute the upward and downward directed intensities. This results in a relatively simple form for the atmospheric thermal intensities because the computations are formulated in terms of uniform absorption coefficients along parallel light beam paths. Thus the recipe for obtaining the outgoing thermal intensity  $U_n(\mu_i)$  in the direction  $\mu_i$  at the top edge of the  $n$ th layer (for each  $k$  distribution subinterval) is obtained as follows:

$$\begin{aligned} U_0(\mu_i) &= B_\nu(T_0) \\ U_1(\mu_i) &= E_1(\mu_i) + U_0(\mu_i)e^{-\tau_{1i}/\mu_i} \\ &\vdots \\ U_n(\mu_i) &= E_n(\mu_i) + U_{n-1}(\mu_i)e^{-\tau_{ni}/\mu_i} \end{aligned} \quad (A9)$$

where  $B_\nu(T_0)$  is the Planck radiation emitted by the ground within the spectral interval  $[\nu_1, \nu_2]$ ,  $\tau_n$  is the column optical thickness of the  $n$ th layer, and  $E_n(\mu_i)$  is the isolated layer emission given by (A3). The outgoing intensity at the top of the atmosphere in the direction  $\mu_i$  is given by  $U_N(\mu_i)$ , where  $N$  is the top layer of the stack.

The downward directed thermal intensity is similarly defined at the top edge of the  $n$ th layer for each  $k$  interval.  $D_n(\mu_i)$ , along the direction  $\mu_i$ , is given by

$$\begin{aligned} D_N(\mu_i) &= 0 \\ D_{N-1}(\mu_i) &= E_N^*(\mu_i) + D_N(\mu_i)e^{-\tau_{N-1}/\mu_i} \\ &\vdots \\ D_n(\mu_i) &= E_{n+1}^*(\mu_i) + D_{n+1}(\mu_i)e^{-\tau_{n+1}/\mu_i} \end{aligned} \quad (A10)$$

where  $N$  is the top layer of the atmosphere,  $\tau_n$  is the column optical thickness of the  $n$ th layer, and  $E_n^*(\mu_i)$  is the downward directed thermal emission by an isolated layer as given by (A4). For the thermal wavelengths considered, the downward intensity at the top of the atmosphere,  $D_N(\mu)$ , is effectively zero. Atmospheric emission incident on the ground is given by  $D_0(\mu_i)$ .

The layer by layer intensities are obtained for the atmosphere using the above algorithms. The upward and downward directed longwave fluxes are obtained via Gaussian quadrature over the respective intensities

$$F_n^\uparrow = \sum_{i=0}^N U_n(\mu_i) \mu_i w_i \quad (A11)$$

and

$$F_n^\downarrow = \sum_{i=0}^N D_n(\mu_i) \mu_i w_i \quad (A12)$$

The net outgoing longwave flux at the top edge of the  $n$ th layer is

$$F_n = F_n^\uparrow - F_n^\downarrow \quad (A13)$$

Finally, the radiative cooling rate profile (flux divergence) is obtained by differencing  $F_n$  and summing the  $F_n$  contributions over the  $k$  distribution.

## APPENDIX B: LINE-BY-LINE RADIATIVE FLUXES

The fluxes and cooling rates tabulated in Tables B1–B4 are line-by-line results for the *McClatchey et al.* [1972] mid-latitude summer atmosphere. A total of 65 layers is used to represent the atmospheric structure with 1-km resolution from 0 to 30 km and 2-km resolution from 30 km to the top of the atmosphere, set at 100 km. Above 25 km, the layer edge temperatures and absorber concentrations are interpolated from the MLS atmospheric profiles. The temperature interpolation was linear in pressure (solid line in Figure B1). While exponential interpolation in pressures might have been preferable (dotted line), the differences are small below 50 km, and the form of temperature interpolation does not impact the line-by-line and correlated  $k$  distribution comparisons.

The molecular data used in the calculations are from the 1982 AFGL compilation [*Rothman*, 1981]. To reduce the computing time, we employed an algorithm which blends nearby lines, depending on the closeness of spacing and the relative strengths of the lines [*Oinas*, 1983]. For spectral integration, the wavelength mesh size was  $0.005 \text{ cm}^{-1}$  for altitudes below 15 km, and  $0.0005 \text{ cm}^{-1}$  for altitudes above 15 km. Tests carried out using higher spectral resolution produced negligible differences. The absorption coefficients were calculated using the average values of pressure and temperature at each layer midpoint. The Voigt profile was employed throughout. The Lorentz wings were truncated at  $5 \text{ cm}^{-1}$  from the line center in all cases. Larger cutoff limits, e.g.,  $10 \text{ cm}^{-1}$ , were tested, but produced virtually no change. Radiative intensities were calculated assuming LTE throughout. Integration over emission angle was performed using a five-point Gaussian quadrature. For the atmospheric structure specified, the numerical precision of the line-by-line fluxes and cooling rates is thought to be of the order  $\sim 0.1\%$ .

The vertical distribution of absorber amount was taken from the *McClatchey et al.* [1972] atmospheric profiles of  $\text{H}_2\text{O}$  and  $\text{O}_3$ , with the absorber amounts interpolated exponentially in pressure to the 65-layer grid, although within each atmospheric layer, the absorber was assumed to be uniformly distributed. For  $\text{CO}_2$ ,  $\text{CH}_4$ , and  $\text{N}_2\text{O}$ , uniform mixing was assumed throughout the atmosphere for relative concentrations of 300, 1.60, and 0.35 ppmv, respectively.

Stimulated emission, which becomes important for the longer wavelengths, was included as a correction to the tabulated line strengths.

$$s_i = s_{i,0} \frac{[1 - \exp(-\beta\nu)]}{[1 - \exp(-\beta_0\nu)]} \quad (B1)$$

where  $s_{i,0}$  is the tabulated line strength at temperature  $T_0 = 296^\circ\text{C}$  and  $\beta = h/kT$ , with  $h$  and  $k$  being the Planck and Boltzmann constants, respectively, and  $\nu$  is the wavelength of the line center.

TABLE B1. H<sub>2</sub>O Line-by-Line Fluxes and Cooling Rates

$Z_n$	0–700 cm <sup>−1</sup>				0–1200 cm <sup>−1</sup>				0–2500 cm <sup>−1</sup>			
	$F_0^\uparrow - F_n^\uparrow$	$F_n^\downarrow$	$CR_n$	$\Delta CR_n$	$F_0^\uparrow - F_n^\uparrow$	$F_n^\downarrow$	$CR_n$	$\Delta CR_n$	$F_0^\uparrow - F_n^\uparrow$	$F_n^\downarrow$	$CR_n$	$\Delta CR_n$
98.0	47.799	0.002	2.702	−0.448	52.923	0.002	2.702	−0.448	85.102	0.002	2.646	−0.461
96.0	47.799	0.002	1.503	−0.067	52.923	0.002	1.503	−0.067	85.102	0.002	1.443	−0.081
94.0	47.799	0.003	1.111	−0.019	52.923	0.003	1.111	−0.019	85.102	0.003	1.051	−0.032
92.0	47.799	0.004	0.916	0.009	52.923	0.004	0.916	0.008	85.102	0.004	0.856	−0.005
90.0	47.799	0.004	0.797	0.028	52.923	0.004	0.797	0.028	85.102	0.004	0.737	0.015
88.0	47.799	0.005	0.715	0.042	52.923	0.005	0.715	0.042	85.101	0.005	0.655	0.030
86.0	47.799	0.005	0.655	0.053	52.923	0.005	0.655	0.053	85.101	0.005	0.595	0.042
84.0	47.799	0.005	0.609	0.062	52.922	0.005	0.609	0.062	85.101	0.005	0.550	0.050
82.0	47.799	0.006	0.573	0.069	52.922	0.006	0.573	0.069	85.101	0.006	0.514	0.058
80.0	47.799	0.006	0.544	0.075	52.922	0.006	0.544	0.075	85.101	0.006	0.486	0.063
78.0	47.798	0.006	0.521	0.078	52.922	0.006	0.521	0.078	85.101	0.007	0.463	0.068
76.0	47.798	0.007	0.502	0.082	52.922	0.007	0.502	0.082	85.100	0.007	0.445	0.071
74.0	47.798	0.007	0.486	0.085	52.922	0.007	0.486	0.085	85.100	0.007	0.430	0.074
72.0	47.798	0.007	0.474	0.085	52.921	0.007	0.474	0.085	85.100	0.008	0.419	0.075
70.0	47.798	0.008	0.466	0.082	52.921	0.008	0.466	0.082	85.100	0.008	0.411	0.073
68.0	47.797	0.013	0.391	−0.042	52.920	0.013	0.391	−0.043	85.097	0.014	0.331	−0.033
66.0	47.795	0.018	0.367	0.014	52.918	0.018	0.367	0.014	85.094	0.020	0.301	0.026
64.0	47.793	0.025	0.403	0.034	52.917	0.025	0.404	0.033	85.090	0.027	0.336	0.053
62.0	47.791	0.031	0.464	0.045	52.915	0.031	0.465	0.044	85.087	0.035	0.406	0.070
60.0	47.789	0.039	0.544	0.051	52.912	0.039	0.545	0.051	85.084	0.044	0.505	0.085
58.0	47.787	0.048	0.641	0.058	52.910	0.048	0.642	0.058	85.078	0.055	0.639	0.098
56.0	47.785	0.058	0.756	0.066	52.908	0.058	0.758	0.065	85.074	0.068	0.813	0.113
54.0	47.783	0.069	0.894	0.074	52.906	0.069	0.897	0.073	85.071	0.082	1.043	0.123
52.0	47.782	0.082	1.065	0.080	52.905	0.082	1.068	0.081	85.068	0.099	1.354	0.126
50.0	47.782	0.095	1.300	0.085	52.905	0.096	1.304	0.086	85.068	0.118	1.811	0.117
48.0	47.787	0.142	1.364	0.010	52.910	0.143	1.369	0.010	85.078	0.180	1.884	0.006
46.0	47.793	0.188	1.363	0.029	52.916	0.189	1.369	0.029	85.090	0.236	1.750	0.051
44.0	47.805	0.255	1.388	0.019	52.928	0.256	1.394	0.020	85.110	0.312	1.699	0.046
42.0	47.821	0.336	1.298	0.013	52.944	0.337	1.303	0.014	85.135	0.400	1.522	0.042
40.0	47.836	0.412	1.214	0.012	52.959	0.413	1.218	0.013	85.158	0.479	1.370	0.041
38.0	47.864	0.562	1.181	0.002	52.987	0.564	1.185	0.002	85.199	0.637	1.306	0.014
36.0	47.892	0.711	1.163	0.003	53.015	0.713	1.166	0.004	85.236	0.790	1.265	0.010
34.0	47.930	0.945	1.165	0.000	53.053	0.948	1.168	0.000	85.286	1.033	1.251	0.001
32.0	47.983	1.284	1.233	−0.002	53.105	1.288	1.235	−0.001	85.352	1.384	1.315	−0.002
30.0	48.035	1.635	1.272	0.004	53.158	1.639	1.273	0.005	85.416	1.746	1.345	0.004
29.0	48.081	1.994	1.175	0.009	53.203	1.998	1.176	0.009	85.471	2.117	1.235	0.009
28.0	48.124	2.301	1.018	0.011	53.247	2.306	1.018	0.012	85.523	2.434	1.070	0.012
27.0	48.164	2.564	0.879	0.011	53.286	2.569	0.880	0.011	85.570	2.704	0.921	0.011
26.0	48.198	2.788	0.751	0.010	53.320	2.794	0.751	0.010	85.609	2.934	0.782	0.010
25.0	48.223	2.978	0.624	0.008	53.345	2.984	0.625	0.007	85.638	3.127	0.645	0.007
24.0	48.246	3.227	0.508	0.004	53.367	3.233	0.508	0.004	85.662	3.381	0.522	0.004
23.0	48.269	3.465	0.408	0.002	53.390	3.472	0.408	0.002	85.688	2.624	0.420	0.002
22.0	48.290	3.677	0.322	0.000	53.411	3.684	0.322	0.000	85.713	3.840	0.329	0.001
21.0	48.301	3.896	0.266	−0.001	53.422	3.904	0.266	−0.001	85.724	4.063	0.270	−0.001
20.0	48.308	4.115	0.224	−0.002	53.429	4.122	0.224	−0.002	85.729	4.285	0.227	−0.002
19.0	48.310	4.339	0.191	−0.003	53.430	4.347	0.191	−0.003	85.730	4.513	0.192	−0.002
18.0	48.303	4.589	0.174	−0.003	53.423	4.596	0.174	−0.003	85.721	4.766	0.174	−0.003
17.0	48.282	4.879	0.165	−0.004	53.402	4.887	0.165	−0.004	85.694	5.062	0.165	−0.004
16.0	48.254	5.230	0.170	−0.004	53.374	5.238	0.170	−0.004	85.661	5.421	0.171	−0.004
15.0	48.216	5.667	0.177	−0.005	53.335	5.676	0.177	−0.005	85.610	5.869	0.177	−0.005
14.0	48.154	6.251	0.191	−0.004	53.273	6.260	0.191	−0.004	85.535	6.468	0.191	−0.005
13.0	48.024	7.126	0.242	−0.006	53.143	7.136	0.242	−0.006	85.375	7.368	0.240	−0.006
12.0	47.591	9.467	0.535	−0.007	52.707	9.479	0.535	−0.007	84.847	9.811	0.538	−0.009
11.0	46.700	15.443	1.260	−0.017	51.810	15.464	1.260	−0.017	83.713	16.163	1.292	−0.019
10.0	45.244	24.923	1.778	−0.017	50.331	24.980	1.781	−0.017	81.740	26.501	1.854	−0.019
9.0	43.030	35.447	1.628	0.014	48.068	35.596	1.636	0.014	78.603	38.499	1.736	0.012
8.0	40.440	46.191	1.431	0.033	45.392	46.521	1.447	0.033	74.727	51.339	1.572	0.031
7.0	36.987	58.421	1.369	0.029	41.793	59.095	1.400	0.028	69.345	66.701	1.556	0.026
6.0	33.214	72.048	1.360	0.018	37.789	73.335	1.413	0.018	63.155	84.511	1.604	0.014
5.0	28.857	86.939	1.324	0.003	33.092	89.230	1.407	0.003	55.706	104.768	1.610	−0.002
4.0	23.709	104.390	1.400	−0.008	27.418	108.435	1.540	−0.008	46.522	129.523	1.772	−0.012
3.0	17.730	124.104	1.411	0.001	20.665	131.107	1.635	0.002	35.397	158.994	1.884	0.003
2.0	11.007	145.363	1.331	0.000	12.892	157.187	1.676	0.001	22.363	193.192	1.937	0.003
1.0	4.840	164.927	1.128	−0.002	5.616	183.604	1.612	−0.001	9.955	227.844	1.873	0.003
0.0	0.000	181.356	0.879	0.007	0.000	208.890	1.492	0.009	0.000	260.844	1.749	0.015

TABLE B2. CO<sub>2</sub> Line-by-Line Fluxes and Cooling Rates

$Z_n$	0–850 cm <sup>-1</sup>				0–1200 cm <sup>-1</sup>				0–2500 cm <sup>-1</sup>			
	$F_0^\uparrow - F_n^\uparrow$	$F_n^\downarrow$	$CR_n$	$\Delta CR_n$	$F_0^\uparrow - F_n^\uparrow$	$F_n^\downarrow$	$CR_n$	$\Delta CR_n$	$F_0^\uparrow - F_n^\uparrow$	$F_n^\downarrow$	$CR_n$	$\Delta CR_n$
98.0	38.355	0.015	26.248	-5.377	38.991	0.015	26.247	-5.379	40.163	0.015	26.271	-5.436
96.0	38.354	0.021	7.918	0.190	38.990	0.021	7.917	0.189	40.162	0.021	7.906	0.142
94.0	38.353	0.025	5.582	0.323	38.989	0.025	5.580	0.322	40.160	0.025	5.564	0.275
92.0	38.351	0.028	4.531	0.256	38.988	0.028	4.529	0.255	40.159	0.029	4.511	0.208
90.0	38.350	0.032	3.915	0.178	38.987	0.032	3.913	0.178	40.158	0.032	3.893	0.130
88.0	38.349	0.035	3.507	0.114	38.985	0.035	3.506	0.112	40.157	0.035	3.484	0.065
86.0	38.348	0.038	3.218	0.059	38.984	0.038	3.216	0.058	40.156	0.038	3.193	0.010
84.0	38.346	0.041	3.003	0.015	38.983	0.041	3.002	0.013	40.154	0.041	2.978	-0.035
82.0	38.345	0.043	2.840	-0.019	38.981	0.043	2.839	-0.021	40.153	0.043	2.814	-0.068
80.0	38.344	0.046	2.715	-0.048	38.980	0.046	2.714	-0.050	40.152	0.046	2.689	-0.099
78.0	38.343	0.049	2.620	-0.071	38.979	0.049	2.619	-0.073	40.150	0.049	2.593	-0.121
76.0	38.341	0.051	2.549	-0.091	38.978	0.051	2.548	-0.093	40.149	0.051	2.522	-0.142
74.0	38.340	0.054	2.501	-0.109	38.976	0.054	2.500	-0.112	40.148	0.054	2.473	-0.161
72.0	38.339	0.056	2.477	-0.130	38.975	0.056	2.476	-0.133	40.146	0.056	2.450	-0.184
70.0	38.338	0.059	2.504	-0.167	38.974	0.059	2.502	-0.168	40.145	0.059	2.476	-0.220
68.0	38.314	0.102	1.814	-0.318	38.950	0.102	1.813	-0.318	40.121	0.102	1.781	-0.327
66.0	38.286	0.144	1.435	-0.014	38.922	0.144	1.434	-0.014	40.093	0.145	1.393	-0.020
64.0	38.256	0.191	1.563	0.124	38.892	0.191	1.563	0.124	40.062	0.192	1.517	0.120
62.0	38.225	0.242	1.929	0.207	38.861	0.242	1.929	0.207	40.030	0.243	1.881	0.205
60.0	38.193	0.300	2.480	0.269	38.829	0.300	2.481	0.271	39.997	0.302	2.437	0.270
58.0	38.162	0.365	3.216	0.316	38.798	0.365	3.219	0.317	39.965	0.368	3.186	0.321
56.0	38.134	0.437	4.161	0.356	38.770	0.437	4.168	0.356	39.935	0.442	4.158	0.365
54.0	38.109	0.518	5.369	0.388	38.745	0.518	5.378	0.391	39.908	0.524	5.413	0.403
52.0	38.092	0.608	6.952	0.402	38.728	0.608	6.967	0.404	39.890	0.617	7.078	0.423
50.0	38.091	0.707	9.327	0.377	38.727	0.708	9.349	0.379	39.888	0.720	9.610	0.404
48.0	38.157	0.981	8.860	0.068	38.793	0.983	8.884	0.070	39.958	1.001	9.140	0.074
46.0	38.226	1.189	7.200	0.161	38.862	1.192	7.220	0.163	40.031	1.213	7.393	0.172
44.0	38.329	1.441	6.277	0.107	38.965	1.444	6.293	0.109	40.137	1.469	6.425	0.114
42.0	38.462	1.707	5.366	0.095	39.098	1.712	5.378	0.096	40.275	1.738	5.471	0.099
40.0	38.581	1.919	4.424	0.147	39.216	1.924	4.432	0.148	40.398	1.951	4.490	0.149
38.0	38.778	2.293	3.770	0.058	39.413	2.299	3.775	0.059	40.599	2.326	3.813	0.059
36.0	38.955	2.597	3.175	0.079	39.590	2.604	3.178	0.080	40.780	2.631	3.201	0.079
34.0	39.168	3.010	2.668	0.035	39.802	3.017	2.669	0.035	40.997	3.043	2.681	0.035
32.0	39.412	3.505	2.329	0.008	40.045	3.513	2.329	0.009	41.242	3.538	2.336	0.009
30.0	39.619	3.913	1.939	-0.004	40.251	3.921	1.938	-0.004	41.451	3.945	1.940	-0.004
29.0	39.777	4.331	1.673	-0.012	40.408	4.340	1.672	-0.012	41.609	4.363	1.672	-0.012
28.0	39.932	4.721	1.585	-0.012	40.563	4.731	1.583	-0.011	41.765	4.753	1.584	-0.012
27.0	40.080	5.068	1.438	-0.015	40.709	5.079	1.436	-0.014	41.913	5.099	1.436	-0.015
26.0	40.214	5.372	1.268	-0.021	40.842	5.382	1.266	-0.020	42.046	5.402	1.265	-0.020
25.0	40.317	5.633	1.058	-0.028	40.943	5.644	1.056	-0.028	42.148	5.663	1.053	-0.027
24.0	40.411	6.043	0.946	-0.020	41.037	6.055	0.944	-0.020	42.241	6.073	0.941	-0.019
23.0	40.525	6.521	0.923	-0.012	41.149	6.534	0.921	-0.012	42.352	6.551	0.920	-0.013
22.0	40.653	6.968	0.792	-0.013	41.274	6.981	0.790	-0.013	42.477	6.997	0.788	-0.013
21.0	40.727	7.454	0.647	-0.013	41.347	7.467	0.645	-0.013	42.548	7.483	0.643	-0.013
20.0	40.790	7.967	0.570	-0.009	41.407	7.981	0.568	-0.009	42.605	7.996	0.566	-0.009
19.0	40.829	8.489	0.473	-0.005	41.442	8.504	0.471	-0.005	42.638	8.519	0.468	-0.004
18.0	40.812	9.003	0.358	-0.002	41.422	9.019	0.356	-0.003	42.615	9.034	0.354	-0.003
17.0	40.689	9.587	0.281	0.001	41.294	9.604	0.279	0.000	42.482	9.620	0.276	0.001
16.0	40.519	10.212	0.240	0.005	41.119	10.230	0.238	0.005	42.301	10.247	0.235	0.005
15.0	40.273	10.861	0.178	0.008	40.867	10.881	0.176	0.008	42.041	10.898	0.173	0.008
14.0	39.878	11.532	0.101	0.008	40.464	11.554	0.099	0.008	41.628	11.572	0.096	0.008
13.0	39.112	12.177	-0.039	-0.004	39.689	12.201	-0.042	-0.003	40.840	12.220	-0.045	-0.004
12.0	37.346	13.734	-0.059	-0.006	37.911	13.760	-0.061	-0.006	39.040	13.785	-0.066	-0.005
11.0	35.210	16.179	0.077	0.003	35.759	16.211	0.074	0.003	36.861	16.247	0.070	0.003
10.0	32.945	19.037	0.131	0.000	33.471	19.078	0.129	-0.001	34.538	19.131	0.124	0.000
9.0	30.237	22.581	0.164	-0.002	30.733	22.639	0.161	-0.002	31.755	22.717	0.157	-0.002
8.0	27.433	26.469	0.190	0.001	27.891	26.552	0.188	0.001	28.858	26.665	0.184	0.001
7.0	24.138	31.111	0.210	0.002	24.547	31.235	0.209	0.001	25.440	31.402	0.206	0.001
6.0	20.844	36.106	0.235	0.001	21.195	36.293	0.235	0.002	22.004	36.528	0.233	0.001
5.0	17.313	41.463	0.230	0.000	17.597	41.742	0.233	0.000	18.302	42.066	0.231	0.000
4.0	13.564	47.287	0.236	0.003	13.774	47.699	0.243	0.003	14.358	48.139	0.242	0.003
3.0	9.644	53.606	0.246	0.001	9.781	54.206	0.258	0.001	10.218	54.797	0.259	0.000
2.0	5.683	60.468	0.266	-0.004	5.750	61.333	0.284	-0.004	6.025	62.119	0.286	-0.003
1.0	2.347	67.159	0.283	-0.001	2.366	68.377	0.308	0.000	2.488	69.380	0.314	0.000
0.0	0.000	73.450	0.299	0.000	0.000	75.121	0.332	0.000	0.000	76.354	0.340	0.001

TABLE B3. O<sub>3</sub> Line-by-Line Fluxes and Cooling Rates

$Z_n$	900–1200 cm <sup>-1</sup>				500–1200 cm <sup>-1</sup>				0–2500 cm <sup>-1</sup>			
	$F_0^\uparrow - F_n^\uparrow$	$F_n^\downarrow$	$CR_n$	$\Delta CR_n$	$F_0^\uparrow - F_n^\uparrow$	$F_n^\downarrow$	$CR_n$	$\Delta CR_n$	$F_0^\uparrow - F_n^\uparrow$	$F_n^\downarrow$	$CR_n$	$\Delta CR_n$
98.0	9.447	0.000	-0.023	-0.001	11.831	0.000	-0.024	-0.003	12.003	0.000	-0.024	-0.003
96.0	9.447	0.000	-0.039	0.002	11.831	0.000	-0.041	-0.001	12.003	0.000	-0.041	-0.002
94.0	9.447	0.000	-0.053	0.003	11.831	0.000	-0.055	-0.003	12.003	0.000	-0.056	-0.002
92.0	9.446	0.000	-0.067	0.004	11.831	0.000	-0.070	-0.003	12.003	0.000	-0.070	-0.003
90.0	9.446	0.000	-0.079	0.006	11.831	0.000	-0.083	-0.002	12.003	0.000	-0.083	-0.002
88.0	9.446	0.000	-0.092	0.008	11.831	0.000	-0.095	-0.003	12.003	0.000	-0.096	-0.003
86.0	9.446	0.000	-0.103	0.008	11.830	0.000	-0.107	-0.003	12.003	0.000	-0.108	-0.003
84.0	9.446	0.000	-0.114	0.009	11.830	0.000	-0.118	-0.004	12.003	0.000	-0.119	-0.004
82.0	9.446	0.000	-0.124	0.009	11.830	0.000	-0.129	-0.004	12.002	0.000	-0.129	-0.005
80.0	9.446	0.000	-0.134	0.011	11.830	0.000	-0.138	-0.006	12.002	0.000	-0.139	-0.006
78.0	9.446	0.000	-0.142	0.010	11.830	0.000	-0.147	-0.007	12.002	0.000	-0.148	-0.007
76.0	9.445	0.000	-0.151	0.012	11.829	0.001	-0.156	-0.006	12.002	0.001	-0.157	-0.007
74.0	9.445	0.001	-0.158	0.012	11.829	0.001	-0.163	-0.007	12.001	0.001	-0.164	-0.008
72.0	9.445	0.001	-0.165	0.013	11.829	0.001	-0.170	-0.008	12.001	0.001	-0.171	-0.008
70.0	9.445	0.001	-0.171	0.014	11.829	0.001	-0.176	-0.008	12.001	0.001	-0.177	-0.008
68.0	9.440	0.003	-0.170	0.033	11.824	0.004	-0.172	0.035	11.996	0.004	-0.173	0.036
66.0	9.436	0.007	-0.139	0.042	11.819	0.007	-0.132	0.044	11.991	0.007	-0.134	0.046
64.0	9.430	0.011	-0.071	0.052	11.813	0.012	-0.052	0.054	11.985	0.012	-0.054	0.057
62.0	9.425	0.017	0.040	0.063	11.808	0.019	0.075	0.065	11.980	0.019	0.073	0.069
60.0	9.420	0.024	0.201	0.073	11.802	0.027	0.256	0.076	11.974	0.027	0.255	0.080
58.0	9.415	0.033	0.421	0.083	11.797	0.037	0.500	0.086	11.969	0.038	0.500	0.091
56.0	9.411	0.045	0.709	0.093	11.793	0.050	0.817	0.096	11.965	0.050	0.818	0.103
54.0	9.409	0.058	1.076	0.102	11.790	0.065	1.218	0.105	11.963	0.065	1.221	0.112
52.0	9.409	0.075	1.536	0.111	11.790	0.083	1.717	0.114	11.962	0.083	1.721	0.124
50.0	9.411	0.094	2.107	0.122	11.793	0.105	2.331	0.126	11.965	0.105	2.339	0.136
48.0	9.429	0.169	2.408	0.043	11.812	0.189	2.679	0.046	11.984	0.189	2.688	0.059
46.0	9.448	0.238	2.321	0.017	11.833	0.269	2.629	0.022	12.005	0.270	2.639	0.036
44.0	9.479	0.331	2.169	0.043	11.864	0.379	2.510	0.051	12.037	0.381	2.521	0.066
42.0	9.518	0.434	1.909	0.086	11.905	0.509	2.272	0.097	12.077	0.511	2.281	0.113
40.0	9.552	0.520	1.601	0.116	11.937	0.623	1.964	0.129	12.109	0.625	1.971	0.146
38.0	9.602	0.663	1.275	0.118	11.979	0.822	1.594	0.134	12.150	0.826	1.597	0.151
36.0	9.634	0.775	0.949	0.086	11.997	0.985	1.194	0.099	12.167	0.990	1.194	0.114
34.0	9.649	0.920	0.684	0.062	11.980	1.202	0.853	0.075	12.147	1.209	0.849	0.089
32.0	9.633	1.086	0.475	0.038	11.904	1.457	0.563	0.050	12.067	1.465	0.556	0.062
30.0	9.579	1.220	0.250	0.023	11.773	1.670	0.259	0.031	11.931	1.680	0.248	0.042
29.0	9.483	1.342	0.077	0.014	11.583	1.868	0.025	0.021	11.736	1.879	0.012	0.030
28.0	9.382	1.440	-0.008	0.009	11.389	2.031	-0.091	0.012	11.536	2.043	-0.105	0.021
27.0	9.276	1.515	-0.090	-0.001	11.195	2.158	-0.193	0.006	11.336	2.172	-0.206	0.012
26.0	9.170	1.568	-0.155	-0.004	11.006	2.255	-0.268	0.000	11.142	2.269	-0.281	0.005
25.0	9.064	1.603	-0.206	-0.006	10.827	2.324	-0.319	-0.004	10.959	2.339	-0.330	0.000
24.0	8.896	1.649	-0.228	-0.008	10.556	2.414	-0.339	-0.007	10.681	2.430	-0.349	-0.004
23.0	8.685	1.703	-0.244	-0.010	10.226	2.517	-0.355	-0.010	10.343	2.534	-0.365	-0.007
22.0	8.431	1.751	-0.285	-0.010	9.841	2.613	-0.398	-0.012	9.950	2.631	-0.408	-0.010
21.0	8.106	1.797	-0.322	-0.010	9.370	2.710	-0.432	-0.013	9.470	2.729	-0.442	-0.011
20.0	7.728	1.843	-0.329	-0.007	8.844	2.803	-0.428	-0.012	8.935	2.823	-0.437	-0.011
19.0	7.295	1.883	-0.331	-0.006	8.264	2.890	-0.416	-0.010	8.345	2.910	-0.423	-0.009
18.0	6.811	1.918	-0.323	-0.003	7.642	2.965	-0.394	-0.007	7.713	2.987	-0.400	-0.007
17.0	6.297	1.951	-0.293	-0.001	7.003	3.034	-0.348	-0.004	7.066	3.056	-0.352	-0.004
16.0	5.770	1.984	-0.260	0.000	6.368	3.099	-0.300	-0.003	6.422	3.122	-0.304	-0.002
15.0	5.204	2.017	-0.236	0.000	5.702	3.161	-0.267	-0.001	5.750	3.185	-0.270	-0.001
14.0	4.561	2.052	-0.223	0.000	4.961	3.224	-0.248	-0.001	5.001	3.250	-0.250	-0.001
13.0	3.897	2.084	-0.205	0.000	4.212	3.281	-0.224	-0.001	4.244	3.310	-0.226	0.000
12.0	3.283	2.133	-0.159	0.001	3.530	3.353	-0.171	0.000	3.556	3.384	-0.172	-0.001
11.0	2.734	2.214	-0.116	0.000	2.927	3.458	-0.123	0.000	2.949	3.490	-0.124	0.000
10.0	2.250	2.320	-0.084	0.000	2.400	3.588	-0.088	0.000	2.418	3.622	-0.089	0.000
9.0	1.825	2.449	-0.058	0.000	1.940	3.740	-0.060	0.000	1.955	3.776	-0.060	-0.001
8.0	1.439	2.604	-0.040	-0.001	1.526	3.920	-0.041	0.000	1.537	3.958	-0.041	0.000
7.0	1.097	2.786	-0.025	0.000	1.160	4.129	-0.025	0.000	1.169	4.169	-0.025	0.000
6.0	0.799	2.995	-0.012	0.000	0.843	4.366	-0.011	0.000	0.849	4.408	-0.011	0.000
5.0	0.552	3.223	-0.002	-0.001	0.581	4.622	-0.001	0.000	0.585	4.666	-0.001	0.000
4.0	0.348	3.476	0.006	0.000	0.366	4.905	0.008	0.000	0.369	4.951	0.008	0.000
3.0	0.191	3.757	0.013	0.000	0.200	5.217	0.015	0.000	0.201	5.266	0.015	0.000
2.0	0.081	4.072	0.019	0.000	0.085	5.564	0.021	0.000	0.085	5.616	0.021	0.001
1.0	0.020	4.410	0.023	0.001	0.021	5.936	0.026	0.000	0.021	5.991	0.026	0.000
0.0	0.000	4.777	0.026	0.000	0.000	6.337	0.029	0.000	0.000	6.396	0.029	0.000



TABLE B4. CH<sub>4</sub> and N<sub>2</sub>O Line-by-Line Fluxes and Cooling Rates

$Z_n$	CH <sub>4</sub>				N <sub>2</sub> O				CH <sub>4</sub> + N <sub>2</sub> O			
	$F_0^\uparrow - F_n^\uparrow$	$F_n^\downarrow$	$CR_n$	$\Delta CR_n$	$F_0^\uparrow - F_n^\uparrow$	$F_n^\downarrow$	$CR_n$	$\Delta CR_n$	$F_0^\uparrow - F_n^\uparrow$	$F_n^\downarrow$	$CR_n$	$\Delta CR_n$
98.0	3.646	0.000	-0.072	0.016	3.721	0.000	-0.039	0.003	6.369	0.000	-0.110	0.019
96.0	3.646	0.000	-0.071	0.015	3.721	0.000	-0.039	0.004	6.369	0.000	-0.109	0.019
94.0	3.645	0.000	-0.070	0.015	3.721	0.000	-0.039	0.004	6.369	0.000	-0.108	0.019
92.0	3.645	0.000	-0.069	0.015	3.721	0.000	-0.038	0.004	6.368	0.000	-0.106	0.019
90.0	3.645	0.000	-0.068	0.015	3.721	0.000	-0.038	0.004	6.368	0.000	-0.105	0.019
88.0	3.645	0.000	-0.068	0.016	3.721	0.000	-0.037	0.004	6.368	0.000	-0.103	0.019
86.0	3.645	0.000	-0.067	0.016	3.721	0.000	-0.037	0.005	6.368	0.000	-0.102	0.019
84.0	3.645	0.000	-0.066	0.016	3.721	0.000	-0.036	0.004	6.368	0.000	-0.100	0.019
82.0	3.645	0.000	-0.065	0.016	3.721	0.000	-0.036	0.005	6.368	0.000	-0.099	0.020
80.0	3.645	0.000	-0.063	0.016	3.721	0.000	-0.035	0.004	6.368	0.000	-0.097	0.020
78.0	3.645	0.000	-0.062	0.016	3.721	0.000	-0.034	0.004	6.368	0.000	-0.096	0.020
76.0	3.645	0.000	-0.061	0.016	3.720	0.000	-0.034	0.005	6.368	0.000	-0.094	0.020
74.0	3.645	0.000	-0.060	0.016	3.720	0.000	-0.033	0.004	6.368	0.000	-0.092	0.020
72.0	3.645	0.000	-0.059	0.016	3.720	0.000	-0.033	0.005	6.368	0.000	-0.090	0.020
70.0	3.645	0.000	-0.058	0.017	3.720	0.000	-0.032	0.005	6.368	0.000	-0.088	0.020
68.0	3.644	0.001	-0.052	0.017	3.720	0.000	-0.029	0.010	6.366	0.001	-0.080	0.025
66.0	3.643	0.001	-0.040	0.017	3.719	0.001	-0.023	0.011	6.365	0.002	-0.061	0.026
64.0	3.642	0.002	-0.024	0.018	3.719	0.001	-0.014	0.010	6.363	0.003	-0.037	0.027
62.0	3.641	0.003	-0.003	0.018	3.718	0.001	-0.003	0.011	6.362	0.004	-0.005	0.027
60.0	3.640	0.003	0.022	0.018	3.718	0.002	0.010	0.011	6.361	0.005	0.032	0.029
58.0	3.640	0.004	0.051	0.019	3.718	0.002	0.026	0.012	6.360	0.007	0.078	0.029
56.0	3.640	0.006	0.086	0.019	3.717	0.003	0.045	0.012	6.360	0.009	0.131	0.031
54.0	3.640	0.007	0.127	0.019	3.717	0.004	0.067	0.012	6.360	0.011	0.194	0.031
52.0	3.640	0.009	0.174	0.020	3.717	0.005	0.092	0.013	6.360	0.013	0.267	0.031
50.0	3.640	0.010	0.228	0.020	3.718	0.006	0.121	0.014	6.361	0.016	0.350	0.033
48.0	3.643	0.017	0.234	0.008	3.719	0.009	0.125	0.008	6.365	0.026	0.360	0.017
46.0	3.645	0.022	0.196	0.007	3.720	0.012	0.106	0.007	6.369	0.034	0.303	0.014
44.0	3.649	0.028	0.160	0.004	3.722	0.015	0.088	0.005	6.374	0.043	0.248	0.011
42.0	3.652	0.033	0.121	0.003	3.723	0.019	0.067	0.006	6.379	0.051	0.188	0.011
40.0	3.655	0.036	0.084	0.007	3.725	0.021	0.049	0.006	6.383	0.057	0.133	0.013
38.0	3.660	0.041	0.057	0.005	3.727	0.024	0.034	0.006	6.390	0.065	0.092	0.011
36.0	3.663	0.043	0.037	0.006	3.728	0.027	0.023	0.006	6.394	0.069	0.061	0.013
34.0	3.666	0.045	0.023	0.006	3.729	0.030	0.016	0.005	6.399	0.074	0.040	0.011
32.0	3.670	0.047	0.017	0.004	3.729	0.033	0.011	0.004	6.403	0.079	0.029	0.010
30.0	3.672	0.048	0.011	0.004	3.728	0.036	0.007	0.003	6.405	0.083	0.020	0.007
29.0	3.673	0.050	0.008	0.003	3.727	0.038	0.004	0.003	6.406	0.087	0.014	0.006
28.0	3.674	0.052	0.008	0.002	3.725	0.041	0.003	0.003	6.406	0.092	0.014	0.004
27.0	3.674	0.054	0.007	0.001	3.723	0.044	0.002	0.002	6.405	0.097	0.011	0.004
26.0	3.674	0.056	0.005	0.001	3.721	0.046	0.000	0.002	6.404	0.101	0.008	0.002
25.0	3.673	0.058	0.003	0.000	3.718	0.049	-0.002	0.002	6.401	0.105	0.003	0.002
24.0	3.671	0.061	0.002	0.000	3.713	0.052	-0.003	0.001	6.395	0.111	0.001	0.002
23.0	3.669	0.065	0.002	-0.001	3.706	0.057	-0.004	0.001	6.388	0.119	0.001	0.001
22.0	3.665	0.069	0.001	-0.001	3.697	0.061	-0.006	0.002	6.378	0.128	-0.002	0.001
21.0	3.659	0.074	-0.001	-0.002	3.685	0.067	-0.008	0.001	6.363	0.138	-0.006	0.001
20.0	3.650	0.081	-0.002	-0.002	3.669	0.073	-0.009	0.001	6.343	0.150	-0.008	0.001
19.0	3.638	0.088	-0.004	-0.002	3.649	0.080	-0.011	0.001	6.316	0.164	-0.011	0.000
18.0	3.620	0.096	-0.006	-0.003	3.622	0.089	-0.013	0.000	6.280	0.179	-0.015	0.000
17.0	3.596	0.106	-0.008	-0.003	3.587	0.099	-0.015	0.000	6.230	0.198	-0.019	0.000
16.0	3.565	0.119	-0.010	-0.003	3.542	0.111	-0.017	0.000	6.166	0.221	-0.022	0.000
15.0	3.521	0.134	-0.013	-0.003	3.483	0.126	-0.020	0.000	6.079	0.249	-0.026	0.000
14.0	3.458	0.152	-0.016	-0.003	3.400	0.144	-0.023	0.000	5.957	0.283	-0.033	0.000
13.0	3.369	0.173	-0.022	-0.003	3.292	0.165	-0.028	0.000	5.789	0.320	-0.042	0.000
12.0	3.246	0.207	-0.025	-0.002	3.150	0.197	-0.031	0.000	5.561	0.381	-0.047	0.000
11.0	3.094	0.268	-0.022	-0.003	2.979	0.250	-0.029	0.000	5.285	0.488	-0.042	0.000
10.0	2.913	0.357	-0.020	-0.003	2.779	0.329	-0.027	0.000	4.959	0.642	-0.038	0.000
9.0	2.697	0.483	-0.018	-0.002	2.545	0.441	-0.024	0.000	4.573	0.860	-0.033	0.001
8.0	2.448	0.651	-0.014	-0.002	2.280	0.594	-0.020	0.000	4.133	1.151	-0.026	0.001
7.0	2.160	0.876	-0.010	-0.001	1.981	0.802	-0.014	0.000	3.631	1.540	-0.018	0.002
6.0	1.840	1.170	-0.004	0.000	1.654	1.079	-0.007	0.000	3.077	2.044	-0.007	0.002
5.0	1.491	1.531	0.002	-0.001	1.306	1.428	0.000	0.000	2.478	2.662	0.002	0.002
4.0	1.120	1.979	0.009	0.000	0.949	1.866	0.009	0.000	1.847	3.423	0.015	0.001
3.0	0.742	2.533	0.018	0.001	0.603	2.416	0.021	0.000	1.214	4.354	0.031	0.001
2.0	0.390	3.220	0.031	0.001	0.299	3.104	0.035	0.000	0.631	5.496	0.051	0.001
1.0	0.125	4.013	0.045	0.000	0.087	3.915	0.050	0.000	0.199	6.801	0.073	0.001
0.0	0.000	4.906	0.058	0.001	0.000	4.846	0.064	0.000	0.000	8.247	0.095	0.000

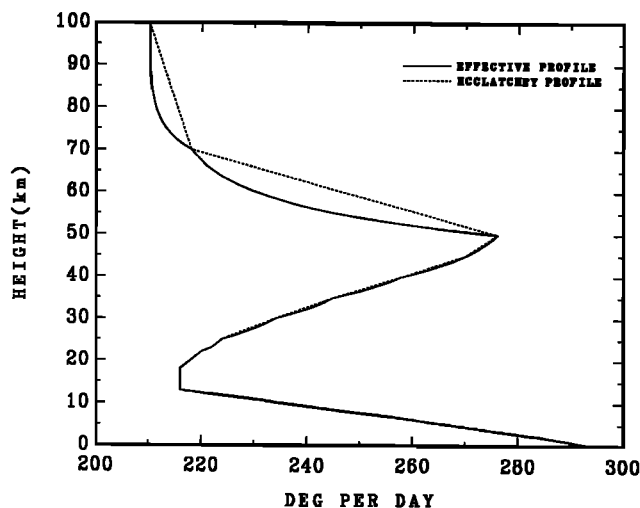


Fig. B1. Mid-latitude summer temperature profile. The solid line shows the McClatchey *et al.* [1972] temperature profile with linear interpolation in pressure as used in the line-by-line calculations. The dotted line shows exponential interpolation.

The net radiative fluxes are obtained as described in Appendix A. The cooling rate is then obtained from the net flux divergence

$$\frac{\Delta T}{\Delta t} = \frac{\Delta F_n}{c_p \Delta m} \quad (\text{B2})$$

where  $\Delta F_n = F_n - F_{n+1}$  is the net flux deposited within the  $n$ th layer,  $c_p$  is the heat capacity of air, and  $\Delta m$  is the mass of air per unit area in the  $n$ th layer. Expressing the mass in terms of the layer pressure differential in millibars, the cooling rate is given by

$$\frac{\Delta T}{\Delta t} = \frac{8.422 \Delta F_n}{\Delta P} \quad (\text{B3})$$

This relates the radiative fluxes ( $\text{W m}^{-2}$ ) to the atmospheric cooling rates ( $^{\circ}\text{C/d}$ ) in Tables B1–B4.

Tables B1–B4 list the line-by-line radiative fluxes for selected spectral regions for water vapor,  $\text{CO}_2$ ,  $\text{O}_3$ ,  $\text{CH}_4$ , and  $\text{N}_2\text{O}$ . The results for the upward fluxes are given as the flux depletion, or the difference between the flux emitted by the ground surface and the outgoing flux at the top of the atmosphere. (The flux emitted by the ground is the Planck radiation within the specified wavelength intervals for a mid-latitude summer surface temperature of 294 K.) This gives a measure of the greenhouse trapping by each gas and makes comparisons of the upwelling flux less sensitive to the precise wavelength interval used in the computations.

The results for  $\text{H}_2\text{O}$ ,  $\text{CO}_2$ , and  $\text{O}_3$  are given for the individual gases in Tables B1–B3. Contributions from the water vapor continuum are excluded. The results for the principal gases within the specified broad spectral regions are presented in cumulative form to permit comparison of the radiative cooling contributed by individual spectral regions relative to the spectrally integrated cooling. In Table B4 the line-by-line results for  $\text{CH}_4$  and  $\text{N}_2\text{O}$  are given first individually for each gas, then in (line-by-line) overlapping form over the same spectral interval from 1100 to  $1350 \text{ cm}^{-1}$ .

The upward and downward fluxes calculated with the

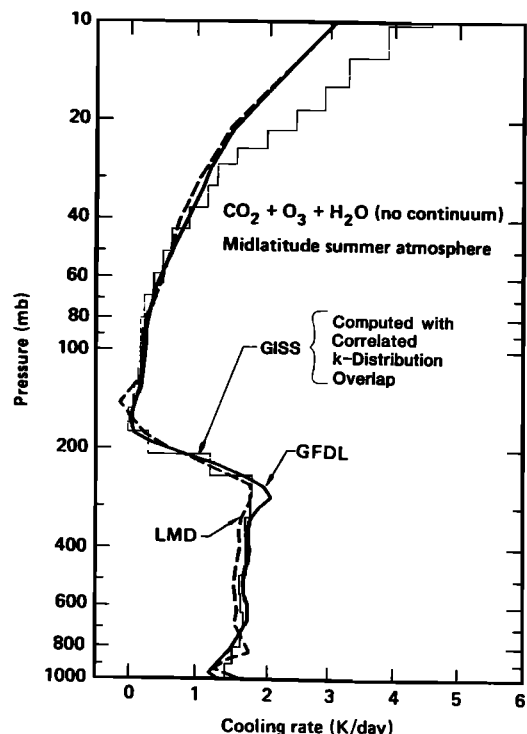


Fig. B2. Mid-latitude summer line-by-line cooling. The cooling rates shown are for  $\text{CO}_2$ ,  $\text{O}_3$ , and  $\text{H}_2\text{O}$  (without water vapor continuum) reported in the ICRCCM intercomparisons [Luther and Fouquart, 1984]. The solid line gives the GFDL line-by-line results, and the dashed line those of LMD. The light histogram curve represents the GISS-correlated  $k$  distribution results with the band model parameters least squares fitted individually to  $\text{CO}_2$ ,  $\text{O}_3$ , and  $\text{H}_2\text{O}$  line-by-line results, then combined analytically to compute the overlapping absorption.

correlated  $k$  distribution differ little from the line-by-line fluxes given in Tables B1–B4. For ozone, the flux differences between the correlated  $k$  distribution and line-by-line results at the top and bottom of the atmosphere are less than  $0.1 \text{ W m}^{-2}$ , and for  $\text{CO}_2$ , less than  $0.2 \text{ W m}^{-2}$ . For water vapor, the flux differences are 0.4 and  $1 \text{ W m}^{-2}$  ( $\sim 0.5\%$  error) for the outgoing and surface fluxes, respectively. Close agreement is expected, since the band model parameters were least squares fitted to the line-by-line calculations.

The line-by-line results for  $\text{CO}_2$  and ozone presented here differ slightly from the GISS results included in the ICRCCM comparisons [Luther and Fouquart, 1984]. The earlier results used 33 layers instead of the present 65 layers to model the vertical structure of the atmosphere. Also, the  $4.3\text{-}\mu\text{m}$  band was not included in the earlier results. In comparing the results for  $\text{CO}_2$ , both the upward and downward fluxes differ by  $0.25 \text{ W m}^{-2}$ . The sense of the difference is such that the higher vertical resolution resulted in a less opaque atmosphere, i.e., the downward flux is smaller and the outgoing flux is larger with the 65-layer resolution. The present results agree with the LMD (Laboratoire de Meteorologie Dynamique, Paris) fluxes for  $\text{CO}_2$  to within  $0.11 \text{ W m}^{-2}$  at the top of the atmosphere and to within  $0.03 \text{ W m}^{-2}$  at the ground surface, but the differences with respect to the GFDL results are now larger ( $\sim 0.2 \text{ W m}^{-2}$ ).

For ozone, the response of the upward and downward fluxes to the higher vertical resolution is similar to the  $\text{CO}_2$  results, with the flux difference being  $0.03 \text{ W m}^{-2}$ . Inclusion

of the ozone rotational band ( $0\text{--}160\text{ cm}^{-1}$ ) and the  $2100\text{ cm}^{-1}$  band decreases the outgoing flux by  $1.2\text{ W m}^{-2}$  but contributes little ( $0.04\text{ W m}^{-2}$ ) to the downwelling flux at the ground.

For water vapor, the line-by-line fluxes in Table B1 are found to differ substantially from ICRCCM results. In the ICRCCM comparisons, *Luther and Fouquart* [1984] show a spread of  $4\text{ W m}^{-2}$  for the downward flux at the ground surface and a similar spread for the outgoing flux at the top of the atmosphere. The ICRCCM surface fluxes range from  $267.29\text{ W m}^{-2}$  (GFDL, LMD) to  $263.25\text{ W m}^{-2}$  (Goddard Laboratory for Atmospheric Studies (GLAS) Greenbelt, Maryland), while the outgoing flux depletion spans the range of  $86.76\text{ W m}^{-2}$  (GLAS),  $87.46\text{ W m}^{-2}$  (GFDL), to  $91.47\text{ W m}^{-2}$  (LMD). Our present results for water vapor are  $260.84\text{ W m}^{-2}$  for the surface flux and  $85.1\text{ W m}^{-2}$  for the outgoing flux depletion. The specific reason for these differences is not clear, but it seems reasonable to believe that the model treatment of the vertical absorber distribution may be the likely cause. This is supported by the ICRCCM comparisons, which show flux differences of only  $\sim 0.1\text{ W m}^{-2}$  for  $\text{CO}_2$  (uniform atmospheric distribution), somewhat larger differences for ozone, and the largest differences for water vapor.

Figure B2 shows the atmospheric cooling rate in the more realistic case of overlapping absorption by  $\text{H}_2\text{O}$ ,  $\text{CO}_2$ , and  $\text{O}_3$  (but with the water vapor continuum omitted). Comparison is made to the ICRCCM results [*Luther and Fouquart*, 1984] where the GFDL line-by-line cooling rate is shown by the solid line and the LMD results are given by the dashed line. The light histogram curve is the GISS-correlated  $k$  distribution result which was obtained using least squares fitted band model parameters for  $\text{H}_2\text{O}$ ,  $\text{CO}_2$ , and  $\text{O}_3$  (for the line-by-line results in Tables B1–B3). Overlapping absorption effects were computed according to (32) and (33) using  $10\text{ cm}^{-1}$  spectral resolution for the band model parameters.

The cooling rate in Figure B2, computed with the correlated  $k$  distribution overlap procedure, is seen to agree closely with the line-by-line results from the ground through the 40-mbar pressure level. This tends to confirm the general applicability of the Malkmus model formulation for modeling nongray gaseous absorption within the Lorentz line regime. Band model parameters, though least squares fitted to line-by-line results, seem to retain their basic physical meaning; hence overlapping absorption by several gases can be evaluated with good accuracy using the formulation described in section 4.

In the case of single gases, and for overlapping absorption by two gases undergoing uniform variations in absorber amount such as  $\text{CH}_4$  and  $\text{N}_2\text{O}$ , the rather poor representation of  $k$  distributions by the Malkmus model in the Doppler regime is mitigated by good layer-to-layer vertical correlation of the actual  $k$  distributions of these gases. Also, the fact that the band model parameters are forced to fit the homogeneous path transmission permits reasonable accuracy to be obtained in these cases for radiative cooling even in the Doppler regime.

However, computations of overlapping absorption for  $\text{CO}_2$  and  $\text{H}_2\text{O}$  using the correlated  $k$  distribution approach produce excessive cooling above  $\sim 30$  mbar. This problem, unfortunately, is fundamental in nature. It arises from the poor vertical correlation of the combined  $k$  distributions of  $\text{CO}_2$  and  $\text{H}_2\text{O}$ , aggravated by the rapid change with height of the relative absorber strengths and amounts. Though the

poor representation of Doppler regime  $k$  distributions by the Malkmus model formulation is a contributing factor, which makes the band model parameters increasingly more “numerical” in nature and thus less able to retain their physical meaning, it is not the underlying cause of the problem. We have examined the cooling rate calculations for overlapping absorption using numerical  $k$  distributions, thus completely eliminating the Malkmus model as a source of error. However, the problem persists because the overlapping  $k$  distributions of  $\text{CO}_2$  and  $\text{H}_2\text{O}$  are not sufficiently correlated between neighboring layers.

A simple expedient to deal with this problem in typical atmospheric modeling applications is to use empirical scaling of the absorber amounts for water vapor and  $\text{CO}_2$  within the 5- to 30-mbar region (since we have accurate results from line-by-line calculations for comparison). This approach has the advantage of retaining a linear dependence on the number of model layers, and it does not require a large increase in the number of  $k$  distribution intervals to improve the accuracy.

To more directly address the problem of the vertical correlation of overlapping  $k$  distributions, *West et al.* [1990] describe a spectral mapping procedure that forces correlation of the atmospheric  $k(g)$  values in frequency with respect to  $k(g)$  values of a selected reference layer. In this approach, the standard frequency to  $k$  distribution transformation for the reference layer is used to rearrange absorption coefficients of the other layers in exactly the same way, thus guaranteeing frequency correlation throughout the atmosphere. However, the resulting  $k(g)$  will in general no longer be a monotonic function of  $g$ ; it may even be multivalued and require of the order of 100  $g$  intervals to achieve 1% accuracies for the cooling rates. While the spectral mapping technique effectively addresses the vertical correlation of absorption coefficients for a given profile of absorber amounts, the frequency transformations need to be recomputed whenever the absorber distributions depart noticeably from their reference profiles.

This somewhat pathological behavior of overlapping absorption by  $\text{CO}_2$  and stratospheric water vapor underscores the difficulties encountered in developing parameterizations for computing radiative cooling rates that are both fast and accurate and applicable in all regions of the atmosphere. Fortunately, line-by-line calculations can provide the necessary standard of comparison against which faster parameterizations may be tested and improved.

From the tabulated fluxes in Tables B1–B4, it is clear that the Doppler regime correlation problems that affect the stratospheric cooling rates in the case of overlapping absorption by  $\text{CO}_2$  and water vapor have little impact on the radiative fluxes. The downward fluxes at the ground surface obtained by GFDL and LMD for the line-by-line overlap of  $\text{H}_2\text{O}$ ,  $\text{CO}_2$ , and  $\text{O}_3$  are  $302.46$  and  $300.69\text{ W m}^{-2}$ , with outgoing flux depletions of  $127.69$  and  $128.84\text{ W m}^{-2}$ , respectively. For comparison, the GISS-correlated  $k$  distribution results with the analytic overlap formulation are  $305.94$  and  $129.46\text{ W m}^{-2}$ , respectively.

**Acknowledgments.** The work reported here spans nearly 15 years of development, testing, and application. During this time, many helpful contributions and suggestions have come from a large number of individuals. We are especially grateful to J. Hansen, R. Goody, S. Lebedeff, L. Travis, and W.-C. Wang for their contribu-

tions, comments, and suggestions that have inspired and molded our understanding of the correlated  $k$  distribution. We also thank T. Mo, A. Oppenheim, J. Owen, R. Anne, J. Forkosh, and P. Lee for running numerous test cases and examples. We also thank B. Carlson, S. Fels, W. Rossow, and two anonymous reviewers for their critical reading of the manuscript and constructive suggestions. Finally, we want to thank R. Schiffer of NASA Headquarters for his continued support of climate studies at GISS.

## REFERENCES

- Altshuler, T. L., and J. I. F. King, Inference of band structures from laboratory data, Specialist Conference on Molecular Radiation and its Application to Diagnostic Techniques, NASA TMX 53711, pp. 96–112, Natl. Aeronaut. and Space Admin., Washington, D. C., 1968.
- Ambartsumian, V., The effect of the absorption lines on the radiative equilibrium of the outer layers of the stars, *Publ. Obs. Astron. Univ. Leningrad*, 6, 7–18, 1936.
- Arking, A. A., and K. Grossman, The influence of line shape and band structure on temperatures in planetary atmospheres, *J. Atmos. Sci.*, 29, 937–949, 1972.
- Armstrong, B. H., Analysis of the Curtis-Godson approximation and radiation transmission through inhomogeneous atmospheres, *J. Atmos. Sci.*, 25, 312–322, 1968.
- Cess, R. D., D. P. Kratz, S. J. Kim, and J. Caldwell, Infrared radiation models for atmospheric methane, *J. Geophys. Res.*, 91, 9857–9864, 1986.
- Chou, M. D., and A. Arking, Computation of infrared cooling rates in the water vapor bands, *J. Atmos. Sci.*, 37, 855–867, 1980.
- Clough, S. A., F. X. Kneizys, and R. W. Davies, Line shape and the water vapor continuum, *Atmos. Res.*, 23, 229–241, 1989.
- Cox, S. K., and K. T. Griffith, Estimates of radiative divergence during phase III of the GARP Atlantic Tropical Experiment, I, Methodology, *J. Atmos. Sci.*, 36, 576–585, 1979.
- Curtis, A. R., Discussion of "A statistical model for water vapour absorption," *Q. J. R. Meteorol. Soc.*, 78, 638–640, 1952.
- Domoto, G. A., Frequency integration for radiative transfer problems involving homogeneous non-grey cases: The inverse transmission function, *J. Quant. Spectrosc. Radiat. Transfer*, 14, 935–942, 1974.
- Drayson, S. R., Rapid computation of the Voigt profile, *J. Quant. Spectrosc. Radiat. Transfer*, 16, 611–614, 1975.
- Elsasser, W. M., Heat Transfer by Infrared Radiation in the Atmosphere, *Harvard Meteorol. Stud.*, 6, 107 pp., Harvard University Press, Cambridge, Mass., 1942.
- Fels, S. B., and M. D. Schwartzkopf, The simplified exchange approximations: A new method for radiative transfer calculations, *J. Atmos. Sci.*, 32, 1475–1488, 1975.
- Fels, S. B., and M. D. Schwartzkopf, An efficient, accurate algorithm for calculating CO<sub>2</sub> 15- $\mu$ m band cooling rates, *J. Geophys. Res.*, 86, 1205–1232, 1981.
- Godson, W. L., The evaluation of infrared-radiative fluxes due to atmospheric water vapour, *Q. J. R. Meteorol. Soc.*, 79, 367–379, 1953.
- Goldman, A., and T. G. Kyle, A comparison between statistical model and line by line calculations with application to the 9.6  $\mu$ m ozone and the 2.7  $\mu$ m water vapor bands, *Appl. Opt.*, 7, 1167–1177, 1968.
- Goody, R. M., A statistical model for water vapor absorption, *Q. J. R. Meteorol. Soc.*, 78, 165–169, 1952.
- Goody, R. M., *Atmospheric Radiation*, 436 pp., Oxford University Press, New York, 1964.
- Goody, R., R. West, L. Chen, and D. Crisp, The correlated- $k$  method for radiation calculations in nonhomogeneous atmospheres, *J. Quant. Spectrosc. Radiat. Transfer*, 42, 539–550, 1989.
- Hansen, J. E., and L. D. Travis, Light scattering in planetary atmospheres, *Space Sci. Rev.*, 16, 527–610, 1974.
- Hansen, J. E., W. C. Wang, and A. A. Lacis, Mount Agung eruption provides test of a global climate perturbation, *Science*, 199, 1065–1068, 1978.
- Hansen, J., D. Johnson, A. Lacis, S. Lebedeff, P. Lee, D. Rind, and G. Russell, Climate impact of increasing atmospheric carbon dioxide, *Science*, 213, 957–966, 1981.
- Hansen, J., G. Russell, D. Rind, P. Stone, A. Lacis, S. Lebedeff, R. Ruedy, and L. Travis, Efficient three-dimensional global models for climate studies: Models I and II, *Mon. Weather Rev.*, 111, 609–662, 1983.
- Hansen, J., A. Lacis, D. Rind, G. Russell, P. Stone, I. Fung, R. Ruedy, and J. Lerner, Climate sensitivity: Analysis of feedback mechanisms, in *Climate Processes and Climate Sensitivity*, edited by J. E. Hansen and T. Takahashi, pp. 130–163, AGU, Washington, D. C., 1984.
- Hansen, J., I. Fung, A. Lacis, D. Rind, S. Lebedeff, R. Ruedy, and G. Russell, Global climate changes as forecast by Goddard Institute for Space Studies three-dimensional model, *J. Geophys. Res.*, 93, 9341–9364, 1988.
- Howard, J. N., D. E. Burch, and D. Williams, Infrared transmission of synthetic atmospheres, Parts I–V, *J. Opt. Soc. Am.*, 46, 186–190, 237–241, 242–245, 334–338, 452–455, 1956.
- Kiehl, J. T., and V. Ramanathan, CO<sub>2</sub> radiative parameterization used in climate models: Comparison with narrow band models and with laboratory data, *J. Geophys. Res.*, 88, 5191–5202, 1983.
- Kondratyev, K. Ya., *Radiation in the Atmosphere*, 912 pp., Academic, San Diego, Calif., 1969.
- Kratz, D. P., and R. D. Cess, Infrared radiation models for atmospheric ozone, *J. Geophys. Res.*, 93, 7047–7054, 1988.
- Kuhn, W. R., and J. London, Infrared radiative cooling in the middle atmosphere (30–110 km), *J. Atmos. Sci.*, 26, 189–204, 1969.
- Lacis, A. A., and J. E. Hansen, A parameterization for the absorption of solar radiation in the Earth's atmosphere, *J. Atmos. Sci.*, 31, 118–133, 1974.
- Lacis, A., W. C. Wang, and J. Hansen, Correlated  $k$ -distribution method for radiative transfer in climate models: Application to effect of cirrus clouds on climate, *NASA Conf. Publ.*, 2076, 309–314, 1979.
- Lacis, A., J. Hansen, P. Lee, T. Mitchell, and S. Lebedeff, Greenhouse effect of trace gases, 1970–1980, *Geophys. Res. Lett.*, 8, 1035–1038, 1981.
- Lebedinsky, A. I., Radiative equilibrium in the Earth's atmosphere, *Proc. Leningrad Univ. Ser. Math.*, 3, no. 31, 152–175, 1939.
- Lindquist, G. H., and F. S. Simmons, A band model formulation for very nonuniform paths, *J. Quant. Spectrosc. Radiat. Transfer*, 12, 807–820, 1972.
- Liou, K. N., *An Introduction to Atmospheric Radiation*, Int. Geophys. Ser., vol. 26, Academic, San Diego, Calif., 1980.
- Luther, F. M., and Y. Fouquart, The intercomparison of radiation codes in climate models (ICRCCM), *WMO Rep. WCP-93*, 37 pp., World Meteorol. Organ., Geneva, Switzerland, 1984.
- Malkmus, W., Random Lorentz band model with exponential-tailed  $s^{-1}$  line-intensity distribution function, *J. Opt. Soc. Am.*, 57, 323–329, 1967.
- Manabe, S., and F. Moller, On the radiative-equilibrium and heat balance of the atmosphere, *Mon. Weather Rev.*, 89, 503–532, 1961.
- McClatchey, R. A., R. W. Fenn, J. E. A. Selby, F. E. Volz, and J. S. Garing, Optical properties of the atmosphere, *Environ. Res. Pap. 411*, 108 pp., Air Force Cambridge Res. Lab., Bedford, Mass., 1972.
- McClatchey, R. A., W. S. Benedict, S. A. Clough, D. E. Burch, R. F. Calfee, K. Fox, L. S. Rothman, and J. S. Garing, AFCRL atmospheric absorption line parameters compilation, *Environ. Res. Pap. 434*, 78 pp., Air Force Cambridge Res. Lab., Bedford, Mass., 1973.
- Oinas, V., Rapid transmittance integration using line blending and a straight-line fit to line shapes, *J. Quant. Spectrosc. Radiat. Transfer*, 29, 407–411, 1983.
- Pierluissi, J. H., P. C. Vanderwood, and R. B. Gomez, Fast calculational algorithm for the Voigt profile, *J. Quant. Spectrosc. Radiat. Transfer*, 18, 555–558, 1977.
- Rind, D., R. Suozzo, N. K. Balachandran, A. Lacis, and G. Russell, The GISS global climate-middle atmosphere model, I, Model structure and climatology, *J. Atmos. Sci.*, 45, 329–370, 1988.
- Rodgers, C. D., and C. D. Walshaw, The computation of infra-red cooling rate in planetary atmospheres, *Q. J. R. Meteorol. Soc.*, 92, 67–92, 1966.
- Rothman, L. S., AFGL atmospheric absorption line parameters compilation: 1980 version, *Appl. Opt.*, 20, 791–795, 1981.
- Smith, W. L., W. C. Shen, and H. B. Howell, A radiative heating model derived from the GATE MSR experiment, *J. Atmos. Meteorol.*, 16, 384–392, 1977.
- Stephens, G. L., The parameterization of radiation for numerical

- weather prediction and climate models, *Mon. Weather Rev.*, **112**, 826–867, 1984.
- van de Hulst, H. C., Theory of absorption lines in the atmosphere of the Earth, *Ann. Astrophys.*, **8**, 1–11, 1945.
- Walshaw, C. D., and C. D. Rodgers, The effect of the Curtis-Godson approximation on the accuracy of radiative heating-rate calculations, *Q. J. R. Meteorol. Soc.*, **89**, 122–130, 1963.
- Wang, W. C., A parameterization for the absorption of solar radiation by water vapor in the Earth's atmosphere, *J. Appl. Meteorol.*, **15**, 21–27, 1976.
- Wang, W. C., and G. Y. Shi, Total band absorptance and  $k$ -distribution function for atmospheric gases, *J. Quant. Spectrosc. Radiat. Transfer*, **39**, 387–397, 1988.
- Wang, W. C., Y. L. Yung, A. A. Lacis, T. Mo, and J. E. Hansen, Greenhouse effects due to man-made perturbations of trace gases, *Science*, **194**, 685–690, 1976.
- West, R., D. Crisp, and L. Chen, Mapping transformations for broadband atmospheric radiation calculations, *J. Quant. Spectrosc. Radiat. Transfer*, **43**, 191–199, 1990.
- Wiscombe, W., and J. Evans, Exponential-sum fitting of radiative transmission functions, *J. Comput. Phys.*, **24**, 416–444, 1977.
- Yamamoto, G., Direct absorption of solar radiation by atmospheric water vapor, carbon dioxide and molecular oxygen, *J. Atmos. Sci.*, **19**, 182–188, 1962.
- Yamamoto, G., M. Tanaka, and S. Asano, Radiative transfer in water clouds in the infrared region, *J. Atmos. Sci.*, **27**, 282–292, 1970.
- Yamamoto, G., M. Aida, and S. Yamamoto, Improved Curtis-Godson approximation in a non-homogeneous atmosphere, *J. Atmos. Sci.*, **29**, 1150–1155, 1972.
- Young, S. J., Band model formulation for inhomogeneous optical paths, *J. Quant. Spectrosc. Radiat. Transfer*, **15**, 483–501, 1975.
- 
- A. A. Lacis, NASA Goddard Space Flight Center, Institute for Space Studies, 2880 Broadway, New York, NY 10025.
- V. Oinas, STX, Incorporated, 2880 Broadway, New York, NY 10025.

(Received May 2, 1990;  
revised August 29, 1990;  
accepted August 29, 1990.)